Highly Ordered Organic Layers and Wires

Inaugural-Dissertation
zur
Erlangung des Doktorgrades
der Mathematisch-Naturwissenschaftlichen Fakultät
der Universität zu Köln

vorgelegt von
M.Sc. Yannic Frank Falke
aus
Dormagen

Köln, 2022

Berichterstatter (Gutachter):

Prof. Dr. Alexander Grüneis

Prof. Dr. Klas Lindfors

Vorsitzender:
Prof. Dr. Mathias Wickleder

Beisitzer:
Dr. Dirk Hertel

Tag der mündlichen Prüfung: 09.08.2022

Contents

Abstract

This thesis deals with the synthesis of highly ordered organic thin films and the characterization of the molecule-substrate interaction through spectroscopy and diffraction. Organic devices, such as organic light emitting diodes (OLEDs) and organic field effect transistors (OFETs) have become ubiquitous in modern times. The transistor and high frequency performance of such organic devices crucially depends on charge carrier mobility. In inorganic semiconductors, which are bonded covalently, the band masses are typically lower and their crystallinity higher in comparison to their organic counterparts. In a simple Drude model, the charge carrier mobility is inversely proportional to the effective charge carrier mass. The low effective mass and high crystallinity of inorganic semiconductors result in large carrier mobilities of up to $1 \times 10^7\,\mathrm{cm}^2/\mathrm{Vs}$ [1] for GaAs at low temperatures. The large effective mass in van der Waals bonded organic materials and their poorer molecular order decrease the carrier mobility. This thesis addresses the limitations of the inherently low mobility and disorder in organic thin films in a twofold way.

The first is the introduction of a novel synthesis method for graphene nanoribbons, which are covalently bonded long stripes of graphene. This new method, developed in this thesis, is based on laser induced photothermal heating. It allows for the synthesis of atomically precise graphene nanoribbons with a higher degree of control over the reaction

than conventional methods and is shown to work in a multitude of different nanoribbon species. The growth takes place in an area that is solely governed by the spotsize of the incoming laser light ($\sim 4\,\mu$m). This method has an advantage over present methods through the exact control of the growth kinetics with regards to chemical uniformity and local area distribution. Additionally, the physical properties and growth kinetics of photothermally grown graphene nanoribbons are investigated by means of Raman spectroscopy.

In a second way, the growth of organic moiré structures on a topological insulator is studied. We show the growth of C_{60} thin films on the topological insulator Bi_4Te_3 through electron diffraction and observe a moiré pattern. This indicates very long range order in the form of a (4×4) on (9×9) superstructure that is observable on the entire $1 \times 1\,\mathrm{cm}^2$ sample surface. The growth of the structure is performed using molecular beam epitaxy (MBE) and chemical vapor deposition (CVD) in ultra-high vacuum (UHV) conditions and the properties of the interface are studied using low energy electron diffraction (LEED), angle resolved photoemission spectroscopy (ARPES) and density functional theory (DFT). We find that a C_{60} induced surface reconstruction and the softness of the underlying, layered topological insulator are responsible for the high order. The theoretical calculations find that the structure bonds mostly through physisorption and both the theory and band structure measurements show no perturbation of the electronic states of the topological insulator by the overlayer.

Finally, we extend the concept of well ordered growth of organic thin films on topological insulators to superconducting alkali metal doped C_{60}. These organic films are metallic at room temperature but turn

into *s*-wave superconductors at a critical temperature of 28 K. The combination of this relatively high transition temperature in combination with the well defined growth opens up a new playground for both experimental and theoretical studies. The van der Waals bond nature of the interface protects the interface from alloying, which can be a problem for inorganic topological insulator–superconductor interfaces. We show a novel synthesis route for the growth of well ordered superconducting alkali metal doped fullerenes on the topological insulator Bi_4Te_3. The growth process is studied using LEED and ultra violet photoemission spectroscopy (UPS) and makes the phase pure synthesis of thin film Rb_3C_{60} possible, which is crucial to avoid contamination through an insulating Rb_6C_{60} phase. ARPES spectra confirm the intactness of the interface by measurements of both the Fermi surface of the topological insulator as well as the newly formed Rb_3C_{60} metallic film.

Chapter 1
Introduction

Field-Effect Transistors (FETs) are at the very heart of modern electronic devices. With increasing demand of high performance electronics, the number of transistors in a given device needs to gradually increase while the overall package size should remain constant. This trend, which is described by the empirical Moore's law, drove the industry to develop ever smaller semiconductor processing techniques with modern devices reaching a count of up to 5×10^{10} FETs per chip.[2, 3]
At the time of writing, TSMC, the worlds largest semiconductor manufacturer, uses a 5 nm processing variant to create the FETs on its chips.[4] Putting that into perspective with a Si–Si bond length of 2.4 Å in a silicon single crystal yields a staggering $\sim 20 \times 20$ atoms per FET. This means that there is only finite room left for optimization of silicon chips, since the electronic properties of the bulk start to break down on these atomic scales due to increased scattering at the edges and possible tunneling.
Increasing research on alternative semiconductors is the logical consequence where Organic Field-Effect Transistors (OFETs) or Organic Thin-Film Transisitors (OTFTs) show promising results.[5–8] Here, silicon is replaced by highly conjugated (aromatic) organic molecular thin films with semiconducting properties such as α–sexithiophene. These films promise a multitude of advantages over their inorganic counterparts such as inherent flexibility, low production cost and solution based processing.
The quality and usability of a TFT is determined by factors such as the

I_{ON}/I_{OFF} current ratio, subthreshold slope and carrier mobility.[9–12] These merits not only depend on the chemical structure of the molecule but also on the degree of order that a thin film exhibits. A highly crystalline film is less prone to defect scattering and is therefore most likely to yield high performance TFTs.[13, 14] This is why recent work has focused on studying thin film growth, molecule-molecule interaction as well as molecule-substrate interaction. C_{60} already inherently possesses high symmetry and can be condensed into van der Waals crystals which is what makes it an excellent candidate to study and optimize the growth of thin films for future use in TFTs.

In recent years, the field of bottom-up grown graphene nanoribbons (GNRs) has blossomed. With this approach, all GNR properties are defined by the precursor molecule. These precursors can readily be synthesized through organic chemistry and processed into GNRs by means of chemical vapour deposition (CVD) or sublimation and polymerization in ultra high vacuum (UHV). The shape and termination of the GNR are solely given by the design of the precursor, which is in stark contrast to lithographic methods that offer little control over the edge termination and are limited by the resolution of the optical lithography process.[15, 16] GNRs are defined by their size and shape in one direction e.g. 7-armchair graphene nanoribbons (7-AGNRs) are seven atoms wide and exhibit so called armchair geometry. Regarding the electronic properties, the electronic states of the short axis are quantized whereas the states along the long axis are continuous, i.e. they form electronic energy bands. Since their electronic properties are well defined by their appearance, they have become a sandbox for theorists and experimental physicists alike. Tunability of the band gap and general band structure

paired with an intrinsically high order marks them as perfect candidates for high performance, next generation TFTs and working devices have already been constructed.[17–19]

The bottom-up approach overcomes these issues by generating the GNRs from well defined organic molecules whose chemical properties determine the direction of growth and the resulting shape of the ribbon. By clever design and optimization of the growth conditions, the bottom-up approach can yield a plethora of different GNRs with all of them having perfect edge termination.[20] This in turn results in very clean and well defined GNRs with reproducible properties.

Chapter 2
Theory and Methods

2.1 Two-Dimensional Crystallography

2.1.1 Low Energy Electron Diffraction

Understanding the crystal structure of a material is a critical step prior to studying other properties, since the symmetry and orientation of crystals can be taken advantage of to simplify experiments. Additionally, the cleanliness of the surface, termination and orientation of a crystal surface is an important aspect for growth of ordered thin films. While X-ray diffraction (XRD) is the most commonly used method for investigation of the structure of a three-dimensional crystal[23–25], in surface science low energy electron diffraction (LEED) is the optimal experimental method to study these properties on a large scale.[26, 27] This is mainly due to the usage of low energy electrons ($\sim 10 - 200\,\mathrm{eV}$) as an excitation source, which have wavelength in the range of Å and small mean free path on the order of Å in solids.[21] This results in extreme surface sensitivity which allows to very accurately determine, whether there are adsorbates present in a given system, them either being unwanted contamination or structures which were deposited on purpose. The descriptions in this section are primarily based on the excellent review by Jona *et al.*[21]

Although both use diffraction to gain information of the underlying system, there are a few key differences between XRD and LEED besides the usage of different incident beams. Where in XRD the energy of the beam is constant and the incident angle is changed, in LEED the

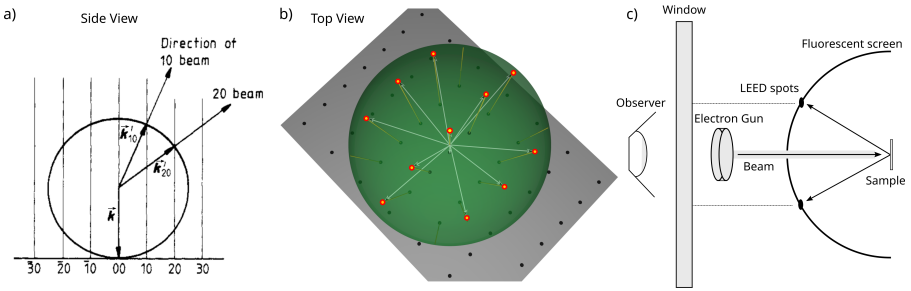

Figure 2.1: a) Shows the Ewald construction on a two dimensional pattern with the incident wavevector $\vec{k}$ and scattered wavevector $\vec{k'}$, reproduced from [21]. b) Shows a 3D view of the Ewald construction with diffraction beams protruding the Ewald sphere and resulting LEED pattern (red dots), taken from [22]. c) Sketch of an experimental LEED setup.

angle is kept constant and the energy is varied. Second, in LEED the material must be measured in ultra-high vacuum (UHV), be single crystalline and the surface must be atomically flat and clean.
While diffraction in three-dimensional space is described by the Laue conditions, in LEED only two conditions have to be fulfilled for diffraction to occur, given by

$$(\vec{k} - \vec{k'}) \cdot \vec{a} = 2\pi m \quad \text{and} \quad (\vec{k} - \vec{k'}) \cdot \vec{b} = 2\pi n \,. \tag{2.1}$$

Here, $\vec{k}$ and $\vec{k'}$ define the incident and scattered reciprocal wavevectors, $\vec{a}$ and $\vec{b}$ are the 2D lattice vectors m and n are integer numbers. The occurrence of diffraction can be visualized with the aid of the Ewald construction, where the Ewald sphere is spanned by the vector $\vec{k}$, as shown in Fig 2.1 a) and b). Visible LEED spots then exactly exist

at the points where this three-dimensional sphere is intersected by the nm diffraction beams, as shown in Fig. 2.1 b). These spots are labeled in terms of their nm values, which correspond to the integer steps of the lattice vectors. With increasing energy/wavevector of the incident beam more spots become visible in LEED, where the sphere intersects higher order diffraction beams. An important takeaway is, that LEED provides a direct observation of the reciprocal lattice in real time.
Finally, Fig. 2.1 c) shows a sketch of the experimental setup. The sample is bombarded with a low-energy electron beam by the electron gun, which also serves as a beam-stop for the direct, back scattered electrons (00-reflex). The beam is then diffracted onto a fluorescent screen which emits visible light that can be observed in real time. Depending on the performance of the system and the composition of the sample, integration times of a few seconds can be necessary to clearly observe all LEED spots.

2.1.2 Graphene

Graphene is a simple system that is well suited as an introduction into LEED explanation and analysis and will therefore be used in the following section. Fig. 2.2 a) shows the real space, two-dimensional lattice of graphene. It crystallizes in a hexagonal honeycomb pattern and consists of two carbon atoms per unit cell (open and colored circles respectively). The lattice vectors $\vec{a}$ and $\vec{b}$ enclose an angle of $\alpha = 120\,^\circ$ and span the two-dimensional unit cell highlighted in red.
With the C–C bond distance $a = 1.42\,\text{Å}$, these lattice vectors are de-

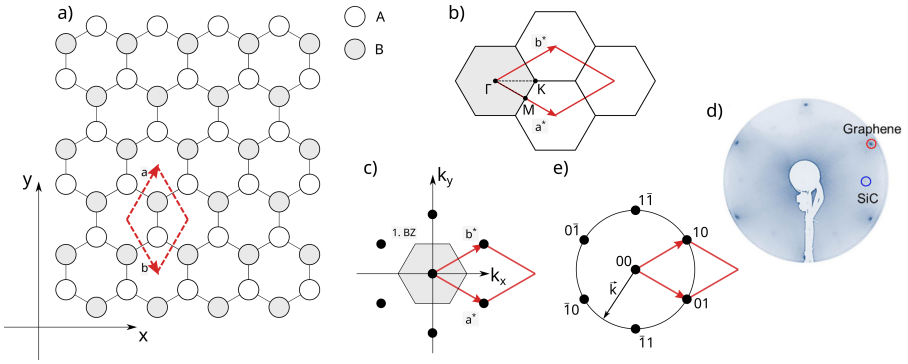

Figure 2.2: Shown are real space structure, Brillouin zone and LEED pattern. a) Depicts the real space lattice of graphene with the lattice constants highlighted in dashed red. b) Shows the reciprocal lattice with the Brillouin zone in gray and reciprocal wavevectors in red. c) Black points indicate LEED spots with the 1. BZ in gray, e) shows indices of the LEED spots on the Ewald sphere. d) Experimental LEED pattern of graphene on SiC, taken from [28].

fined as

$$\vec{a} = \frac{a}{2}\left(\sqrt{3}, 3\right), \ \vec{b} = \frac{a}{2}\left(\sqrt{3}, -3\right), \ |\vec{a}| = |\vec{b}| = a\sqrt{3}\,. \tag{2.2}$$

and the corresponding vectors $\vec{a}^*$ and $\vec{b}^*$ in reciprocal space are given by

$$\vec{a}^* = \frac{2\pi}{3a}\left(\sqrt{3}, -1\right), \ \vec{b}^* = \frac{2\pi}{3a}\left(\sqrt{3}, 1\right), \ |\vec{a}^*| = |\vec{b}^*| = \frac{4\pi}{3a}\,. \tag{2.3}$$

These reciprocal vectors then define the size of the first Brillouin Zone (BZ) and enclose an angle of $\phi = 60°$ as shown in Fig. 2.2 b). Note, that both the real space and reciprocal space lattices posses hexagonal

symmetry. Here, three high symmetry points are defined with Γ having the highest, six-fold rotational symmetry, K three-fold and M two-fold. The lines connecting these points are thus called called high symmetry directions and their determination is a valuable asset of LEED analysis.
Fig. 2.2 c) shows a LEED pattern (black dots), that is obtained by diffraction from a hexagonal crystal structure. Each of the black diffraction spots corresponds to the Γ point of one BZ and their arrangement is determined by the reciprocal lattice vectors, highlighted in red. By connecting lines through these points and drawing perpendicular lines at each midpoint of them, the irreducible BZ can easily be obtained analogous to the Wigner-Seitz cell in a real space lattice.

2.1.3 Interpretation and Superstructures

As already discussed, LEED provides information on the orientation and symmetry of a two-dimensional crystal lattice. These properties can be extracted by simply taking the LEED spots as perfect points with zero lateral expansion. In reality however, these measured spots inherit a spherical spatial distribution which also carries information.
In a perfect, pristine sample the spots possess a small diameter that is only limited by the resolving power of the instrument. The spots can however be "smeared out" in an even pattern around their origin, which can point towards the presence of contaminants on the surface. Since LEED has to be performed in UHV conditions, these contaminants are likely not to originate from the surrounding vacuum but from still being attached to a sample from its past exposure to ambient conditions. If

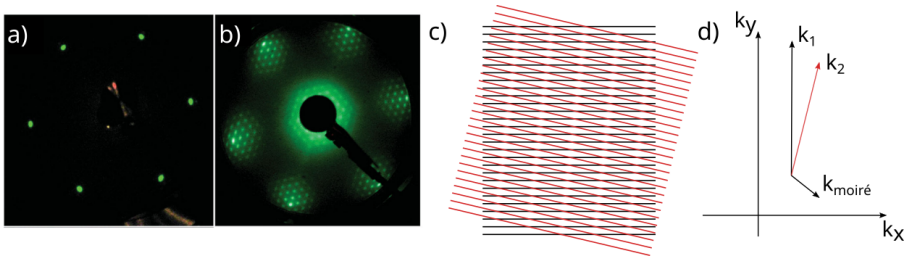

Figure 2.3: a) Shows the LEED pattern of a hexagonal structure (Ru(0001)), taken from [29]. b) Shows the LEED moiré pattern of a hexagonal structure with another hexagonal structure absorbed on top of it (graphene/Ru(0001)), taken from [29]. c) Shows a simple model of a moiré pattern (upper) with d) matching k vectors, reproduced from [30].

possible, the sample must then be cleaned further, usually by means of Ar^+-ion bombardment (sputtering) and heating to elevated temperatures (annealing). If after further cleaning the LEED spots are still not sharp, it indicates low crystallinity of the underlying sample.
Another indication of low crystallinity is the presence of a ring-shaped feature that spans between all LEED spots. This is due to the presence of multiple domains which are rotated against each other, thus contributing with slightly twisted, weaker LEED spots, resulting in a circular image appearance.

Increasing complexity of a sample in the form of adsorbing a second, foreign and ordered structure onto the pristine material can also be evaluated using LEED. Here, the interplay between both structures can be used to understand the orientation and growth behaviour of two materials. Fig. 2.3 contains two sets of data where the left shows a pris-

tine structure with hexagonal symmetry and the right a multi-layered system, where another structure was deposited on the pristine material. Starting with the pristine LEED (the composition of the material is not relevant for this discussion) the hexagonal lattice is clearly recognizable and the LEED spots are sharp, indicating high sample crystallinity and it being free from contaminants.
On the right hand, the same bright spots can still be seen at the edge of the screen together with a multitude of additional new spots. The new spots show very small separation in the LEED image, so their real space distance is large. However, the layers that was evaporated on top of the inital one does not exhibit this massive lattice spacing. It is much rather known as a moiré pattern.[30] This pattern forms whenever two lattices with different lattice constants overlay each other over very long distances, as shown in the sketch in Fig. 2.3 c). The appearance of a moiré pattern thus proves very high order between two lattices on a global scale and can be described by a new wavevector $k_{moiré} = k_1 - k_2$. This is what makes LEED a powerful tool for characterization of two-dimensional crystal structures on a large scale.

2.2 Photoemission Spectroscopy

In 1887, H. Hertz observed that ultraviolet (UV) radiation interacts with electrons by measurement of an electric current when a metal was irradiated.[31] It took until 1905 when A. Einstein described this phenomenon as the photoelectric effect. The discovery of this effect and the correct description of the photon lead to him being awarded the Nobel price in 1921.[32] Since then, advancements in experimental techniques have made the electronic structure of numerous materials easily available to scientists and therefore the theoretical basis as well as experimental details will be described in the following section, which is mainly based on the review paper [33] by A. Damascelli *et al.*
The photoelectric effect is described by the relation

$$E_{\mathrm{kin}} = h\nu - \phi - E_{\mathrm{B}} \ , \tag{2.4}$$

where the kinetic energy E_{kin} of an emitted electron is defined by the excitation energy $h\nu$, the work function ϕ and its binding energy E_{B}. This simple description is depicted in Figure 2.4 a). In any crystalline solid, electrons are bound at various levels with their respective binding energy E_{B} which increases for electrons closer to the nucleus (core levels). The filling of electrons into levels continues up to the Fermi-Energy E_{F} after which no electrons are bound anymore. Shining light with energy $h\nu$ onto the material can excite electrons with a maximum energy of $h\nu - \phi$ where ϕ is the workfunction (this corresponds to $E_{\mathrm{B}} = 0$ in Eq. 2.4) i.e. higher excitation energies are necessary to release electrons with higher binding energy. This in turn means that the energy of the excited electron is only dependent on the energy of the incoming light,

not its intensity, which is proportional to the number of emitted electrons. This is why a highly intense light source is desirable for high quality measurements.

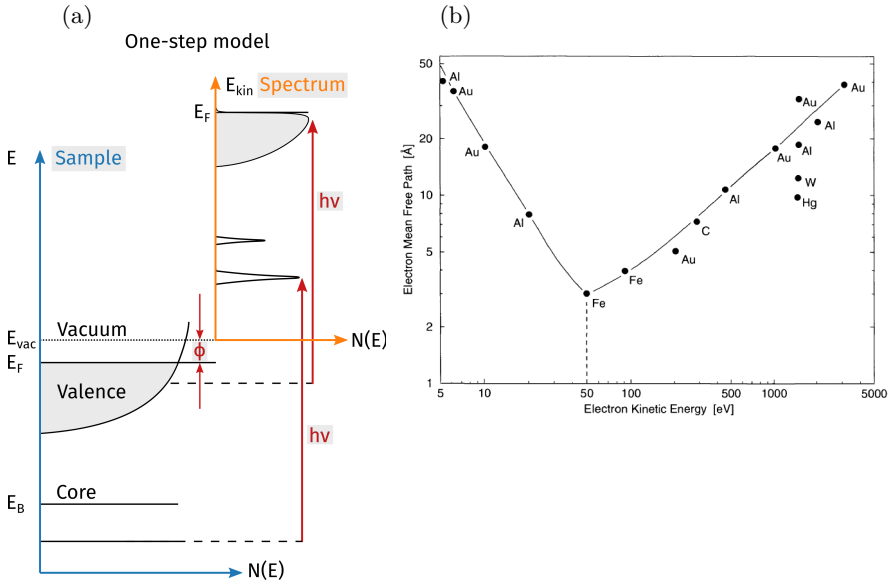

Figure 2.4: a) Shows a schematic of the photoemission process as described by the one-step model. E_{B} denotes the binding energy of electrons at various levels, EF the energy of the Fermi level, E_{vac} the energy at the vacuum level, which is separated from the Fermi level by the workfunction ϕ and N(E) is the number of electronic states. b) Shows the universal curve of the inelastic mean free path of electrons in solids.[34]

The probability of photoexcitation is given by Fermi's golden rule[33]

$$\omega = \frac{2\pi}{\hbar} \left|H_{\text{int}}\right|^2 \delta(E_f - E_i \pm h\nu) \tag{2.5}$$

$$\text{with} \;\; H_{\text{int}} = -\frac{e}{mc} \langle \psi_f | \mathbf{A} \cdot \mathbf{p} | \psi_i \rangle \,, \;\; \mathbf{p} = -i\hbar\nabla \tag{2.6}$$

which describes the transition of an electron from an initial state ψ_i to a final state ψ_f based on the electronic momentum operator $\mathbf{p}$ and the electromagnetic vector potential $\mathbf{A}$. Note that this equation is only valid using the dipole approximation which states that $\mathbf{A}$ is constant over atomic distances in the bulk (this holds for UV radiation). However, at the interface between bulk and vacuum (surface) this approximation can break down due to the discontinuity of the dielectric function ϵ [35] and a more complex description known as the *one-step model* should be used, in which one Hamiltonian is used to describe the processes in the bulk, surface and vacuum. Since this description is rather complex, a discussion of the photoemission process within in the *three-step model* is more convenient. This model separates three independent steps:

i) Optical excitation of an electron in the bulk.

ii) Travel of the electron to the surface.

iii) Transition of the photoelectron from surface into vacuum.

While this model gives a concise mathematical description of the photoemission effect, it is beyond the scope of this short introduction and the model will rather be used to explain actual photoemission spectra. In step i) an electron is excited in the bulk which contains all information about energy E_{kin} and momentum k of the electronic structure of

the studied material. So if this particular electron can me measured by an analyzer it is a direct representation of the exact electronic state of the electron in the material. In order to be measured, the electron has to travel through the bulk up to the surface, as given by step ii). In an ideal, non-interacting material at $T = 0\,\mathrm{K}$ the electron reaches the surface unperturbed. In reality however, the interaction of the electron with other electrons causes incoherent scattering, which leads to a broadening of the resulting spectral function. Additionally, some of the photoelectrons never reach the surface as expressed by the the inelastic mean free path (IMFP), that relates the intensity of the photoelectron I to the the initial intensity I_0 via a Lambert-Beer like expression as

$$I = I_0 \cdot e^{\frac{-x}{\lambda}}, \tag{2.7}$$

where λ is the IMFP. The IMFP of an electron in a solid is given by the universal curve as depicted in Fig. 2.4 b). In the range of 10 – 1000 eV (which is common for photoemission spectroscopy) the electrons only travel on the order of $\sim 10\,\text{Å}$ until their energy decays, which makes the method extremely surface sensitive.[34]

Once the electron reaches the surface, it transitions from the surface into the vacuum, as stated by step iii), and the energy required for this transition is given by the material specific work function ϕ. Here, the conservation of momentum is well defined and is described in a later of this section.

There are three different photoemission spectroscopy methods which are commonly used for determination of various aspects on the electronic structure of solids, namely X-Ray Photoemission Spectroscopy

(XPS), Ultraviolet Photoemission Spectroscopy (UPS) and Angle Resolved Photoemission Spectroscopy (ARPES).

As the name implies, XPS uses X-Rays as the photon source, which are in the energy range of $\sim 1000\,\mathrm{eV}$. These photons can be generated by common X-Ray cathodes or preferably using synchrotron radiation. Here, the synchrotron light has the advantage of inherent higher *brilliance*, which is defined as the number of photons emitted per unit source area over a unit angle of emission per uni energy (photon s^{-1} mrad^{-2} mm^{-2} per 0.1% radiation bandwith).[36] The use of high energy photons allows for this method to study the electronic structure of orbitals with high binding energy (core levels). This information is valuable in examination of the chemical state of a material i.e. which elements are present and what are their oxidation states.

High energy photons however come with the drawback of a relatively high energy distribution on the order of $\Delta E \approx 700\,\mathrm{meV}$ for cathode based radiation or $\Delta E = 50\,\mathrm{meV}$ with the use of a monochromator.[37] Even with the use of synchrotron radiation, the energy resolution of hard X-rays lies in the range of a few tens of meV. While this is not critical for analysis of core levels it is impossible to study changes of a few meV close to the Fermi-Level. This is where the usage of UV light in a UPS experiment makes a significant difference. The most common light source for a lab based setup is a Helium discharge lamp, which yields two main lines He I (21.2 eV) and He II (40.8 eV) with a band width of only $\sim 3\,\mathrm{meV}$[38] that can be further reduced using a monochromator (at the cost of intensity). Synchrotron based light can reduce this width even further and the combination with a high resolution hemispherical analyzer ($\Delta E < 1\,\mathrm{meV}$) enables the study of slight

changes to the electronic structure with high precision.

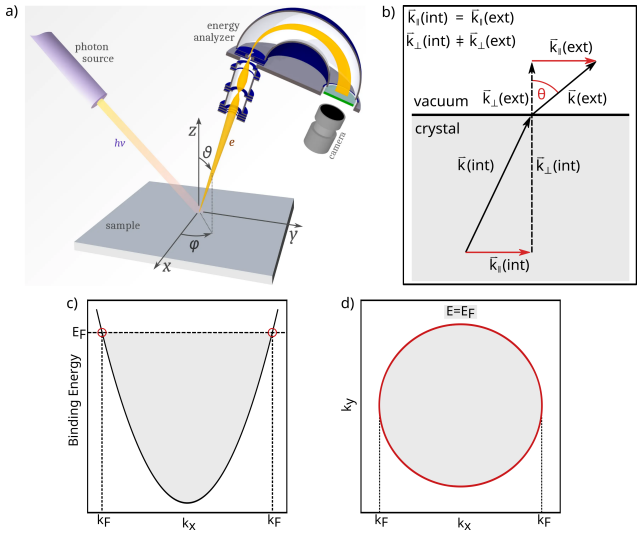

Figure 2.5: a) Sketch of an ARPES setup, taken from [39]. b) Behaviour of the electron momentum when crossing the crystal surface. c) Sketch of the measurement of a parabolic band. d) Equi-energy cut through a parabolic band at the Fermi level.

Let us take a step back and focus again on the exact process of step iii) of the photoemission process, where the electrons crosses the surface while transitioning from the crystal to vacuum. In this process the momentum component perpendicular to the surface $k_\perp$ is not conserved but the component parallel to the surface $k_\parallel$ is, because the $k_\perp$ part is altered while crossing the surface from the material to vacuum, as depicted in Fig. 2.5 b). This detail is crucial in order to obtain the correct energy-momentum relation of a measured photoelectron, which

is given by

$$k_{\parallel} = \sqrt{\frac{2m_e}{\hbar^2} E_{\text{kin}}} \cdot \sin\theta = 0.512\sqrt{E_{\text{kin}}} \cdot \sin\theta \ . \tag{2.8}$$

The use of a hemispherical analyzer not only allows for resolving electrons in the energy direction but also in the direction of the angle at which the electrons left the sample. The inclusion of this second data axis as well as the precise knowledge of the sample orientation with respect to the electron analyzer is known as Angle-Resolved Photoemission Spectroscopy (ARPES). A sketch of an ARPES setup is depicted in Fig. 2.5 a). A light source irradiates the sample and photoexcited electrons leave the surface in all directions. The electron analyzer collects electrons with a defined angular and energy distribution around a central excitation angle θ (polar angle). Electronic lenses inside the analyzer guide the electrons to a phosphorous film (after being multiplied by a multi channel plate), which acts as a screen and lights up when hit by the electrons due to phosphorescence. This signal is then picked up by a CCD camera and results in detection of a two-dimensional image. A sketch of such an image is shown in Fig. 2.5 b), here for the case of a perfect electron gas. The detected image shows the kinetic (binding) energy on the y-axis and angle (momentum) on the x-axis. The analyzer also houses a rectangular slit that is large in one direction (on the range of cm) and very narrow in the other (few µm). This allows for only picking up electrons with angular distribution in the direction of the long axis of the slit e.g. the k_{x} direction, while the k_{y} distribution is so small that it can be described as a single value that corresponds to a specific sample rotational angle. The sample can then be rotated along

the direction of the small axis of the slit to access different k_y values. The process of taking a lot of E vs k_x images along the k_y direction (or vise versa) is called *mapping*. With the exact knowledge of the rotation angles it is possible to combine this set of images into a three-dimensional cube, where the axis describe k_x, k_y and E. This 3D data set can then be *sliced* in any direction to access either the energy distribution along different high symmetry direction or to produce equi-energy contours, one of which is depicted in Fig. 2.5 c) for the case of a slice at the Fermi surface.

2.3 Raman Spectroscopy of Carbon Nanostructures

Spectroscopy is the general term for studying the interaction of radiation with matter. One of these interactions is the scattering of photons with phonons, which are the quantized lattice vibrations. Sir Chandrasekhara Venkata Raman found that this process can either happen elastically or inelastically and his research was rewarded with the Nobel price in 1930.[40] The intensity of the inelastically scattered light however is a factor $\sim 10^7$ smaller than that of the incident light. While Raman discovered the effect using focused sunlight, it took until 1960 when the invention of a high intensity light source, namely the laser, made using this effect easily accessible.[41]

All light is classified as electromagnetic radiation which is most simply described as sinusoidal waves of both the electric and magnetic field. While the amplitude of the magnetic part of this radiation is negligible for most light-matter interactions, the alternating electric field is

strong enough to induce local, oscillating dipole moments in the electric fields of molecules. This on the other hand causes vibrations in the affected molecule if resonance conditions of the light's frequency and the molecule's phonons are fulfilled. Depending on the structure of the target, these vibrations can have two effects.
If there is already a dipole present, say in a polar C=O bond in Acetone, then the incoming light can modulate this already existing dipole moment, is therefore absorbed and transferred to the molecular structure and falls into the selection rules of Infrared Spectroscopy (IR). This method uses a polychromatic, infrared light source and monitors the strength of absorption as a function of the incoming wavelength.[42]
On the other hand, if there is no dipole present in a molecule, for example in the diatomic N_2, no such absorption can happen. The light can however induce a deformation of the electron cloud, which creates a local dipole since the negative electron cloud moves about the positive cores and is therefore an off-resonant interaction that is induced by the incoming, oscillating electric field of light with a fixed frequency ν.[42]
The size of the dipole moment $\mathbf{P}$ depends on the polarizability α of the molecule and the magnitude of the incoming electric field $\mathbf{E}$ *via* [43]

$$\mathbf{P} = \alpha \mathbf{E} \, . \tag{2.9}$$

The magnitude of the electric field of light with frequency ω is given as

$$\mathbf{E} = \mathbf{E_0} \cos(\omega t) \tag{2.10}$$

and the polarizability can be described as the deformability of an electron cloud under the effect of an external electric field. In detail, this

depends on the exact geometry of the molecule and the induced vibrational frequency ω_{vib} and is described as

$$\alpha = \alpha_0 \cos(\omega_{\text{vib}} t) \tag{2.11}$$

and yields the final description of the polarization as

$$\begin{aligned} \mathbf{P} &= \alpha_0 \mathbf{E}_0 \cos(\omega t) \cos(\omega_{\text{vib}} t) && (2.12)\\ &= \frac{1}{2}\alpha_0 \mathbf{E}_0 \big[\underbrace{\cos\big((\omega + \omega_{\text{vib}})t\big)}_{\text{Anti-Stokes}} + \underbrace{\cos\big((\omega - \omega_{\text{vib}})t\big)}_{\text{Stokes}} \big] && (2.13)\\ &= \frac{1}{2}\alpha_0 \mathbf{E}_0 \cos\big((\omega \pm \omega_{\text{vib}})t\big). && (2.14) \end{aligned}$$

This results in emission of light with a different wavelength than the incoming one which of course is in relation to the affected, oscillating bond and this inelastic effect is called Raman scattering. Raman spectroscopy therefore uses a monochromatic laser light source and detects emitted frequencies different from the incoming one. It does not require modes that carry a dipole moment and therefore makes it the perfect tool for characterization of purely Carbon based structures such as graphene, graphene nanoribbons or C_{60}.

Fig. 2.6 shows a typical Raman spectrum with the underlying scatterin processes. The very intense line at $\nu = 0\,\text{cm}^{-1}$ is caused by Rayleigh scattering where the incoming light is absorbed and scattered elastically so that the frequency of the scattered light does not differ from the incoming. This process is the most probable in any solid and is therefore much more intense than any Raman scattering process.

The peaks on the right hand side of the spectrum are caused by Stokes

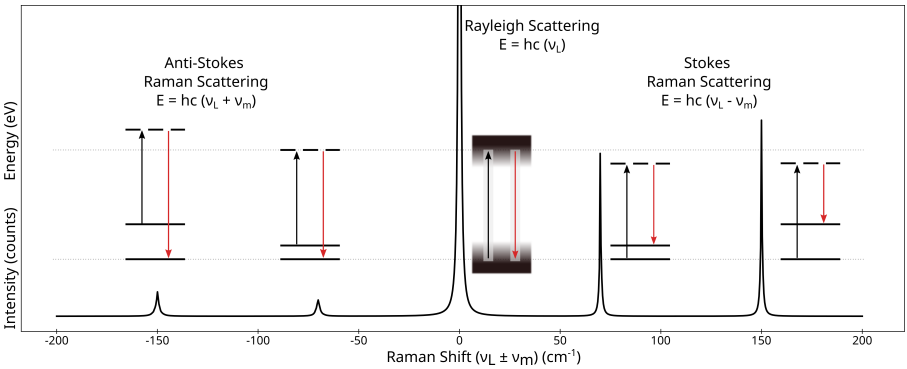

Figure 2.6: Shown is an exemplary Raman spectrum with assignment of different scattering processes. Black line with Lorentzian peaks shows the Raman spectrum. Horizontal, solid lines show ground states with different excitation levels, dashed horizontal lines indicate virtual states. Black arrows show the incoming laser light, red arrows the scattered light.

scattering in which the incoming photon elevates an electron from some *ground* state to a higher, *virtual* state. The electron then falls back into a higher *excited* state and, due to conservation of energy, releases light with a characteristic frequency that is lower (less energetic) than the laser light. This means that the position of a Stokes peak (its frequency) contains the information about a specific vibrational state. The intensity of the respective peak is governed by the intensity of the incoming light as well as the number of equal scattering sites (bonds).

The third process on the left hand side is called the Anti-Stokes scattering, where an electron from an elevated vibrational state is lifted to a virtual state and then falls back to a lower vibrational state, therefore emitting light with a higher frequency (higher energy) than the

incoming one. For every Stokes peak, there exists an accompanying Anti-Stokes one with negative frequency. The ratio between the intensities of the two is described by Boltzmann's–Law and given as

$$\frac{I_{\mathrm{AS}}}{I_{\mathrm{S}}} = \exp\left(\frac{-E_{\mathrm{ph}}}{k_{\mathrm{B}}T}\right) . \tag{2.15}$$

It follows, that the intensity of the Anti-Stokes peak increases at higher temperatures since this is where electrons exist in higher vibrational states already. It is also clear, that it is possible to determine the temperature of a sample by careful analysis of the intensity ratios of the Stokes and Anti-Stokes lines.

Due to its high symmetry, (pristine) graphene exhibits only a few observable peaks in Raman scattering and thus makes for an excellent example for introduction to experimental Raman spectra. Furthermore, the nomenclature of carbon nanotubes and graphene nanoribbons is derived from that of graphene, so knowledge of the graphene naming conventions is critical to understanding that of GNRs. Fig. 2.7 (upper) shows the Raman spectrum of a defect-free graphene monolayer which consists of two major peaks namely G at $\sim$1580 cm^{-1} and 2D at $\sim$2690 cm^{-1}.[45] The G peak (name based on *Graphene*) corresponds to a high frequency, in-plane phonon at the Γ point. It is an E_{2g} optical mode that is Raman active only, as shown in Fig. 2.7 b). Another in-plane vibration is shown in Fig. 2.7 c) and called *breathing* mode. This simultaneous, symmetrical vibration is not Raman active as is and is only activated through defects in the graphene structure and is aptly named D peak (based on *Defect*). The 2D peak in pristine graphene

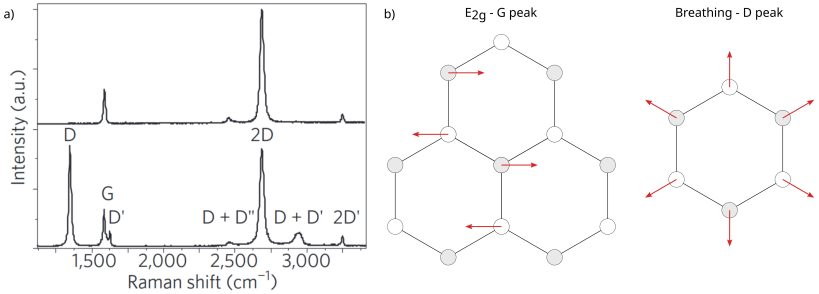

Figure 2.7: a) Raman spectra of pristine (upper) and defective (lower) graphene, taken from [44]. b) Raman active phonon modes in graphene, adapted from [44].

however is Raman active even without defects, since it is the D overtone. This process involves scattering between two K valleys and since it is a two phonon process, momentum conservation is satisfied even in the absence of any defects.[44, 46, 47]

Upon introduction of defective sites, more Raman peaks are visible in a spectrum, namely the D, D', D+D", D+D' and 2D' peaks, as shown in Fig. 2.7 a) (lower). These peaks correspond to phonon activated intra- and intervalley scattering processes.[45–47] By comparison of the intensities of the D and G peaks (D/G ratio), the quality of a graphene monolayer can easily be accessed by Raman spectroscopy.

By altering the structure of graphene i.e. rolling it up into carbon nanotubes or reducing its lateral size into graphene nanoribbons, more defect-like peaks appear. These peaks for example correspond to a specific nanoribbon width or edge termination and can therefore be used as *fingerprint* modes to access properties of graphene like structures.

The calculated Raman spectra with corresponding lattice vibrations

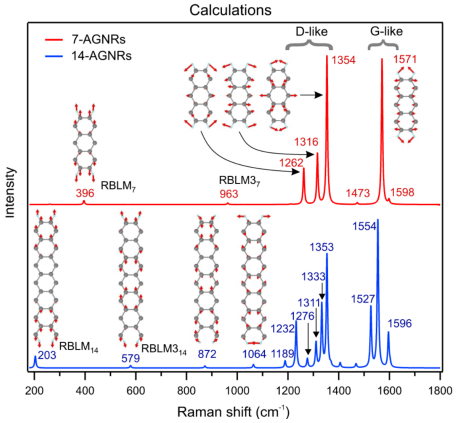

Figure 2.8: Calculated Raman spectra of (upper) 7-AGNR and (lower) 14-AGNR, showing the RBLM, D-like and G-like peaks with corresponding lattice vibrations, taken from [17].

of a 7-armchair graphene nanoribbon (7-AGNR, upper) and 14-AGNR (lower) are shown in Fig. 2.8. The peaks around $\sim$1570 cm^{-1} are called G-like due to their close resemblance to the G peak of graphene. The same naming scheme holds for the D-like peaks around 1350 cm^{-1}. At 396 cm^{-1} the radial breathing like mode (RBLM) appears in the case of 7-AGNRs and is directly tied to the width of the nanoribbon. Increasing width leads to a shift of the RBLM towards lower frequencies and therefore acts as a fingerprint for determination of a graphene nanoribbons' width. The origin of the naming convention of the RBLM lies in its first appearance in cylindrical carbon nanotubes, where it is tied to the radius of the tube and was adapted in the case of graphene nanoribbons.

Observation of the RBLM mode of specific nanoribbons is however not

possible with any laser, since it is enhanced by resonance Raman scattering.[43, 48–50] In this process, a photoexcited electron undergoes electron-phonon interaction and scatters to a virtual state before recombining. This is possible if the energy of the exciting (laser-)light is close to an existing electronic transition and is therefore directly tied to the electronic band structure of the GNR. In a simple model, the band gap decreases with increasing GNR width (described in more detail in Section 3.1) and therefore a laser with appropriate energy must be chosen to enable the resonant Raman process. In the case of 7-AGNRs, a 532 nm (2.33 eV) is ideal for measurement of all modes including the RBLM, whereas for a 14-AGNR the RBLM is only visible using a less energetic 633 nm (1.96 eV) laser.

Chapter 3

Material systems

3.1 Graphene Nanoribbons

Since the discovery of Graphene by Novoselov and Geim in 2004 [51], the interest in low-dimensional carbon based systems has risen dramatically. While graphene itself holds manifold interesting properties, there is a limited range of modifications that can be done to its electronic structure. Furthermore, any defects in its structure can drastically change its electronic properties, which is why related structures were investigated. Here, carbon nanotubes, which resemble rolled up graphene sheets, lead towards defect free carbon structures whose quasi-1D structure plays a role in quantum confinement.[52] This confinement results in discrete electronic states which heavily depend on the size of the nanotube and possible modification with heteroatoms.

Another 1D carbon structure comes in the form of Graphene Nanoribbons (GNRs), which are quasi-infinite in one direction but have a defined width and shape in the other. This limitation in width also leads to quantization of electronic states and therefore drastically changes the electronic structure in comparison to graphene. By precisely tuning the shape of the edge of a ribbon, manifold electronic systems can be realized.[20, 53]

Fig. 3.1 depicts nanoribbon systems of different width and edge termination. The two most simple systems are the Armchair Graphene Nanoribbons (AGNRs) and the Zigzag Graphene Nanoribbons (ZGNRs), whose naming schemes originate from their edge terminations. Here,

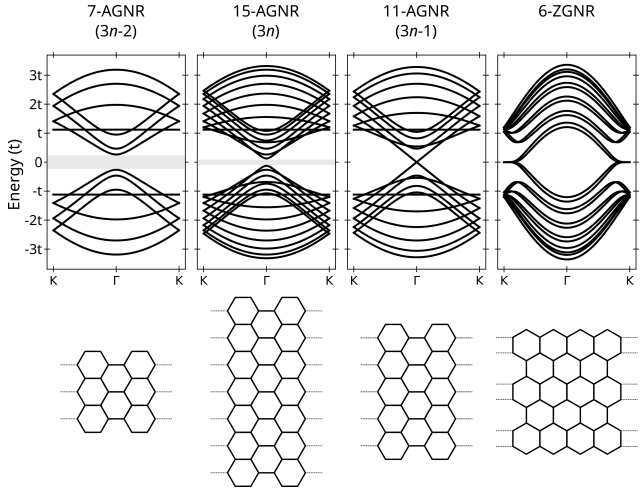

Figure 3.1: Tight-binding calculations of the electronic energy bands for different nanoribbons (upper) and corresponding structures (lower). The empirical hopping parameter t defines the orbital overlap.

AGNRs resemble the top-down view onto a chair with armrests and ZGNRs the cutting edge of a knife. The difference in edge termination has large influence on the electronic structure of the system, where most AGNRs are semiconductors whose bandgap scales inversely proportional to the width of the ribbon. ZGNRs on the other hand are metallic or quasi-metallic with a flat band forming at the K point. These electronic states are located on the zigzag edge of these ribbons and are predicted to be spin-polarized, rendering them interesting for use in spintronics. These systems were theoretically investigated by Kane and Mele [54] with respect to their topological order and possible realization of the quantum spin hall effect. In the case of AGNRs, their semiconducting nature breaks down for ribbon widths equal to $3n-1$[19] where

n is an integer number, as shown in Fig. 3.1. This shows, that precise control over the ribbon width and edge termination is crucial to studying and manipulating their electronic structures.
Initially, GNRs were obtained by cutting sheets of graphene into shape using optical lithography.[55] Here, a large sample area is covered in a photosensitive solution (photoresist) in any desirable form and shape and developed using light. The generated, solid mask acts as a protection for a following etching step, in which anything not covered by the mask is removed. Afterwards the mask is dissolved again, yielding a clean, patterned carbon structure. This process has already been heavily optimized by the semiconductor industry and although its high throughput rate and large sampling area provide an excellent basis for modification of graphene sheets, the major drawback lies in its inherent "low" resolution that is governed by the wavelength of the light. Therefore it is impossible to produce GNRs with consistent size and edge termination on the atomic scale using this method.

The search for more control lead to the realization of novel methods (compare Fig. 3.2):

i) Unzipping of carbon nanotubes.

ii) Epitaxial growth from 4 H−SiC substrates.

iii) CVD growth.

iv) Bottom–up fabrication from precursor molecules in UHV.

For the synthesis of GNRs by unzipping of carbon nanotubes, a set of tubes of fixed dimension is first suspended in concentrated sulfuric

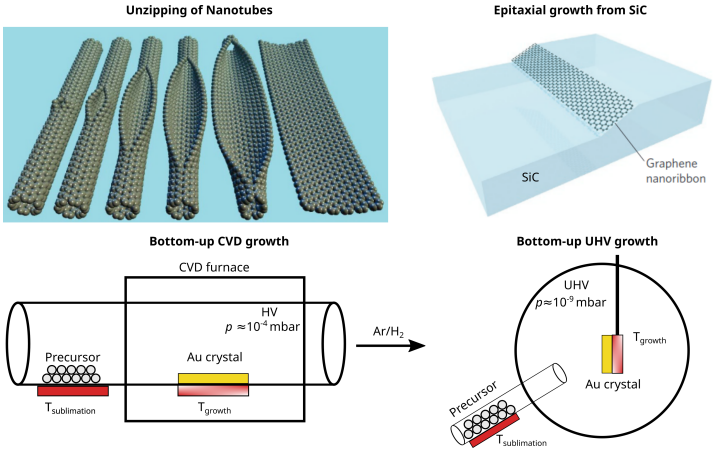

Figure 3.2: Sketches of different methods of top-down and bottom–up synthesis routes. Top left is taken from [56], top right taken from [57], bottom left reproduced from [58], bottom right is own work.

acid. The addition of $KMnO_4$ leads to oxidation of the nanotubes which starts at a random spot along the tube. It was found that for further oxidation it is more energetically favourable to occur along a straight line in the direction of the long axis of the nanotube, which results in the length-wise unzipping of the nanotube.[56] This yields an oxidized GNR whose size is confined by the width of the original carbon nanotube. After reduction, the final GNRs can be deposited on any substrate for further use.

While this solution based method is able to produce a vast amount of GNRs in a small period of time, the lacking spatial order of the produced GNRs makes it hard to use this approach for consistent device fabrication. Additionally, the minimum GNR width achievable with

this method is limited by the smallest size of carbon nanotube available and the control over the edge state is not trivial.
A different approach lies in the epitaxial growth of GNRs from 4 H – SiC substrates. Here, SiC serves both as a carbon source as well as a template structure for the ordered growth of nanoribbons. The surface of silicon carbide readily produces step-like, slanted terraces at an angle of $\sim 25°$, whose formation is understood as minimization of surface free energy and ultimately originates from its crystal structure.[57] This behaviour can be exploited by first etching a 90° step into the surface of the crystal with a specific depth, which is done with nanometer precision using lithographic preparation of nickel lines with following fluorine etching. Through careful annealing at elevated temperatures ($\sim 1300\,°C$) the cuts relax into slanted "nano-facets" whose length depend on the depth of the prior etching step. By further controlled increase of the temperature, carbon is released from the crystal and forms nanoribbons selectively along the more reactive facets of the substrate.
A major advantage of this technique is the ability to produce (slanted) circuits on an SiC substrate through the lithographic process and therefore design a device structure for the nanoribbons to grow in.[57] However, the control over the width of the ribbon is still limited by a lithographic process and the precise control over edge states is not trivial.
Today, the most precise way of synthesizing GNRs is based on bottom–up synthesis in UHV, followed by CVD growth in a furnace. Both methods are based on the same principle, in which the design of a molecular precursor dictates the outcome of the final GNR. Fig. 3.3 shows the reaction mechanism of the bottom–up process and will be discussed here on the example of 10,10'-dibromo-9,9'-bianthracene (DBBA) to 7-

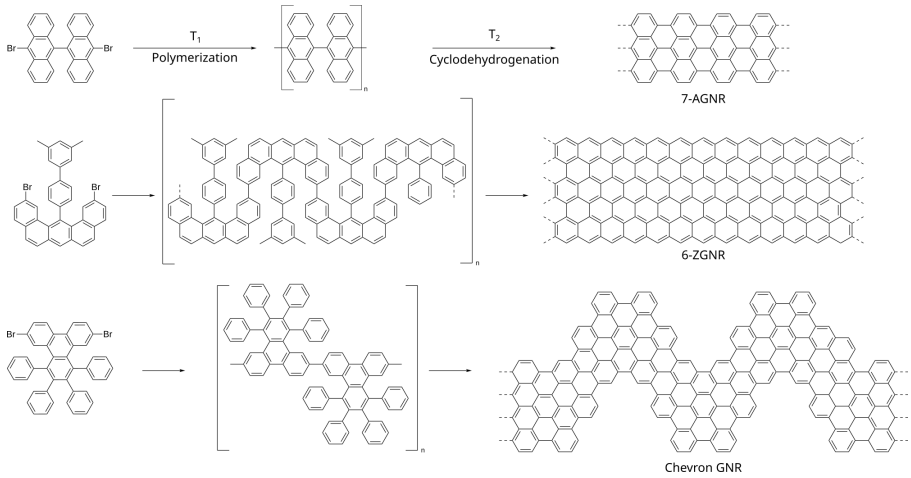

Figure 3.3: Reaction mechanism from precursor to 7-AGNR (upper), 6-ZGNR (middle) and Chevron GNR (lower).

armchair graphene nanoribbon (7-AGNR) conversion. The precursor is first deposited onto a gold substrate either in UHV or my means of chemical vapor transport.[53] Both single crystal bulk Au(111) and aligned Au(788) crystals or thin films of well ordered Au on MICA (muscovite, $KAl_2(AlSi_3O_{10})(F, OH)_2$) can serve as this substrate, where highly crystalline samples yield highest quality GNRs. After deposition, the precursor, through heating, reacts in an Ullmann-type fashion along the halogen sites, where Au acts as a catalyst.[59, 60] This forms a long, non-planar polymer which can still freely rotate around the linkage C – C bond. Further well controlled heating promotes cyclodehydrogenation, which results in the formation of new bonds thus forming the final, planar GNR.

The quality of the resulting ribbon is mainly determined by the purity of

the precursor molecule and the growth conditions. High quality precursors can be synthesized through organic chemistry and purified following standard techniques with some of the most common ones (like DBBA) even being commercially available.[61] Cleanliness during growth is ultimately high under UHV conditions, which is why highest quality GNRs can be grown under such albeit at high costs in experimental setup. CVD on the other hand has the advantage of a less complex and costly setup, which allows much higher throughput. Another major factor is optimization of the growth in terms of reaction temperatures. While these lie in the same range from 200 °C to 400 °C for most ribbons, the exact and best temperatures vary between molecules. Some GNRs, especially those incorporating heteroatoms such as boron or nitrogen are volatile and can break down under exposure to high temperatures. Other GNRs, such as the 7-AGNRs, can be fused into wider ribbons, with n times its size, i.e. 14-AGNRs and 21-AGNRs through further cyclodehydrogenation.[17] Precise and quick control over the reaction temperature is key to obtaining pristine products.

3.2 Buckminsterfullerene C_{60}

C_{60} is a member of the fullerene family of carbon materials whose members form large structures only based on carbon that is connected by single and double bonds. These unsaturated carbon structures were long thought to not be stable until the discovery of C_{60} by R. Smalley *et al.* in 1985 [62], which then paved the way for structures such as graphene, carbon nanotubes and graphene nanoribbons. The molecules' structure comes in the form of a truncated icosahedron, consisting of pentagons and hexagons, which is commonly known as the geometry of a standard soccer ball. It was aptly named as the Buckminsterfullerene (Buckyball) after the architect Buckminster Fuller, whose works resemble that particular icosahedral shape and the scientists were awarded the Nobel price in chemistry in 1996. Ever since, C_{60} has sparked major interest in all fields of natural sciences. In biology, it was used for encapsulation of small molecules[63, 64] and as an antioxidant agent.[65, 66] In chemistry, manifold functionalization and incorporation of heteroatoms[67, 68] was explored whereas in physics, the interesting optical and electronic properties[69] were explored, the latter of which will be covered in the following part of this thesis.

Whereas the atomic structure of the C_{60} molecule is made up of 12 pentagons and 20 hexagons, its atomic structure is governed by single and double π-bonds. One would assume that this large arrangement of π-bonds would form a large, "superaromatic" structure, but it was found that the double bonds do not form across the pentagon sites. This results in low electron delocalization that can in part explain its optical absorption properties and which makes it a good electron accep-

tor. Cyclic voltammetry studies found that C_{60} can easily be ionized and will accept as much as six electrons per molecule.[70] This fact can easily be understood by investigating the Hückel molecular orbitals as shown in Fig. 3.4. The 60 π-bonds that are available in C_{60} completely

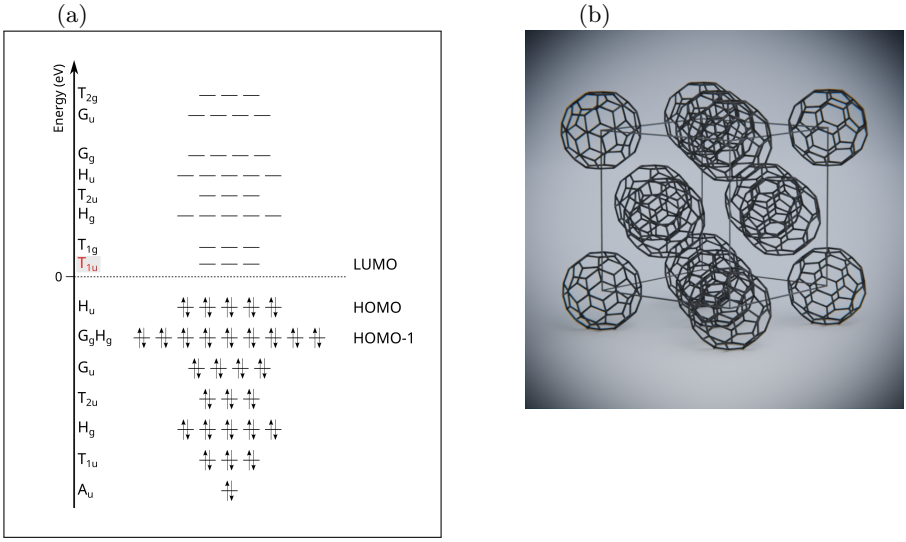

Figure 3.4: a) Hückel Molecular Orbital scheme of C_{60}, adapted from [71]. b) Crystal structure of C_{60}.

fill up the 30 lowest lying orbitals with the highest occupied molecular orbital (HOMO) being the H_u. The three fold degenerate T_{1u} is the lowest lying unoccupied molecular orbital (LUMO) and can therefore accept up to six electrons.[71] In its pristine, undoped state C_{60} is a semiconductor with an optical (direct) bandgap of 1.6 eV and an electronic (indirect) bandgap of 2.3 eV.[69] Filling the LUMO with three electrons then creates a half-filled state, which converts the ${C_{60}}^{3-}$ into a

metallic state and further doping results in an insulating $C_{60}{}^{6-}$ phase. In order to study electronic bands, the molecules must of course be condensed into crystals or ordered thin films. In bulk, the molecule crystallizes in a face-centered cubic (fcc) structure at room temperature, as shown in Fig. 3.4. Due to the large van der Waals diameter of 1.1 nm of a single buckyball [72], the lattice constant of the fcc crystal comes in at $a = 14.12\,\text{Å}$.[62] This large spacing is sufficient for smaller molecules or atoms to intercalate between the buckyballs, making it an ideal structure for ordered assembly of co-atoms.

In the case of thin films, C_{60} is known to form hexagonal pattern.[73, 74] These pattern correspond to the $C_{60}(111)$ direction of the bulk crystal and are described by a vector with length $|\vec{b}| = \frac{\sqrt{2}a}{2} = 9.98\,\text{Å}$. The growth of C_{60} thin films has been studied on a wide range of metals and semiconductors such as Au(111)[75], Cd(0001)[76] and hBN/Rh(110)[77] and optimization of growth in different systems is key to obtaining higher performance devices. Depending on the specific material, C_{60} usually binds via physisorption and is found to exhibit interesting superstructures and moiré pattern all of which prove high symmetry and ordered growth. This high degree of order can on the one hand improve performance of the thin film as a transistor and on the other hand provide a highly ordered, semiconducting template for assembly of more complex structures. Here, the functionalization of C_{60} with organic groups or the incorporation of metallic atoms creates a new, well ordered system for further studies.

3.3 Organic Superconductor Rb_3C_{60}

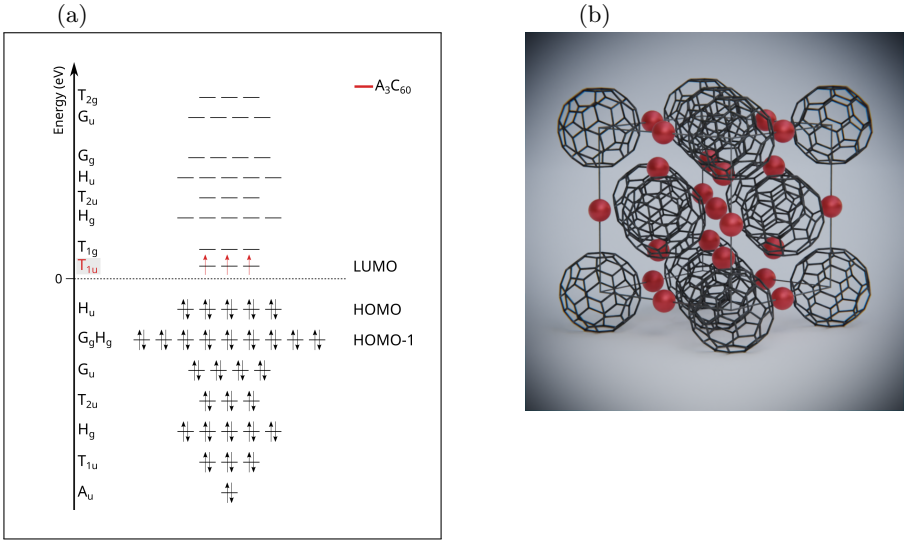

Figure 3.5: a) Hückel Molecular Orbital scheme of A_3C_{60}. b) Crystal structure of A_3C_{60}.

One C_{60} derived system is A_xC_{60}, where A is an alkali metal (K, Rb or Cs) and x is an integer number from 1 to 6.[78] As discussed above, C_{60} acts as a good electron acceptor and takes up to six electrons where every alkali atom each donates a single electron. Thus, a A_3C_{60} system is metallic since the T_{1u} MO is half filled, acting as the new valence band as shown in Fig. 3.5 a). Further doping results in a fully saturated A_6C_{60} phase with the T_{1u} fully filled, yielding an insulating system. Species with alkali metal numbers different from 3 and 6 are mostly unstable at room temperature and ambient pressure. Due to the large

size of (and inherent large space between) the C_{60} molecules, the alkali atoms are given enough volume to intercalate between the molecules of the crystal, keeping the same overall fcc shape (up to A_3C_{60}), shown in Fig. 3.5. Intercalation of alkali metals only leads to a slight increase of the lattice constant which increases based on the radius of the dopant atom, ranging from 14.24 Å in K_3C_{60} over 14.42 Å in Rb_3C_{60} to 14.80 Å in Cs_3C_{60}.[78, 79] This slight change in lattice spacing however has a dramatic effect on the electronic structure of the system.

Both K_3C_{60} and Rb_3C_{60} are metallic at room temperature and become superconducting at exceptionally high (high for a molecular system) temperatures T_c of 18 K and 28 K respectively. The trend of increasing T_c with increased lattice spacing however vanishes at the point of Cs_3C_{60}, which is not superconducting at ambient pressures.[78] Upon exposure to high pressures (reduction of lattice spacing) however, it becomes the highest temperature superconductor of the family at 38 K.[80] The need for elevated pressures renders the Cs compound obsolete for use in TFTs, but the K and Rb species attracted high interest due to their critical transition temperature. Both species have been successfully synthesized as thin films in metallic Au(111) and Ag(111) crystals by deposition of C_{60} and alkali metal doping, but neither have been realized on a (topological) insulator. Furthermore, only a few studies [81, 82] exist on the dependence of superconducting temperature as a function of layer thickness e.g. if monolayer films are actually superconducting and at which layer thickness it breaks down. Additionally, control over the precise stochiometry of the A_xC_{60} films is crucial, since slight under- or overdoping can result in the occurrence of (partial) A_1C_{60} and A_4C_{60}, A_6C_{60} phases, neither of which are metallic and su-

perconducting. These open questions establish A_3C_{60} thin films as an attractive field of study.

Chapter 4
Publications and Manuscripts

4.1 Photothermal bottom-up graphene nanoribbon growth kinetics

---

Yannic Falke, Boris V. Senkovskiy, Niels Ehlen, Lena Wysocki, Tomas Marangoni, Rebecca A. Durr, Alexander I. Chernov, Felix R. Fischer, and Alexander Grüneis

Photothermal Bottom-up Graphene Nanoribbon Growth Kinetics
Nano Lett. 2020, 20, 7, 4761–4767

Doi: `https://doi.org/10.1021/acs.nanolett.0c00317`

Bottom–up fabrication has evolved to become the preferred method for production of high quality graphene nanoribbons (GNRs). This method has to be adapted and tweaked for every new set of precursor molecule since the exact reaction kinetics for every GNR are different. To provide insight into the growth kinetics of any GNR, a novel method for time resolved study of GNR growth was developed based on laser induced heating and Raman spectroscopy measurements.

While common laboratory based lasers with power in the 100 mW range (on a sample) can substantially heat up a thin object, the bulk crystals which are commonly used in GNR synthesis dissipate the produced heat too quickly for the laser to heat it up substantially. Therefore, ultra-thin films of Au/MICA were prepared by means of sputtering and annealing

in ultra-high vacuum (UHV). The laser induced heating was determined for both the bulk Au crystals and the newly prepared Au/MICA thin film through measurements of the Stokes and Anti-Stokes lines of existing GNRs using Raman spectroscopy. Additionally, the temperature dependent shift of the G-like mode of 7-AGNR was determined in a temperature range of $\Delta T = 350\,\mathrm{K}$.

The growth kinetics of 7-AGNRs from precursor over the oligomer to the final nanoribbon with fusion to 14-AGNRs were studied using the novel method developed in this work. Here, short pulses of high intensity laser light were induced to thermally drive the reaction. The Raman response was traced after every heating step and evaluated as a function of heating time and heating power. This allowed for the extraction of temperature dependent reaction constants from precursor to GNR and 7-AGNR to fused 14-AGNR. The validity of this approach was further undermined by surface enhanced Raman scattering (SERS) which allowed for picking up the signal of precursor molecules, usually not visible in common Raman experiments. By using different, resonant lasers the fusion of the nanoribbons was proven.

This novel method was applied to further ribbons (chevron-type GNR and 13-AGNR) to prove its viability in different systems. Here, the extracted reaction constants vastly differed from the ones of the 7-AGNR system and were discussed in the context of substrate-molecule interaction.

Contributions to this publication:

- Main contribution to the publication come from Y. Falke and A. Grüneis with smaller contributions from the co-authors.
- Perform all measurements except atomic force microscopy.
- Evaluate all gathered data.
- Create all figures of main paper and supporting information except the sketch in Fig. 1.
- Design and program the technical aspect of the novel measurement process.

NANO LETTERS

pubs.acs.org/NanoLett

Letter

Photothermal Bottom-up Graphene Nanoribbon Growth Kinetics

Yannic Falke,* Boris V. Senkovskiy, Niels Ehlen, Lena Wysocki, Tomas Marangoni, Rebecca A. Durr, Alexander I. Chernov, Felix R. Fischer, and Alexander Grüneis*

Cite This: *Nano Lett.* 2020, 20, 4761−4767

Read Online

ACCESS | Metrics & More | Article Recommendations | Supporting Information

ABSTRACT: We present laser-induced photothermal synthesis of atomically precise graphene nanoribbons (GNRs). The kinetics of photothermal bottom-up GNR growth are unravelled by *in situ* Raman spectroscopy carried out in ultrahigh vacuum. We photothermally drive the reaction steps by short periods of laser irradiation and subsequently analyze the Raman spectra of the reactants in the irradiated area. Growth kinetics of chevron GNRs (CGNRs) and seven atoms wide armchair GNRs (7-AGNRs) is investigated. The reaction rate constants for polymerization, cyclodehydrogenation, and interribbon fusion are experimentally determined. We find that the limiting rate constants for CGNR growth are several hundred times smaller than for 7-AGNR growth and that interribbon fusion is an important elementary reaction occurring during 7-AGNR growth. Our work highlights that photothermal synthesis and *in situ* Raman spectroscopy are a powerful tandem for the investigation of on-surface reactions.

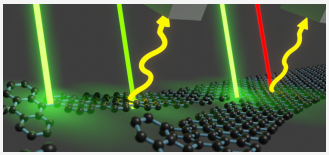

KEYWORDS: *graphene nanoribbons, photothermal, synthesis, Raman spectroscopy*

INTRODUCTION

The precise control of all steps of an on-surface chemical reaction is at the heart of chemical nanotechnology.[1] For example, all steps of the Ullmann-type reaction on a Cu surface have been induced and investigated by scanning tunneling microscopy (STM).[2] The necessary steps (dehalogenation of C_6H_5I, surface diffusion, and radical addition of two $C_6H_5^{\bullet}$) are induced by applying a voltage pulse to the STM tip and moving reactants on the surface.[2] Inspired by the on-surface reaction that fuses two molecules, supramolecular on-surface assembly has been developed.[3] One important class of precursor molecules can assemble into graphene nanoribbons (GNRs) with different width and edge termination.[4−6] The reaction steps of GNR synthesis consist of the dehalogenation of the precursor, radical diffusion across the surface, polymerization into a polymer chain, and finally cyclodehydrogenation. The precursor monomer of the seven atoms wide armchair GNR (7-AGNR) is the 10,10-dibromo-9,9-bianthracene (DBBA) molecule.[4] On the Au(111) substrate, the polymerization of DBBA occurs at ∼470 K and the cyclodehydrogenation of the resulting polymer chain occurs at ∼670 K.[4] It has been shown by STM that interribbon dehydrogenation (lateral fusion) of 7-AGNRs that are in proximity can occur.[7] Lateral fusion results in the formation of 14 carbon atoms wide segments (14-AGNRs) and, to a smaller extent, the formation of 21-AGNRs and so on.[7] Lateral fusion occurs on Au(111) at ∼770 K (see ref 7) but its rate constant is unknown. GNR growth has also been studied by X-ray photoelectron and X-ray absorption spectroscopies.[8] However, GNR growth kinetics has not yet been studied by time-dependent spectroscopy which is related to the difficulty in obtaining a reactant signal within a short integration time if the measurements are taken "live" during the reaction. If one were able to turn on and turn off the GNR growth anytime, a sufficient time could be taken to integrate the reactants' signal before proceeding with the reaction. Turning the reaction instantaneously on and off does not work if the reaction is driven conventionally by heating the substrate. There is a time delay when the temperature is changed because of the heat capacities of the substrate and the sample holder. Overcoming these limitations could lead to improved understanding of the reaction kinetics but requires the development of a new experimental technique.

Here, we photothermally drive bottom-up GNR growth inside an ultrahigh vacuum (UHV) chamber. To that end, we employ a laser beam that is focused onto a surface of a thin single crystalline Au(111) film on mica with precursor molecules deposited on top of Au(111). The experiments shown in this work constitute the first demonstration of photothermal control of an on-surface bottom-up reaction. A major result of our work is the determination of the reaction constants for the GNR growth and lateral fusion.[7,9] Photothermal growth is used for synthesis of 7-AGNRs, 13-AGNRs, and chevron type GNRs (CGNRs) and elegantly combines a high degree of control with simplicity and large reaction

Received: January 23, 2020
Revised: June 5, 2020
Published: June 8, 2020

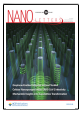

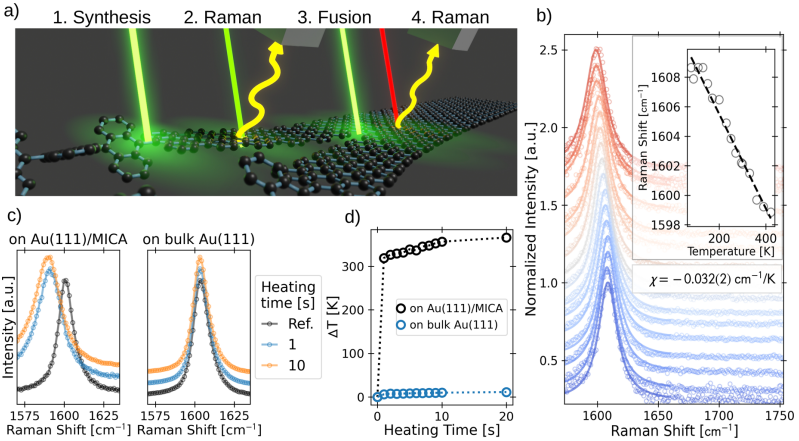

Figure 1. (a) Sketch of the formation and fusion of 7-AGNRs to 14-AGNRs using laser-induced photothermal synthesis. The hydrogen atoms are omitted for clarity, and the spot size of the laser is not to scale. Steps 1−4 indicate driving of the reaction by a high laser power and the investigation of the reaction products using a small laser power. Steps 1−4 are performed consecutively one after another on the same spot on the sample. (b) The temperature-dependent Raman G-like band spectra of 7-AGNRs on a Au(111) bulk crystal along with a fit (solid line) between 90−420 K. The colors blue (red) indicate low (high) temperatures. The sample temperature was controlled by lN2 cooling and conventional heating and measured by a thermocouple. Inset: the G-like band peak position as a function of temperature along with a linear fit of the slope χ. (c) UHV-Raman spectra of the G-like band of 7-AGNRs synthesized on Au(111)/mica and on a bulk Au(111) crystal under application of a λ = 532 nm laser with P = 130 mW. The spectrum in black is the reference spectrum (P = 1.3 mW). (d) Temperature change ΔT of the 200 nm Au(111)/mica and the bulk Au(111) substrates w.r.t. room temperature versus laser irradiation time.

volume. In the photothermal effect, heat is generated as a consequence of an optical de-excitation into phonons. By applying the laser-induced photothermal reaction inside a UHV Raman system, we identify the reaction product, its abundance, and the quality of the product via the position, intensity, and width of the Raman modes, respectively. GNRs have fingerprint Raman modes which allow easy identification. For example, the radial-breathing like mode (RBLM) has a distinct frequency defined by the GNR width.[10,11]

RESULTS AND DISCUSSION

Photothermal Nanoribbon Synthesis. Photothermal synthesis and characterization of the reaction products by Raman spectroscopy are performed *in situ* in a home-built UHV Raman system.[12−14] This UHV Raman system was already employed to investigate hydrogenated 7-AGNRs[15] and boron-doped GNRs.[16] Our starting substrate is a clean, ∼200 nm thick Au(111) film on mica whose surface is prepared by sputtering and annealing.[17] After the surface quality is confirmed by low-energy electron diffraction, one monolayer of precursor molecules is evaporated onto the surface from a Knudsen cell.

Local heating of the surface is achieved using a laser beam (λ = 532 nm, P = 130 mW, spotsize ∼4 μm). If the Au film is sufficiently thin, the laser beam causes instantaneous heating which is needed for GNR synthesis. The heating drives the chemical reactions leading to GNR growth and lateral fusion. The procedure is shown schematically in Figure 1a for the DBBA precursor. Cyclodehydrogenation and lateral fusion reactions are shown but the reaction steps that occur prior to these two reactions (dehalogenation, DBBA diffusion, and the formation of polymer chains) are also induced photothermally. Steps 1−4 in Figure 1a denote photothermal 7-AGNR synthesis with a high laser power (step 1), the Raman measurement with a lower laser power (step 2), the lateral fusion of 7-AGNRs by another exposure to the high-power laser (step 3), and the Raman spectroscopy of 14-AGNRs using a different laser energy and again a small laser power (step 4). Apart from substrate heating, laser irradiation could lead to (1) photochemical reactions, (2) molecule diffusion out of the laser spot, and (3) electronic substrate excitations. We discuss (1−3) in the Supporting Information (SI) and conclude that their effects are negligible. Let us now proceed to the determination of the GNR temperature in the laser spot. Our strategy is as follows: we first establish the linear relation between GNR phonon frequency and temperature by performing temperature-dependent Raman measurements using conventional heating and cooling. We then apply this relation to the phonon frequency shifts observed for GNRs heated by the laser to determine the temperature inside the laser spot. Figure 1b shows a series of G-like Raman spectra of 7-AGNRs on a bulk Au(111) crystal between T = 90 K and T = 420 K. The temperature was measured by a thermocouple placed in direct contact under the Au(111) crystal. Upon increasing temperature, the G-like peak position moves toward lower frequencies. The measured G-like band frequency ω depends linearly on temperature T as is shown in the inset to Figure 1b. Fitting the slope of ω versus T via $\Delta\omega = \Delta T\chi$, we obtain the temperature coefficient of the G-like band χ = −0.032(2) cm^{-1}/K which is in good agreement to the reported literature value of χ = −0.030 cm^{-1}/K (see ref 18). Using ω versus T, we estimate the T of 7-AGNRs inside the laser spot

https://dx.doi.org/10.1021/acs.nanolett.0c00317
Nano Lett. 2020, 20, 4761−4767

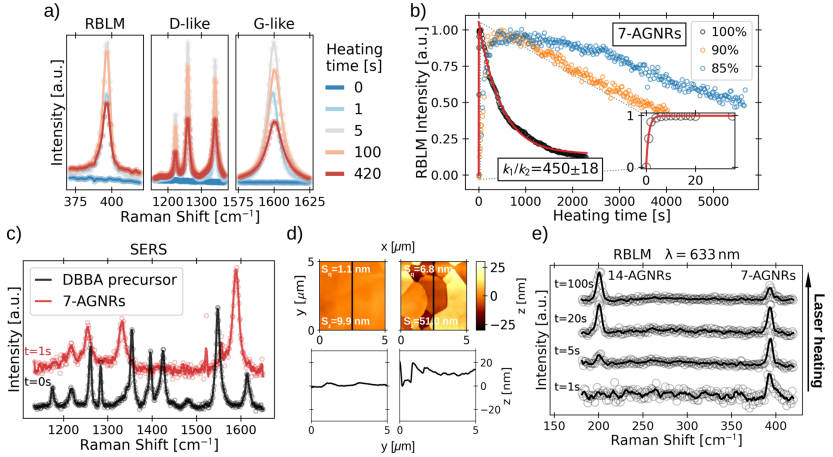

Figure 2. (a) Time-dependent UHV-Raman spectra of the RBLM, D-like and G-like modes during the 7-AGNR synthesis. Photothermal synthesis was performed using a laser (λ = 532 nm, P = 130 mW). (b) Time-dependent RBLM intensity (extracted by fitting Lorentzian functions) and two exponential fits to the data (red). The reaction rate constants for 7-AGNR growth and the conversion to 14-AGNRs are k_1 and k_2 (see text) and the value of k_2/k_1 obtained from the fit to the experimental data is indicated. Changing the laser power (100%, 90%, and 85% of P = 130 mW) results in different reaction rates. The inset is a zoom-in to the 100% curve and depicts the time-dependent RBLM intensity for short irradiation times. (c) DBBA precursor Raman spectrum (black) measured by surface-enhanced Raman spectroscopy (SERS) using a rough Au(111)/mica substrate, and 7-AGNR Raman modes (red) after 1 s of photothermal synthesis (130 mW laser). (d) Topography and surface roughness analysis by atomic force microscopy (AFM) of the Au(111)/mica used for SERS. The left and right panels depict AFM before and after sputtering, respectively. The lower panel shows cuts along the black lines indicated in the AFM topographs. The values of S_z and S_q (see text) before and after sputtering are indicated. (e) Raman spectra of 7-AGNRs during fusion to 14-AGNRs as a function of heating time. Raman spectra are obtained using λ = 633 nm excitation. The RBLM modes of 7-AGNRs and 14-AGNRs are indicated.

for a thin Au(111) film grown on mica and bulk Au(111). The laser power hitting the sample was set to 130 mW. A series of Raman spectra in the region of the G-like band of 7-AGNRs on both substrates is shown in Figure 1c. For a thin film of Au(111)/mica, we observe a rapid downshift of the phonon frequency of the G-like band of 7-AGNRs by $\Delta\omega$ = 10 cm^{-1} after exposure to the laser beam. The Raman spectrum of the G-like band recorded at 1.3 mW laser power (black curves in Figures 1c) for which we have negligible substrate heating serves as a reference spectrum. To cross-check our conclusions, we perform an identical experiment on 7-AGNRs synthesized on bulk Au(111) (Figure 1c) and find that the G-like band position is not affected by the laser intensity. We conclude that the Au(111)/mica film can be heated by the laser while the heat conductivity of the bulk Au(111) is too high to result in a temperature increase upon laser irradiation. Upon laser irradiation, the GNR temperature on Au(111)/mica rises instantaneously from room temperature (T = 295 K) by ΔT = 313 K, and then increases by another 60 K over the next 20 s yielding a final absolute T = 668 ± 25 K. We estimated the uncertainty in T based on the uncertainties in $\Delta\omega$ and χ (0.5 cm^{-1} and 0.002 cm^{-1}/K, respectively). The obtained temperatures are sufficient to induce all steps of GNR synthesis.[4] Using the laser to heat the sample results in a higher temperature gradient versus time compared to the use of a conventional heater (e.g. a filament). In the latter case, the large heat capacity of the single crystal substrate and sample holder takes more time to reach thermal equilibrium. Since the chemical reaction proceeds during the time to reach equilibrium, the reaction conditions are ill-defined. In the case of laser heating a small spot on the sample surface, there are no delays because of the negligible heat capacity of the volume heated by the laser spot. Therefore, the reaction can be turned on and off without a time lag.

Photothermal Synthesis of 7-AGNRs and Lateral Fusion to 14-AGNRs. We employ the precise on/off control of the substrate heating to study the 7-AGNRs growth kinetics. Precursor molecules on Au(111)/mica are exposed to a 130 mW laser beam for a defined time of laser annealing which is followed by Raman spectroscopy using a smaller laser power (see SI for optical absorption of Au and precursors). Figure 2a depicts Raman spectra collected after laser annealing (see SI for full set of time-dependent Raman spectra and comparison of photothermally and conventionally synthesized 7-AGNRs). The comparison of Raman spectra of photothermally and conventionally synthesized 7-AGNRs is shown in the SI. We conclude that the sample qualities are comparable based on Raman peak widths that are proportional to defect concentration.[19,20] At t = 0, there is only the flat background line in all Raman spectra in the investigated spectral range because the Raman response of DBBA in these conditions is too weak. Upon illumination by a 130 mW laser, a Raman signal appears after Δt = 1 s of irradiation indicating the conversion of DBBA to resonant 7-AGNRs. From the individual scans in Figure 2a, we observe that the Raman intensity saturates already after Δt = 5 s of irradiation. This

https://dx.doi.org/10.1021/acs.nanolett.0c00317
Nano Lett. 2020, 20, 4761−4767

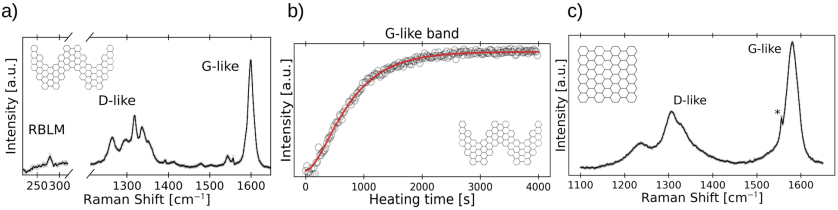

Figure 3. (a) Raman spectrum (λ = 532 nm) of photothermally synthesized (P = 130 mW, 2500 s) chevron-type GNRs (CGNRs) on Au(111)/mica. (b) Time-dependent G-like band Raman intensity of CGNRs as a function of laser irradiation time (P = 130 mW). The raw Raman data is shown in the SI. The red line denotes a fit of the reaction rate constants (see text) assuming a two-step reaction model. (c) Raman spectrum (λ = 532 nm) of photothermally synthesized 13-AGNRs on Au(111)/mica, (*) is due to O_2 present in the laser path.

observation can be explained by two mechanisms. One is the lateral fusion of 7-AGNRs to 14-AGNRs and wider AGNRs. The existence of 14-AGNRs will be deduced later from the observation of a new RBLM mode. The second mechanism relates to the different Raman cross sections of 7-AGNRs and 14-AGNRs, for example, the RBLM intensity of 14-AGNRs cannot be observed by 532 nm excitation (see ref 7 and the SI). Figure 2b shows the time-dependent Raman intensity of the 7-AGNR RBLM mode for laser irradiation by three different powers (100%, 90%, and 85% of 130 mW). For all three laser powers, the characteristic rise and fall of the RBLM intensity can be observed. For a higher laser power, the rise and fall of the Raman intensity proceed faster. The data in Figure 2b have been obtained using automated laser power control for synthesis and Raman measurements. We have used Δt = 15 s irradiation time for all data points at t > 20 s and a shorter irradiation time for data points t < 20 s (see inset to Figure 2b).

In the kinetic model for the GNR growth, we consider three consecutive elementary reactions. One is the formation of polymer chains from precursor molecules described by the reaction rate constant k_0 that effectively models dehalogenation, monomer diffusion, and the covalent bonding of monomers to a polymer chain. The next step is the conversion of polymer chains to 7-AGNRs which is described by k_1. Finally, we describe the lateral fusion of 7-AGNRs to 14-AGNRs by k_2. The inset of Figure 2b shows that, for short laser irradiation times, the 7-AGNR concentration is linearly rising in time. Thus, the growth is limited by either k_0 or by k_1. If the values of the rate constants k_0 and k_1 were close to each other, the time-dependent growth kinetics would be sigmoidal in shape.[21] To understand which of k_0 and k_1 is the limiting rate, we consider the reported temperatures[4] needed for polymerization (~470 K) and cyclodehydrogenation (~670 K). Thus, polymerization is effective already at lower temperatures. If we photothermally drive the reaction, we almost instantaneously reach 670 K. Since the rate constants depend exponentially on temperature, we believe that the reaction steps leading to the formation of a polymer chain proceed faster than the cyclodehydrogenation, that is $k_0 \gg k_1$. We therefore consider only the rate limiting k_1 to describe the reaction kinetics. We will show later that this is not the case for the precursor molecule that is used to synthesize CGNRs where the values of k_0 and k_1 are close to each other and both reactions must be considered. This results in a sigmoidal shape of the time-dependent GNR Raman intensity.

The Raman intensity of the 7-AGNR RBLM mode is proportional to the 7-AGNR abundance which is given by the amount of polymer chains converted to 7-AGNRs (rate constant k_1) minus the 7-AGNRs converted to 14-AGNRs (rate constant k_2). Figure 2b reveals that $k_1 \gg k_2$ which allows for treating the rise and the fall separately. The rise and fall of the Raman intensity $I(t)$ are proportional to 7-AGNR abundance and can be modeled by first order kinetics[21] as $I \propto 1 - \exp(-k_1 t)$ and $I \propto \exp(-k_2 t)$, respectively. The fits of the curve in Figure 2b, which are taken with 100% laser power, yield $k_1 = (9.0 \pm 0.04) \times 10^{-1}$ s^{-1} and $k_2 = (2.07 \pm 0.04) \times 10^{-3}$ s^{-1}. That is, the total conversion from 7-AGNRs to wider GNRs is proceeding $k_2/k_1 = 450 \pm 18$ times slower than the synthesis of 7-AGNRs. This large difference in reaction rate constants implies that it is possible to perform synthesis of a 7-AGNR film with a certain concentration of fused GNRs by choice of the laser irradiation time. Laser-based photothermal synthesis with precise *in situ* control by UHV Raman thus allows for improved control of the chemical reactions compared to conventional heating of the substrate.[7]

To corroborate the fast conversion of DBBA into 7-AGNRs, we perform laser heating of DBBA on a rough Au(111)/mica substrate which is prepared using Ar^+ ion bombardment (1.1 keV, 100 min, incidence angle: 30° w.r.t. the surface normal). The increased surface roughness makes it possible to perform surface-enhanced Raman spectroscopy (SERS).[22] The Raman signal of DBBA on rough Au(111)/mica confirms the presence and the conversion of DBBA upon laser heating (see Figure 2c). Already at t = 1 s, the precursor-related Raman modes vanish and the 7-AGNR Raman spectrum appears. This is consistent with the fast reaction rate constant obtained from the observation of Raman modes of 7-AGNRs. Figure 2d depicts an analysis of the surface topographies of the pristine and rough Au(111)/mica by atomic force microscopy (AFM). The surface roughness is characterized by S_z = 51 nm and S_q = 6.8 nm defined as the maximum height difference and the standard deviation of heights, respectively. These values are comparable to literature[23] and also induce SERS in rhodamine-6G standard probe molecules (SI).

The 14-AGNR RBLM peak was observed using λ = 633 nm excitation but could not be observed by the λ = 532 nm excitation. Photothermal synthesis by the 532 nm laser and Raman measurements with the 633 nm laser requires a change of the laser energy. To ensure that the same spot is measured with both lasers, we scanned the laser spot (130 mW, 532 nm) across 20 × 20 μm^2 area to convert this region to 14-AGNRs. Then we changed to λ = 633 nm and focused inside the square.

https://dx.doi.org/10.1021/acs.nanolett.0c00317
Nano Lett. 2020, 20, 4761−4767

Figure 2e depicts the Raman spectra obtained at different times during the fusion. At $t = 0$, there is one peak in the RBLM spectrum at 400 cm^{-1} which corresponds to 7-AGNRs. At $t > 0$, we start to observe another peak at about 200 cm^{-1} which we assign to the 14-AGNR RBLM mode. This observation corroborates that 7-AGNRs are indeed partially converted to 14-AGNRs and explains the loss of 7-AGNR Raman intensity reported in Figure 2b.

Photothermal Synthesis of Chevron Type GNRs and 13-AGNRs. We investigate photothermal synthesis of chevron GNRs (CGNRS) (see, e.g., refs 4 and 24−29) and 13-AGNRs (see, e.g., refs 30 and 31). The CGNRs use 6,11-dibromo-1,2,3,4-tetraphenyltriphenylene as precursors and Figure 3a shows the Raman spectrum of CGNRs synthesized on Au(111)/mica by laser heating. Sharp Raman modes confirm the high structural quality of the material. The time-dependent Raman intensity is plotted in Figure 3b. The laser irradiation time Δt before each measurement was chosen $\Delta t = 20$ s. Raw data Raman scans at different irradiation times are shown in the SI. The time-dependent Raman signal in Figure 3b reveals strong differences from the kinetics observed for 7-AGNRs. The Raman intensity versus time has a sigmoidal shape, that is, close to $t = 0$ the Raman signal does not rise linearly as we have observed in the 7-AGNR case but quadratically in time. We attribute this to the fact that, in the case of CGNRs, the growth is limited by both the formation of polymer chains (k_0) and the cyclodehydrogenation of polymer chains (k_1). This results in relatively longer synthesis times to reach a saturation of the CGNR Raman intensity (at $t = 2500$ s) which is a factor ∼300 longer than observed for 7-AGNRs. In the case of 7-AGNRs, the Raman intensity is saturated already at $t = 10$ s. We do not observe evidence for lateral fusion of CGNRs, that is, $k_2 \sim 0$ within the time spans of our experiments. That is, the Raman intensity does not decrease for long illumination times. We believe that higher temperatures are needed to laterally fuse CGNRs in agreement with the fact that no lateral fusion of CGNRs has been reported from STM measurements.

The time-dependent Raman intensity of CGNRs during synthesis is modeled by the rate equation that describes two consecutive reactions[21] as $I \propto \left\{1 + \frac{k_0 e^{-k_1 t} - k_1 e^{-k_0 t}}{k_1 - k_0}\right\}$. For CGNRs we find $k_0 = 0.001$ s^{-1} and $k_1 = 0.004$ s^{-1}. The values of k_0 and k_1 are close to each other at variance to the 7-AGNR growth kinetics where we had $k_0 \gg k_1$. The fact that k_0 for CGNR growth is smaller than k_0 for 7-AGNR growth is related to the larger size of the precursor molecule in the case of CGNR growth. The larger precursor molecule has a lower diffusion constant compared to DBBA. The rate constant k_1 that describes cyclodehydrogenation is larger in the case of 7-AGNR growth than for CGNR growth. We speculate that this is a result of the larger energy needed to convert a polymer chain into a CGNR relative to the conversion of the corresponding polymer chain into a 7-AGNR. These observations are consistent with the larger temperatures needed for CGNR growth.[4]

We summarize the fit results for monomer polymerization (k_0), conversion of a polymer chain to a GNR (k_1), and the lateral fusion (k_2) for 7-AGNRs and CGNRs in Table 1. Finally, we have performed growth of 13-AGNRs[31,32] on Au(111)/mica by photothermal synthesis employing 2,2′-di((1,1′-biphenyl)-2-yl)-10,10′-dibromo-9,9′-bianthracene as a precursor molecule. The Raman spectrum of photothermally synthesized 13-AGNRs (130 mW) is shown in Figure 3c and is in good agreement to the Raman spectrum of conventionally synthesized 13-AGNRs.[33,34]

Table 1. Summary of the Reaction Rate Constants[a]

reaction constant	k_0	k_1	k_2
7-AGNRs	$k_0 \gg k_1$	0.9	0.002
chevron	0.001	0.004	0

[a]For monomer polymerization (k_0), conversion of a polymer chain to a GNR (k_1) and the reaction rate constant for lateral fusion (k_2) for 7-AGNRs and chevron type GNRs. All rate constants are in units s^{-1}.

CONCLUSION AND OUTLOOK

We have introduced *in situ* laser-controlled photothermal bottom-up synthesis of GNRs. Precursors on a 200 nm Au(111) film can be locally heated up to temperatures exceeding 660 K. If higher temperatures are needed to drive a specific reaction, they may be achieved by reducing the Au(111) thickness or by increasing the power. By combining laser heating with UHV Raman spectroscopy, the reaction intermediates could be studied and the rate constants determined. Laser irradiation enables precise control of the 7-AGNR/14-AGNR fraction which is a critical factor for tuning the electrical conductivity of a GNR film. We expect that laser-induced synthesis can be applied to many GNR types, for example, 5-AGNRs for which lateral fusing is also possible.[35] Using the methods shown here, one could apply photothermal heating to pattern a circuit by the laser beam. Conducting paths of small band gap 14-AGNRs could be written into a matrix consisting of 7-AGNRs on Au(111)/mica. This film could then be transferred from Au(111) onto a Si wafer.[15] That 14-AGNR path could then serve as the active element in a field effect transistor.

ASSOCIATED CONTENT

Supporting Information

The Supporting Information is available free of charge at https://pubs.acs.org/doi/10.1021/acs.nanolett.0c00317.

Discussion of optical absorption of Au and of DBBA. Comparison of Raman spectra of conventionally and photothermally synthesized 7-AGNRs. Individual time-dependent Raman spectra during synthesis of 7-AGNRs and CGNRs. SERS of rhodamine-6G probe molecules deposited onto rough/flat Au(111)/mica substrates. Discussion of laser-driven processes that can affect the reaction. Discussion of 7-AGNR/14-AGNR Raman intensity cross sections (PDF)

AUTHOR INFORMATION

Corresponding Authors

Yannic Falke − *II. Physikalisches Institut, Universität zu Köln, 50937 Köln, Germany*; Email: falke@ph2.uni-koeln.de

Alexander Grüneis − *II. Physikalisches Institut, Universität zu Köln, 50937 Köln, Germany*; orcid.org/0000-0003-2448-6060; Email: grueneis@ph2.uni-koeln.de

Authors

Boris V. Senkovskiy − *II. Physikalisches Institut, Universität zu Köln, 50937 Köln, Germany*; orcid.org/0000-0003-1443-6780

Niels Ehlen − *II. Physikalisches Institut, Universität zu Köln, 50937 Köln, Germany*; orcid.org/0000-0002-8581-8359

https://dx.doi.org/10.1021/acs.nanolett.0c00317
Nano Lett. 2020, 20, 4761−4767

Lena Wysocki − *II. Physikalisches Institut, Universität zu Köln, 50937 Köln, Germany*
Tomas Marangoni − *Department of Chemistry, University of California, Berkeley, California 94720, United States*
Rebecca A. Durr − *Department of Chemistry, University of California, Berkeley, California 94720, United States*
Alexander I. Chernov − *II. Physikalisches Institut, Universität zu Köln, 50937 Köln, Germany; Center for Photonics and 2D Materials, Moscow Institute of Physics and Technology (National Research University), 141700 Dolgoprudny, Russia; Russian Quantum Center, 121205 Moscow, Russia*
Felix R. Fischer − *Department of Chemistry, University of California, Berkeley, California 94720, United States; Materials Sciences Division, Lawrence Berkeley National Laboratory, Berkeley, California 94720, United States; Kavli Energy NanoSciences Institute, University of California Berkeley and the Lawrence Berkeley National Laboratory, Berkeley, California 94720, United States;* orcid.org/0000-0003-4723-3111

Complete contact information is available at: https://pubs.acs.org/10.1021/acs.nanolett.0c00317

Notes

The authors declare no competing financial interest.

■ ACKNOWLEDGMENTS

Y.F., B.S., N.E., and A.G. acknowledge funding from DFG project GR 3708/4-1 and an ERC Consolidator Grant "SUPER-2D". A.C. acknowledges an Alexander von Humboldt fellowship. F.R.F. acknowledges support by the Office of Naval Research under Project N00014-19-1-2503.

■ REFERENCES

(1) de Oteyza, D. G.; Rogero, C. E. On-Surface Synthesis II. *Proceedings of the International Workshop On-Surface Synthesis*; Springer: San Sebastian, 2016.
(2) Hla, S.-W.; Bartels, L.; Meyer, G.; Rieder, K.-H. Inducing All Steps of a Chemical Reaction with the Scanning Tunneling Microscope Tip: Towards Single Molecule Engineering. *Phys. Rev. Lett.* **2000**, *85*, 2777−2780.
(3) Grill, L.; Dyer, M.; Lafferentz, L.; Persson, M.; Peters, M. V.; Hecht, S. Nano-architectures by covalent assembly of molecular building blocks. *Nat. Nanotechnol.* **2007**, *2*, 687−691.
(4) Cai, J.; Ruffieux, P.; Jaafar, R.; Bieri, M.; Braun, T.; Blankenburg, S.; Muoth, M.; Seitsonen, A. P.; Saleh, M.; Feng, X.; Müllen, K.; Fasel, R. Atomically Precise Bottom-up Fabrication of Graphene Nanoribbons. *Nature* **2010**, *466*, 470−473.
(5) Koch, M.; Ample, F.; Joachim, C.; Grill, L. Voltage-dependent conductance of a single graphene nanoribbon. *Nat. Nanotechnol.* **2012**, *7*, 713−717.
(6) Talirz, L.; Ruffieux, P.; Fasel, R. On-Surface Synthesis of Atomically Precise Graphene Nanoribbons. *Adv. Mater.* **2016**, *28*, 6222−6231.
(7) Ma, C.; Liang, L.; Xiao, Z.; Puretzky, A. A.; Hong, K.; Lu, W.; Meunier, V.; Bernholc, J.; Li, A.-P. Seamless Staircase Electrical Contact to Semiconducting Graphene Nanoribbons. *Nano Lett.* **2017**, *17*, 6241−6247.
(8) Simonov, K. A.; Vinogradov, N. A.; Vinogradov, A. S.; Generalov, A. V.; Zagrebina, E. M.; Mårtensson, N.; Cafolla, A. A.; Carpy, T.; Cunniffe, J. P.; Preobrajenski, A. B. Effect of Substrate Chemistry on the Bottom-Up Fabrication of Graphene Nanoribbons: Combined Core-Level Spectroscopy and STM Study. *J. Phys. Chem. C* **2014**, *118*, 12532−12540.
(9) Wang, S.; Kharche, N.; Costa Girão, E.; Feng, X.; Müllen, K.; Meunier, V.; Fasel, R.; Ruffieux, P. Quantum Dots in Graphene Nanoribbons. *Nano Lett.* **2017**, *17*, 4277−4283.
(10) Zhou, J.; Dong, J. Vibrational property and Raman spectrum of carbon nanoribbon. *Appl. Phys. Lett.* **2007**, *91*, 173108.
(11) Vandescuren, M.; Hermet, P.; Meunier, V.; Henrard, L.; Lambin, P. Theoretical study of the vibrational edge modes in graphene nanoribbons. *Phys. Rev. B: Condens. Matter Mater. Phys.* **2008**, *78*, 195401.
(12) Senkovskiy, B. V.; et al. Semiconductor-to-Metal Transition and Quasiparticle Renormalization in Doped Graphene Nanoribbons. *Adv. Electron. Mater.* **2017**, 3, 1600490.
(13) Grüneis, A.; Senkovskiy, B. V.; Fedorov, A. V.; Hell, M.; Michel, S. In *Encyclopedia of Interfacial Chemistry*; Wandelt, K., Ed.; Elsevier: Oxford, 2018; pp 367−374.
(14) Hell, M. G.; Falke, Y.; Bliesener, A.; Ehlen, N.; Senkovskiy, B. V.; Szkopek, T.; Grüneis, A. Combined Ultra High Vacuum Raman and Electronic Transport Characterization of Large-Area Graphene on SiO2. *Phys. Status Solidi B* **2018**, *255*, 1800456.
(15) Senkovskiy, B. V.; et al. Making Graphene Nanoribbons Photoluminescent. *Nano Lett.* **2017**, *17*, 4029−4037.
(16) Senkovskiy, B. V.; et al. Boron-Doped Graphene Nanoribbons: Electronic Structure and Raman Fingerprint. *ACS Nano* **2018**, *12*, 7571−7582.
(17) Hell, M. G.; Senkovskiy, B. V.; Fedorov, A. V.; Nefedov, A.; Wöll, C.; Grüneis, A. Facile preparation of Au(111)/mica substrates for high-quality graphene nanoribbon synthesis. *Phys. Status Solidi B* **2016**, *253*, 2362−2365.
(18) Late, D. J.; Maitra, U.; Panchakarla, L. S.; Waghmare, U. V.; Rao, C. N. R. Temperature effects on the Raman spectra of graphenes: dependence on the number of layers and doping. *J. Phys.: Condens. Matter* **2011**, *23*, 055303.
(19) Martins Ferreira, E. H.; Moutinho, M. V. O.; Stavale, F.; Lucchese, M. M.; Capaz, R. B.; Achete, C. A.; Jorio, A. Evolution of the Raman spectra from single-, few-, and many-layer graphene with increasing disorder. *Phys. Rev. B: Condens. Matter Mater. Phys.* **2010**, *82*, 125429.
(20) Cançado, L. G.; Jorio, A.; Ferreira, E. H. M.; Stavale, F.; Achete, C. A.; Capaz, R. B.; Moutinho, M. V. O.; Lombardo, A.; Kulmala, T. S.; Ferrari, A. C. Quantifying Defects in Graphene via Raman Spectroscopy at Different Excitation Energies. *Nano Lett.* **2011**, *11*, 3190−3196.
(21) Atkins, P.; de Paula, J. *Physical Chemistry*; Oxford University Press: Oxford, 2014.
(22) Maya, L.; Vallet, C. E.; Lee, Y. H. Sputtered gold films for surface-enhanced Raman scattering. *J. Vac. Sci. Technol., A* **1997**, *15*, 238−242.
(23) Gailly, P.; Petermann, C.; Tihon, P.; Fleury-Frenette, K. Ripple topography and roughness evolution on surface of polycrystalline gold and silver thin films under low energy Ar-ion beam sputtering. *Appl. Surf. Sci.* **2012**, *258*, 7717−7725.
(24) Linden, S.; Zhong, D.; Timmer, A.; Aghdassi, N.; Franke, J. H.; Zhang, H.; Feng, X.; Müllen, K.; Fuchs, H.; Chi, L.; Zacharias, H. Electronic Structure of Spatially Aligned Graphene Nanoribbons on Au(788). *Phys. Rev. Lett.* **2012**, *108*, 216801.
(25) Teeter, J. D.; Costa, P. S.; Mehdi Pour, M.; Miller, D. P.; Zurek, E.; Enders, A.; Sinitskii, A. Epitaxial growth of aligned atomically precise chevron graphene nanoribbons on Cu(111). *Chem. Commun.* **2017**, *53*, 8463−8466.
(26) Denk, R.; et al. Probing optical excitations in chevron-like armchair graphene nanoribbons. *Nanoscale* **2017**, *9*, 18326−18333.
(27) Chen, Z.; et al. Synthesis of Graphene Nanoribbons by Ambient-Pressure Chemical Vapor Deposition and Device Integration. *J. Am. Chem. Soc.* **2016**, *138*, 15488−15496.
(28) Bronner, C.; Marangoni, T.; Rizzo, D. J.; Durr, R. A.; Jørgensen, J. H.; Fischer, F. R.; Crommie, M. F. Iodine versus Bromine Functionalization for Bottom-Up Graphene Nanoribbon Growth: Role of Diffusion. *J. Phys. Chem. C* **2017**, *121*, 18490−18495.
(29) Bronner, C.; Durr, R. A.; Rizzo, D. J.; Lee, Y.-L.; Marangoni, T.; Kalayjian, A. M.; Rodriguez, H.; Zhao, W.; Louie, S. G.; Fischer, F. R.; Crommie, M. F. Hierarchical On-Surface Synthesis of Graphene Nanoribbon Heterojunctions. *ACS Nano* **2018**, *12*, 2193−2200.

(30) Chen, Y.-C.; Cao, T.; Chen, C.; Pedramrazi, Z.; Haberer, D.; de Oteyza, D. G.; Fischer, F. R.; Louie, S. G.; Crommie, M. F. Molecular bandgap engineering of bottom-up synthesized graphene nanoribbon heterojunctions. *Nat. Nanotechnol.* **2015**, *10*, 156−160.
(31) Chen, Y.-C.; de Oteyza, D. G.; Pedramrazi, Z.; Chen, C.; Fischer, F. R.; Crommie, M. F. Tuning the Band Gap of Graphene Nanoribbons Synthesized from Molecular Precursors. *ACS Nano* **2013**, *7*, 6123−6128.
(32) Llinas, J. P.; Fairbrother, A.; Borin Barin, G.; Shi, W.; Lee, K.; Wu, S.; Yong Choi, B.; Braganza, R.; Lear, J.; Kau, N.; Choi, W.; Chen, C.; Pedramrazi, Z.; Dumslaff, T.; Narita, A.; Feng, X.; Mullen, K.; Fischer, F.; Zettl, A.; Ruffieux, P.; Yablonovitch, E.; Crommie, M.; Fasel, R.; Bokor, J.; et al. Short-channel field-effect transistors with 9-atom and 13-atom wide graphene nanoribbons. *Nat. Commun.* **2017**, *8*, 633.
(33) Vo, T. H.; Shekhirev, M.; Lipatov, A.; Korlacki, R. A.; Sinitskii, A. Bulk properties of solution-synthesized chevron-like graphene nanoribbons. *Faraday Discuss.* **2014**, *173*, 105−113.
(34) Chen, Z.; et al. Synthesis of Graphene Nanoribbons by Ambient-Pressure Chemical Vapor Deposition and Device Integration. *J. Am. Chem. Soc.* **2016**, *138*, 15488−15496.
(35) Chen, Z.; Wang, H. I.; Bilbao, N.; Teyssandier, J.; Prechtl, T.; Cavani, N.; Tries, A.; Biagi, R.; De Renzi, V.; Feng, X.; Kläui, M.; De Feyter, S.; Bonn, M.; Narita, A.; Müllen, K. Lateral Fusion of Chemical Vapor Deposited N = 5 Armchair Graphene Nanoribbons. *J. Am. Chem. Soc.* **2017**, *139*, 9483−9486.

https://dx.doi.org/10.1021/acs.nanolett.0c00317
Nano Lett. 2020, 20, 4761−4767

Supporting information for: Photothermal bottom-up graphene nanoribbon growth kinetics

Yannic Falke,[*,†] Boris V. Senkovskiy,[†] Niels Ehlen,[†] Lena Wysocki,[†] Tomas Marangoni,[‡] Rebecca A. Durr,[‡] Alexander I. Chernov,[†,¶,§] Felix R. Fischer,[‡,∥,⊥] and Alexander Grüneis[*,†]

†*II. Physikalisches Institut, Universität zu Köln, Zülpicher Strasse 77, 50937 Köln, Germany*

‡*Department of Chemistry, University of California, Berkeley, CA 94720, U.S.A.*

¶*Photonics and 2D Materials, Moscow Institute of Physics and Technology (National Research University), 141700, Dolgoprudny, Russia*

§*Russian Quantum Center, Skolkovo innovation city, 121205, Moscow, Russia*

∥*Materials Sciences Division, Lawrence Berkeley National Laboratory, Berkeley, CA 94720, U.S.A.*

⊥*Kavli Energy NanoSciences Institute at the University of California Berkeley and the Lawrence Berkeley National Laboratory, Berkeley, California 94720, U.S.A.*

E-mail: falke@ph2.uni-koeln.de; grueneis@ph2.uni-koeln.de

Optical absorption of Au and of DBBA

The optical properties of Au suggest that the reflectance increases strongly in the wavelength range between 500 nm and 600 nm with almost 100% reflection at wavelengths larger than ∼600 nm.[1,2] In our experiment, we use a 532 nm laser for supplying heat to the chemical re-

actions. We hence expect that the Au(111) substrate partially absorbs laser light that causes the photothermal effect. Regarding the optical properties of DBBA, there is no absorption at wavelengths higher than $\sim$ 400 nm.[3] This can be understood since the basic building block of DBBA is anthracene which does not significantly absorb light at wavelengths greater than $\sim$400 nm (see ref. 4). During the formation of GNRs, polymer chains form which may also absorb the laser light and contribute to heating.

Additional Raman spectra

In Figure S1 we show a Raman spectrum of photothermally synthesized 7-AGNRs compared to conventionally synthesized 7-AGNRs over a larger spectral range than in the manuscript. Figure S2 depicts the raw data of the time-dependent Raman spectra taken during 7-AGNR synthesis (c.f. Figure 2a,b of the manuscript). Figure S3 depicts the raw data of the time-dependent Raman spectra taken during chevron type GNR (CGNR) synthesis (c.f. Figure 3a,b of the manuscript). Note, the oxygen peak is from the path of the laser through air.

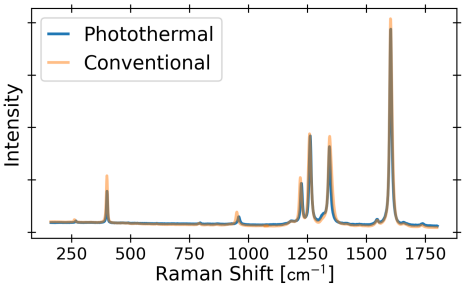

Figure S1: Raman spectra of conventionally and photothermally synthesized 7-AGNRs. Synthesis parameters: $P = 130$ mW, $\lambda = 532$ nm and $t = 20$ s.

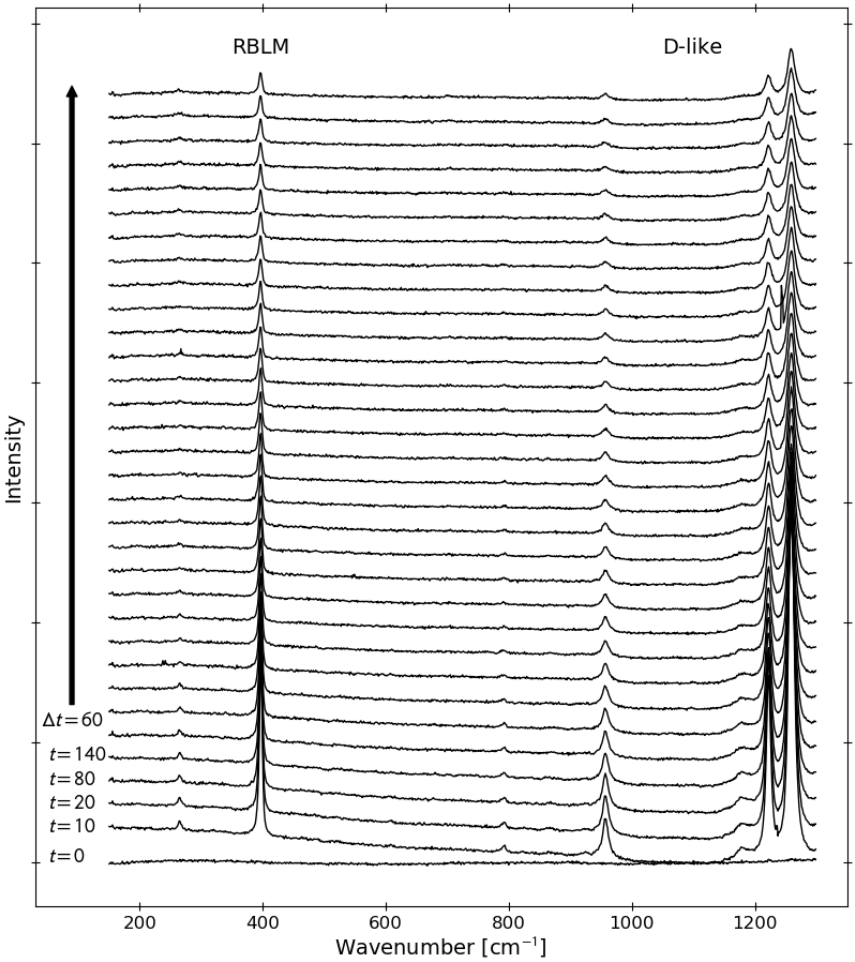

Figure S2: Time-dependent Raman spectra taken during the photothermal synthesis of 7-AGNRs. The time step in between the individual spectra was equal to $\Delta t = 10$ s for the first two scans and $\Delta t = 60$ s for scans thereafter. Measurement parameters: $P = 1.3$ mW, $\lambda = 532$ nm.

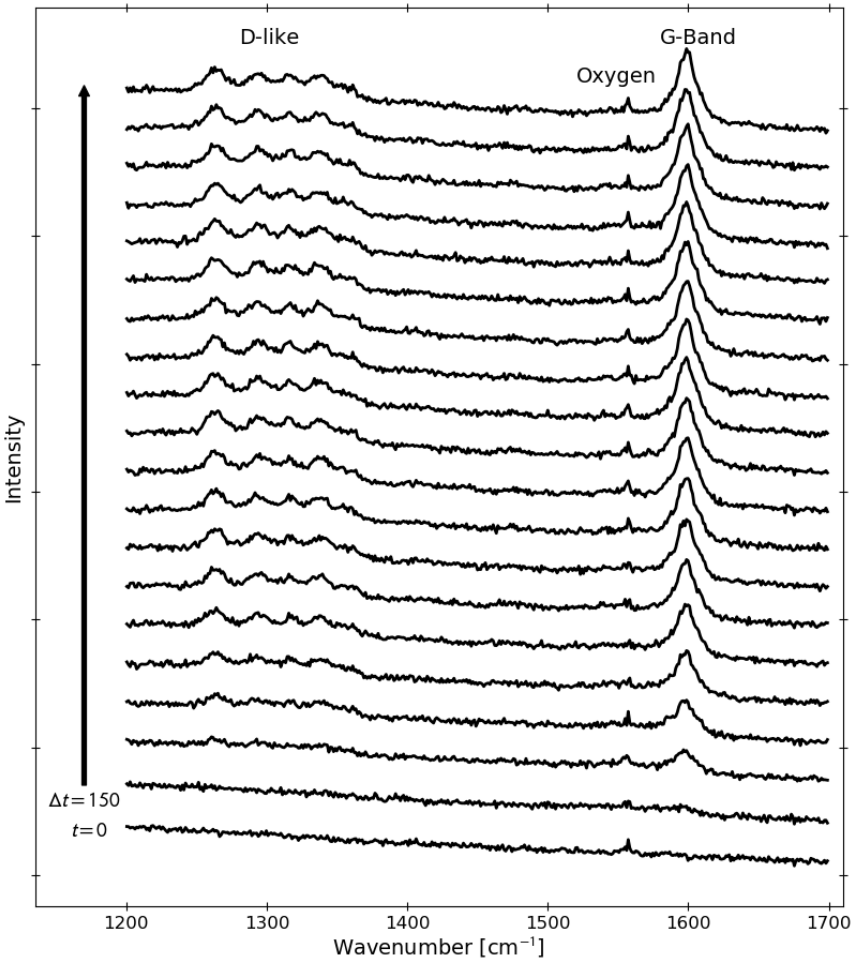

Figure S3: Time-dependent Raman spectra taken during the photothermal synthesis of CGNRs. The time step in between the individual spectra was equal to $\Delta t = 150$ s. Measurement parameters: $P = 1.3$ mW, $\lambda = 532$ nm. The oxygen peak at 1550 cm^{-1} comes from oxygen in the laser path.

Surface enhanced Raman spectra of rhodamine-6G probe molecules

Figure S4 shows Raman spectra of rhodamine-6G molecules on a rough Au(111)/mica substrate and on a flat Au(111)/mica substrate. The rough substrate has been prepared by Ar^+ ion sputtering sputtering. Identical amounts of rhodamine-6G solution in ethanol (10^{-6} molar concentration) were drop coated on both substrates.

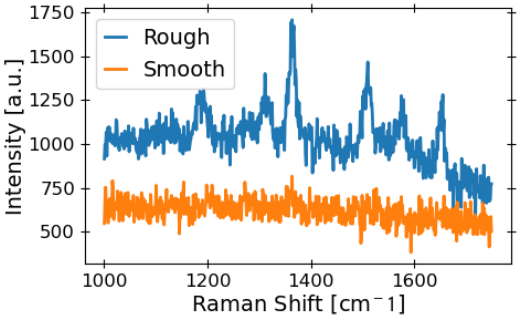

Figure S4: Demonstration of surface enhanced Raman scattering for rhodamine-6G deposited on rough Au(111)/mica (blue line). An identical amount of rhodamine-6G on a flat Au(111)/mica substrate shows no Raman signal (orange line). Measurement parameters: 0.5 mW, $\lambda = 532$ nm. See main text for sputtering parameters used to roughen the surface.

Discussion of laser-driven processes that can affect the reaction

Apart from substrate heating, the laser irradiation could lead to the following three processes: 1) photo-chemical reactions, 2) molecule diffusion out of the laser spot and 3) interaction of precursor molecules with electronic substrate excitations. Regarding 1), the precursor molecules cannot be excited by the $\lambda = 532$ nm that we have used for photothermal heat-

ing.[3]. This can be understood because the basic building block of DBBA is an anthracene unit which has a band gap in the UV range.[4] Regarding 2), if the precursor molecule diffusion length ℓ is larger than the heated spot, the precursor molecules can experience inhomogeneous reaction conditions. A typical diffusion length ℓ of a molecule on a surface can be estimated via a random walk model as a function of time t and temperature dependent diffusion coefficient $D(T) = D_0 \exp(-E_a/kT)$ as $\ell = \sqrt{2nD(T)t}$.[5,6] Here, D_0 is the prefactor, E_a is the energy barrier for diffusion, and $n = 2$ is the number of dimensions. Unfortunately, there are no experimental values of D_0 and E_a of DBBA molecules on Au(111) available. Let us therefore estimate ℓ using reasonable values of D_0 and E_a that describe the surface diffusion of similar sized organic molecules. Using $D_0 = 10^{-8}$ cm^2/s and $E_a = 150$ meV (that describe PTCDA diffusion on Ag(100)[7]), $t = 1$ s and $T = 670$ K, we obtain $\ell = 460$ nm. The obtained ℓ is well below the diameter of the laser spot ($\sim$4 μm). Moreover, for sufficiently large DBBA coverage, DBBA diffusion will be limited by the polymerization of DBBA molecules on the surface. Regarding 3), electronic excitations of the substrate can drive lateral diffusion of adsorbate molecules which has been studied e.g. for CO on Cu(110).[8] In this experiment, the sample was exposed to 200 fs pulses of visible light with an energy of 30 J/m^2 per pulse, inducing lateral motion of the CO adsorbate. Such a laser pulse increases the temperature of the electronic system of the substrate to about 3000 K. The hot substrate electrons can then couple to the translational degrees of freedom of the CO molecule (the cross section of this process is about 10^{-6}) and illumination by intense laser pulses causes lateral CO diffusion. The power during the laser pulse is about 100 W which is about 3 orders of magnitude higher than the power of the continuous laser beam in the present work. We therefore conclude that coupling to electronic excitations of the substrate is negligible in the present case.

Discussion of 7-AGNR/14-AGNR Raman intensity cross sections

Let us now discuss the laser energy dependence of the Raman intensities of 7-AGNRs and 14-AGNRs. One might argue that observation of a Raman signal of monolayer 7-AGNRs with the 633 nm (1.92 eV) excitation is surprising because the excitation energy is below the energy band gap of 7-AGNRs (2.1 eV on Au(788) according to ref. 9). For 14-AGNRs, the band gap on Au is very small (∼0.2 eV) and yet, the RBLM mode of 14-AGNRs cannot be observed by the 532 nm laser. This observation is consistent with literature reports.[10] Thus, the two questions that arise are : 1) why the RBLM mode of 7-AGNRs can be observed by the 633 nm laser and 2) why do the 14-AGNRs have no RBLM intensity if excited by the 532 nm laser. Regarding question 1), an inspection of the energy dependent optical absorption (Fig. 1 of ref. 9) suggests that the absorption peak is rather broad (250 meV) and hence the resonance Raman cross section is sufficiently large to obtain a signal at 1.92 eV. Regarding question 2), it is not unusual that the resonance Raman profiles of different phonon modes have a unique dependence on the excitation energy. For 9-AGNRs, it has been found that the RBLM Raman intensity can only be observed by the 785 nm laser (1.58 eV) which is close to the 9-AGNR gap of about 1 eV. The RBLM mode of 9-AGNRs was suppressed when excited with a green or blue laser (see the supporting information of refs. 11,12). This behaviour was attributed to the possibility to coherently excite the RBLM mode if the excitation energy is close to the gap.[13] We speculate that a similar mechanism (coherent Raman scattering) could be at work in the present experiment, too.

References

(1) Loebich, O. The optical properties of gold. *Gold Bulletin* **1972**, *5*, 2–10.

(2) Yakubovsky, D. I.; Arsenin, A. V.; Stebunov, Y. V.; Fedyanin, D. Y.; Volkov, V. S. Optical constants and structural properties of thin gold films. *Opt. Express* **2017**, *25*, 25574–25587.

(3) Natarajan, P.; Schmittel, M. Photoluminescence, Redox Properties, and Electrogenerated Chemiluminescence of Twisted 9,9'-Bianthryls. *J. Org. Chem.* **2013**, *78*, 10383–10394.

(4) Ferguson, J.; Reeves, L. W.; Schneider, W. G. Vapor absorption spectra and oscillator strengths of naphtalene, anthracene and pyrene. *Canadian Journal of Chemistry* **1957**, *35*, 1117–1136.

(5) Barth, J. V. Transport of adsorbates at metal surfaces: from thermal migration to hot precursors. *Surface Science Reports* **2000**, *40*, 75–149.

(6) Gomer, R. Diffusion of adsorbates on metal surfaces. *Reports on Progress in Physics* **1990**, *53*, 917–1002.

(7) Ikonomov, J.; Bach, P.; Merkel, R.; Sokolowski, M. Surface diffusion constants of large organic molecules determined from their residence times under a scanning tunneling microscope tip. *Phys. Rev. B* **2010**, *81*, 161412.

(8) Bartels, L.; Wang, F.; Möller, D.; Knoesel, E.; Heinz, T. F. Real-Space Observation of Molecular Motion Induced by Femtosecond Laser Pulses. *Science* **2004**, *305*, 648.

(9) Denk, R.; Hohage, M.; Zeppenfeld, P.; Cai, J.; Pignedoli, C. A.; Söde, H.; Fasel, R.; Feng, X.; Müllen, K.; Wang, S.; Prezzi, D.; Ferretti, A.; Ruini, A.; Molinari, E.; Ruffieux, P. Exciton-dominated Optical Response of Ultra-narrow Graphene Nanoribbons. *Nat. Commun.* **2014**, *5*, 4253.

(10) Ma, C.; Liang, L.; Xiao, Z.; Puretzky, A. A.; Hong, K.; Lu, W.; Meunier, V.; Bern-

holc, J.; Li, A.-P. Seamless Staircase Electrical Contact to Semiconducting Graphene Nanoribbons. *Nano Lett.* **2017**, *17*, 6241–6247.

(11) Talirz, L. et al. On-Surface Synthesis and Characterization of 9-Atom Wide Armchair Graphene Nanoribbons. *ACS Nano* **2017**, *11*, 1380–1388.

(12) Chen, Z. et al. Chemical Vapor Deposition Synthesis and Terahertz Photoconductivity of Low-Band-Gap N = 9 Armchair Graphene Nanoribbons. *J. Am. Chem. Soc.* **2017**, *139*, 3635–3638.

(13) Sanders, G. D.; Nugraha, A. R. T.; Saito, R.; Stanton, C. J. Coherent Radial-breathing-like Phonons in Graphene Nanoribbons. *Phys. Rev. B* **2012**, *85*, 205401.

4.2 C_{60} – Bi_4Te_3 Moiré Heterostructures

Yannic Falke, Nicolae Atodiresei, Oliver Gallego, Abdur R. Jalil, Gregor Mussler, Gustav Bihlmayer and Alexander Grüneis
C_{60} - Bi_4Te_3 Moiré Heterostructures
In preparation

Topological insulators have gained much interest in recent years due to their complex quantum physical properties. With thriving research in this field and their robustness against magnetic and electronic perturbation, TIs form the basis for next generation devices. While the interface of TIs with other materials is especially interesting, the materials used are usually of inorganic nature. Here we present the first report of a highly ordered, organic–topological insulator interface that is made up of C_{60} and Bi_4Te_3. C_{60} forms a good basis for the investigation of an organic interface material due to its high symmetry and formation of van der Waals crystals. These layered types of crystals are known to be able to grow in a well aligned manner as is the case in common 2D materials, such as MoS_2.

Monolayers of C_{60} are grown on top of a clean Bi_4Te_3 surface in ultra-high vacuum conditions by means of evaporation from a Knudsen cell. Through well defined control over evaporation rate and substrate temperature, a highly ordered monolayer formed with alignment along the symmetry directions of the underlying, hexagonal surface of the topological insulator. The alignment and high crystallinity were confirmed by low energy electron diffraction (LEED). Additionally, the existence

of a superstructure was found, that exhibits a moiré pattern in LEED. Through analysis of the LEED pattern we found this structure to be a (4×4) C_{60} on (9×9) Bi_4Te_3 pattern. The formation of a moiré pattern of an organic film on a topological insulator is not reported in literature yet, to the knowledge of the author.

The formation of this interface is further examined by means of density functional theory. Here, a single C_{60} molecule is relaxed onto the surface of the Bi_4Te_3 and the ideal adsorption site was found to be on top of a Te atom. This atom in turn is pushed into the surface by $\Delta z = 0.2\,\text{Å}$, which can be described as an inherent softness of the layer. The effect is further enhanced by formation of the (4×4) superstructure, where the deformation effect increases by $\sim 50\%$. The creation of valleys in the surface of the TI locks the C_{60} molecules in place, therefore forming a well aligned interface with slight strain of $\sim 2\%$ in the molecular layer. Finally, the electronic structure of the interface is determined through angle resolved photoemission spectroscopy. Here we find, that both the bulk and surface states of the topological insulator stay unaffected by the presence of the C_{60} monolayer. There is no or insignificant charge transfer from C_{60} to the Bi_4Te_3 or vice versa, which is astonishing since C_{60} is a good electron acceptor. This interaction is judged by the lack of hybridisation between the bands of the materials and the absence of any shift in the electronic states of the topological insulator at the Γ point.

Contributions to this publication:

- Main contribution to the publication come from Y. Falke and N. Atodiresei with smaller contributions from the co-authors.
- Perform all LEED and ARPES measurements at a synchrotron.
- Evaluate all gathered data.
- Create all figures except the individual DFT figures in Fig. 2.

Abstract

We present the formation of an organic moiré pattern of a C_{60} monolayer on the topological insulator Bi_4Te_3. We show the existence of the the pattern through low energy electron diffraction and confirm its structure as a (4×4) C_{60} superstructure on a (9×9) unit of Bi_4Te_3. The formation of this highly ordered interface is further studied using density functional theory. From these calculations it is evident, that the C_{60} buckyballs bond with the topological insulator through physisorption. We find the optimal bindings site for a single C_{60} molecule to be located above a Te atom, which in turn is pushed into the surface by the van der Waals and electrostatic interaction with the buckyball. This behaviour is amplified by the formation of the (4×4) superstructure where the atoms are pushed into the surface as much as 10% of their bond length. We identify the inherent "softness" of the TI surface as the driving force for the excellent order of the organic monolayer.
Additionally, the electronic structure of the interface is studied by means of angle resolved photoemission spectroscopy. Here we find that the the organic overlayer does not alter the electronic states of the underlying topological insulator. This is shown for both the bulk and surface states of the TI, which neither shift in energy nor show hybridization with the bands of C_{60}.

Introduction

Organic thin films prove to be a exciting system for use in metal or semiconductor interfaces due to their versatility in terms of electronic and magnetic properties. The incorporation of heteroatoms and transition metals into the organic structure paired with controllable interaction between surfaces allows for flexible modification of the interface properties. The Buckminsterfullerene C_{60} stands out as a highly symmetric compound that exhibits strong electron-photon interaction and even correlated behaviour when doped, with the additional benefit of encapsulation of atoms or even small molecules along with a high degree of available functionalizations.[63, 68, 84–86] Moreover, C_{60} is also used as an active element in organic devices. A major obstacle for organic device performance is the order of the organic layer and the interface. While condensing organic molecules into crystals or ordered thin films can be challenging due to chirality and anisotropy, C_{60} readily forms highly crystalline van der Waals bulk crystals with face-centered cubic structure. In thin films, it is known to form hexagonal pattern, which correspond to the (111) plane of the bulk system.[73, 74] This formation however heavily depends on the substrate-molecule and molecule-molecule interaction.[87] For organic molecules and C_{60} alike, these interactions have been mainly studied for interfaces with noble metals[75, 76], semiconductors and recently with 2D materials such as graphene and h-BN.[77, 88–93] The growth of ordered organic structures on topological insulators however has not been studied in depth yet although it allows for studying the stability of topological states and potential modification of the topological properties.[94–97] Here, we show growth of a highly ordered, long range structure of C_{60} on the novel topological insulator Bi_4Te_3.[98–101] Interestingly, the pattern exhibits a (4×4) superstructure in a (9×9) grid with regards to the underlying TI, which is observable as a moiré pattern in LEED. The formation of this superstructure is further investigated by density functional theory (DFT) and its electronic interaction with the TI is

studied using angle-resolved photoemission spectroscopy (ARPES).

Experimental details

Bi_4Te_3 films of 20 nm thickness were grown in a n-doped Si(111) wafer using molecular beam epitaxy (MBE) in a UHV chamber with base pressure $< 5 \times 10^{-10}$ mbar. Before exposure to air, the films were capped with an amorphous 2 nm selenium film. In a separate preparation chamber with base pressure $< 5 \times 10^{-10}$ mbar, the capping layer was removed by means of sputtering and annealing cycles with temperatures as high as 650 K until no improvement of the LEED spectrum was distinguishable any more. C_{60} (> 95.5% HPLC) was evaporated from a Knudsen cell at 700 K with an evaporation rate of 0.5 Åmin^{-1} as calibrated by a quartz microbalance (QMB). During evaporation, the substrate temperature was held at 400 K and post-annealed at 420 K for 30 min. ARPES measurements were performed using synchrotron radiation with photon energy of 21 eV at the BaDElPh beamline (ELETTRA).

Results

Low Energy Electron Diffraction

Bi_4Te_3 condenses in the form of a rhombohedral crystal structure ($R\bar{3}m$ space group) with the unit cell consisting of stacked quintuple layers (QL) with Bi_2Te_3 stoichiometry and Bi-Bi bilayers (BL). The surface termination with either a QL or BL alters the electronic properties of the surface states and can be resolved by ARPES.[99] In our case, the decapping and cleaning process leaves a pristine QL as the terminating layer, which is tied to the existence of a "V-shaped" surface state protruding the Fermi level around the Γ point, as shown in Fig. 4.3. The surface of the (111) direction of the crystal, i.e. the QL layer, forms a hexagonal grid, with Te and Bi located at different heights. This hexagonal lattice is described by the lattice constant $a_{\mathrm{hex}} = 4.501$ Å as determined by X-Ray Diffraction (XRD) experiments.[98] The matching reciprocal space LEED of the pristine Bi_4Te_3 thin film is shown in Fig. 4.1 a) where

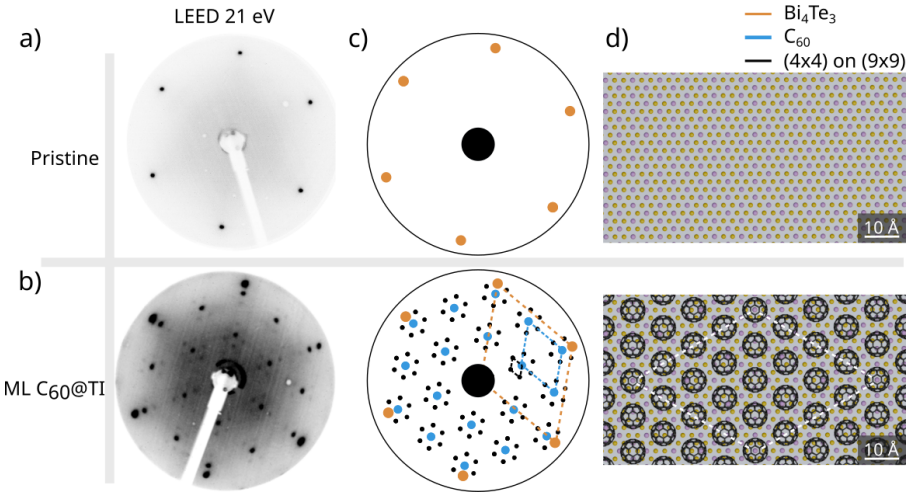

Figure 4.1: Experimental LEED pattern taken at 21 eV of a) pristine Bi_4Te_3 and b) a monolayer of C_{60} on Bi_4Te_3. c) Sketch of LEED pattern for increased clarity, different colors indicate the respective states given in upper right hand legend. d) Top down view on the 2D structure of pristine Bi_4Te_3 (upper) and (4×4) C_{60} superstructure on (9×9) Bi_4Te_3 (lower).

the small, sharp reflexes in a hexagonal pattern indicate a clean surface and high crystallinity. The LEED pattern is consistent over the whole sample area of $1 \times 1\,\mathrm{cm}^2$, proving the absence of possible rotational domains or inconsistencies of the surface and therefore provides and ideal basis for the ordered growth of a C_{60} thin film. After careful evaporation of a monolayer film of C_{60}, as described in detail in the experimental section, the sample is allowed to cool down to RT prior to LEED measurement. A LEED image of the C_{60}@Bi_4Te_3 system at an electron energy of 21 eV is shown in Fig. 4.1 b), with a sketch reproducing the observed diffraction spots in c). In addition to the spots on the outside of the screen, originat-

ing from the Bi_4Te_3 (orange), two sets of new spots appears much closer to the 00-reflex. These spots originate from the newly formed C_{60} monolayer (blue) and their small separation in reciprocal space indicates the large lattice constant. By assuming an unperturbed Bi_4Te_3 base layer, we obtain a lattice constant of $a_{C_{60}} = 9.79(2)$ Å by comparison of the spacing between the spots of both species. This hexagonal C_{60} lattice is subject to a 2% compressive strain in comparison to that of the (111) direction in a bulk crystal. The LEED spots are very sharp and show no sign of any rotational disorder caused by potential rotational domains, therefore providing direct representation of both the high local and long-range order of newly constructed interface.

This long-range order becomes even more clear by the existence of a moiré pattern (black dots in sketch) that is given by the appearance of the second, very small hexagon around each of the C_{60} spots. The pattern inherits the same orientation as the interface and is due to the formation of the arrangement of C_{60} molecules in a (9×9) superstructure with respect to the TI lattice, as sketched in Fig. 4.1 d). It contains (4×4) buckyballs per unit cell and is therefore defined by an exceptionally large hexagonal lattice vector of $4 \cdot a_{C_{60}} = 39.16(8)$ Å. While other studies have shown the growth of well ordered C_{60} and organic molecules on other topological insulators, we are the first one to report the existence of a moiré in this interface, therefore proving ultimate long-range order.

Density Functional Theory

We further investigate the properties of the TI–organic monolayer interface using DFT. Seven atomic layers of Bi_4Te_3 were used in all calculations for accurate description of the TI surface and bulk properties. In a first step, a single, "isolated" C_{60} is adsorbed and relaxed on the surface of the TI in order to determine the most stable adsorption sites and study the binding properties. Here we find, that the C_{60} molecule preferably relaxes into a position with a hexagon (that is the electron rich part) facing towards the surface with slight rotation, which is coherent with other findings

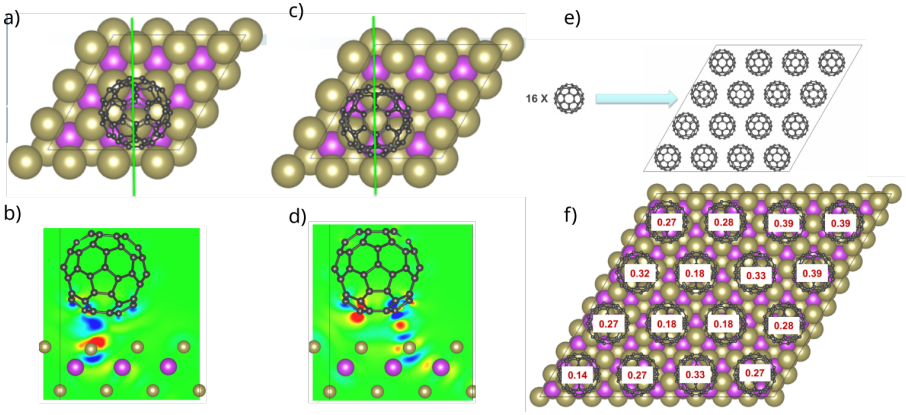

Figure 4.2: a) Most stable configuration of a single C_{60} molecule on Bi_4Te_3 with green line indicating a slice through the structure as shown in b). c) and d) show the the second most stable configuration. Blue and red colors indicate the relative accumulation and depletion of electrons respectively. e) Shows the isolated (4×4) C_{60} superstructure and f) shows the most stable configuration of the superstructure on the Bi_4Te_3 film with protrusion values Δz of the underlying Te atom in Å.

in literature.[94] Furthermore, this most stable configuration places the molecule on top of a Te atom with the slight rotation facing towards a "valley" of the topmost Te layer, as shown in Fig. 4.2 a). Interestingly, this interaction pushes the Te atom into the surface of the TI by $\Delta z = 0.21\,\text{Å}$ in comparison to the pristine layer. This "softness" potentially is one of the driving factors towards the excellent self-alignment of the C_{60} monolayer on top of the Bi_4Te_3.

The adsorption energies of the interface suggest that the binding is mainly driven by van der Waals interaction in combination with a very weak electrostatic contribution. The charge distribution is visualized in Fig. 4.2 b), proving the slight electrostatic effect whereas the lack of charge accumulation between C and Te show that no

hybridization between the two atoms occurs, further solidifying the purely van der Waals nature of the bond. However, a small charge transfer from the C_{60} to the Bi_4Te_3 remains, leaving the C_{60} slightly p-doped in this configuration. Fig.4.2 c) shows another possible configuration, which is slightly less favourable for the single C_{60} molecule with an energy difference of $\Delta E_{\text{relative}} = 0.018\,\text{eV}$. Here, the molecule sits between two Te sites and a slight accumulation of charge at C_{60} appears, making it slightly n-doped. The Te is not pushed into the surface as much in this configuration, with $\Delta z = 0.07\,\text{Å}$ and the binding energies still indicate the van der Waals adsorption onto the surface.

In a second step, we simulated the absorption of the (4×4) superstructure on the TI. Interestingly, we find that the packing energy between the buckyballs of the monolayer is higher (bond is stronger) than the energy between the monolayer and the substrate by $\Delta E_{inter} = 0.12\,\text{eV}$. This can on the hand explain the high degree of crystallinity of the monolayer, as found by LEED, and on the other might be the reason for the 2% strain of the system with respect to the unperturbed bulk. Additionally, the effect of C_{60} pushing the Te into the surface is stronger than in the case of a single C_{60} molecule with an average deflection of $\Delta z = 0.27\,\text{Å}$ and even reaching double the value of the single C_{60} deformation at some points, as shown in Fig. 4.2 f). Here, the z-height of the underlying Te atom is shown for every C_{60} member of the superstructure. The pattern can be described in the form of a two-dimensional wave which is generated by the different interaction strength of the individual molecules with different parts of the surface in the superstructure. This potentially locks the superstructure into place and might be a reason for the excellent alignment and long-range order of the interface.

ARPES

In order to investigate the effect of the adsorption of the C_{60} monolayer onto bulk and surface states of the topological insulator, ARPES measurements of the pristine and perturbed species were performed. Fig. 4.3 a)

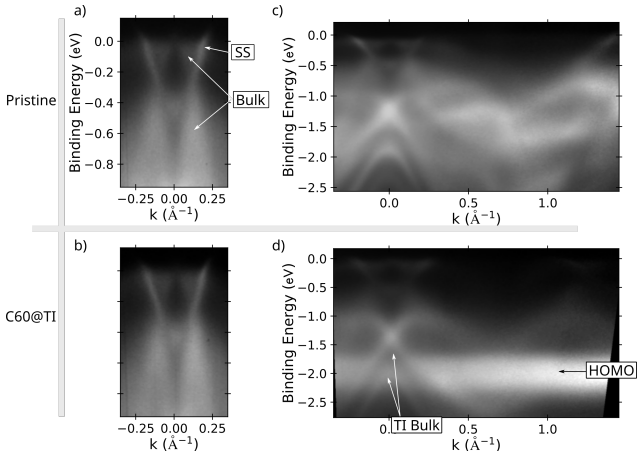

Figure 4.3: Room temperature ARPES measurements of pristine Bi_4Te_3 (upper) and C_{60}@Bi_4Te_3 (lower). a) Band structure close to the Fermi level with bulk bands and surface state (SS). b) Shows the same region of a) after deposition of C_{60}, no shift in any of the bands is observable. c) Γ K scan of pristine Bi_4Te_3 and d) C_{60}@Bi_4Te_3 with the C_{60} HOMO band, no hybridization of the bands is visible.

shows the electronic band structure of pristine Bi_4Te_3 close to the Fermi level, which is comparable to spectra in literature.[99–101] The "V-shaped" surface state (determined in recent work) along with other bulk states are clearly visible and indicate high crystallinity as well as the absence of doping. Fig. 4.3 b) shows an equivalent spectrum taken after deposition of a monolayer of C_{60}. Since both the surface state and bulk states are unperturbed, no charge transfer from the C_{60} to Bi_4Te_3 or vice versa is present, further proving the physisorption and weak interaction of the interface.

Fig. 4.3 c) and d) show long-range scans of the pristine and C_{60}@Bi_4Te_3 systems respectively. The pristine sample shows a plethora of bulk states in either direction Γ, whereas these states are suppressed by the very in-

tense HOMO band upon adsorption of C_{60}. Around Γ, the TI states are more intense than the bands of the molecular film, which is why the latter seems to vanish in this region. The lack of hybridization between the bands of both species further shows the weak interaction and undermines the correctness of our calculations. Additionally, the high degree of order in the molecular thin film is further undermined by the visible angular dispersion of the HOMO band in Fig. 4.3 d), which can only be present in a well ordered molecular crystal. Our measurements also show the resilience of the TI's surface states against perturbation which is induced by the disturbance of surface smoothness due to the existence of the C_{60} overlayer. This can be explained by the relatively small amount of perturbation sites. The C_{60} molecules only affect $4 \times 4 = 16$ out of $9 \times 9 = 81$ tellurium atoms in the superstructure unit cell. Furthermore, the bands of the topological insulator around the Fermi level mostly possess Bi character, which is why they are not affected much by the distortion at Te sites through the C_{60}.

Conclusion

We have shown the construction of a weakly interacting interface between the topological insulator Bi_4Te_3 and a highly ordered C_{60} thin film and investigated its electronic properties. We have found that C_{60} crystallizes with long-range order which is not yet reported for the case of a TI–organic molecular film interface. Its formation and origin were explored in detail using ab-initio calculations that show a slight deformation of the topology of the TI. The driving force of this interaction is mainly van der Waals based with the addition of slight electrostatic forces present, that can explain the deformation of the substrate surface and the existence of a moiré pattern in this interface. The formation of this new interface does not alter the electronic states of either the surface or bulk states of the underlying topological insulator, which was explored using ARPES. This marks this system as an ideal protection of the topological insulator by construction of a weakly interacting interface with a molecular thin film. Additionally,

this system might be used as a basis for introduction of another, highly ordered film attached to the buckyball by altering the highly flexible C_{60} molecules.

Chapter 5
Organic Superconductor Rb_3C_{60} on Topological Insulator Bi_4Te_3

In the following chapter we show the growth of the organic, fullerene based superconductor Rb_3C_{60} on the topological insulator Bi_4Te_3. This kind of interface has not been reported before in literature. We study the growth using LEED and UPS and briefly characterize the electronic band structure in a home-built UHV setup and confirm the phase purity of the final Rb_3C_{60} thin film on TI.
Yannic Falke developed the synthesis method, performed all measurements at home, built up the entire UHV-ARPES system and evaluated the presented data. The findings were developed based on work at multiple beamtimes, which Oliver Gallego, Niels Ehlen and Alex Grüneis contributed to. This work is unpublished yet.

5.1 Introduction

Alkali metal doped fullerenes in the form of A_xC_{60} single crystals have been studied extensively due to their interesting electronic properties. They crystallize in multiple phases with forms reported for $x = 1, 3, 4, 6$, each exhibiting unique behaviour. The most interesting phases consist of A_3C_{60} and A_6C_{60} as they are stable at room temperature and ambient pressure. K and Rb based $x = 3$ structures are metallic at room temperature and exhibit superconductivity with relatively high transition temperatures of $18 - 28\,\mathrm{K}$. Cs_3C_{60} fullerene crystals however are Mott insulators at ambient conditions and transitions into a metallic/superconducting phase under application of high pressures. This

behaviour is directly related to the lattice parameters of the crystals. Whereas potassium, as the smallest of the three alkali metals, shows a minor expansion over the pristine C_{60} crystal, the incorporation of the larger alkali metals is followed by larger lattice constants. Here, the rubidium based fullerene provides the ideal balance of expansion and carrier distribution and shows the highest superconducting transition temperature of the three. Expanding the lattice to higher values, as is the case with Cs, the system turns insulating and only through the application of pressure (compression of the lattice) it becomes metallic again. This marks the precise control over the lattice parameters of these systems as an important point.

Switching from single crystals to thin films of these fullerene based superconductors introduces new challenges. While the van der Waals nature of these films allows for growth on a wide variety of substrates, the control of their order is critical in achieving high performance structures. Disorder in these films results in scattering sites which inhibit the carrier distribution and can lead to the break down of the superconducting transition of the film. Additionally, much increased surface area of these thin films leads to a high exposure of the highly reactive alkali metal to contamination. This in turn makes the synthesis of well defined, pure films non-trivial.

Another important factor in the performance of the thin films is their phase purity with respect to the A_6C_{60} contributions. Whereas the half filled LUMO acts as the conduction band in the A_3C_{60} films, the introduction of three more electrons results in the full occupation of this band, making it insulating. While the control over the amount of alkali metal dopant between $A = 3$ and $A = 6$ might sounds trivial, the pic-

ture is more complex. The problem lies in the instability of the other A_xC_{60} phases at room temperature. Upon introduction of a dopant concentration slight above $x = 3$, parts of the sample will immediately form $x = 6$ phases and make up for missing dopants by leaving other parts in an undoped $x = 0$ phase. This behaviour calls for the need of an extremely precise control over the amount of alkali metal dopant in the system for highest performance thin films.

Topological insulators have sparked much interest in recent years as they provide quantum properties that are robust against perturbation and therefore show significant potential for new device architectures.[102] A major base system for this kind of materials are Bi – Se and Bi – Te based heterostructures. Their layered structure allows for modification of the structure with adatoms and a plethora of different phases, all of them exhibiting novel topological properties.[103–106] The interface of an *s*-wave superconductor and a topological insulator has turned out to be an especially interesting field. Fu and Kane [107] predicted that the superconductor induces a proximity effect. This in turn generates vortices that can theroretically support Majorana bound states. Much work has been put into studying these interfaces, where a major complication arises from potential alloying between the (inorganic) superconductor and the underlying TI. This alters the properties of the TI and can lead to a break down of its properties. Therefore, the use of a van der Waals bonding, organic superconductor in this interface could overcome these drawbacks and will be explored in the following section.

5.2 Characterization of Bi_4Te_3

Bi_4Te_3 is one of the stable phases of the Bi–Te binary system, with other common phases being the Bi_1Te_1 and Bi_2Te_3. All of these phases crystallize in a layered, trigonal structure and are differentiated by their c-axis stacking parameters. The stacking layers come in the form of Bi–Bi *bilayers* (BL) and Bi_2Te_3 *quintuple* layers (QL), as shown in Fig. 5.1 a). With this stacking order in mind, Bi_4Te_3 can also be rewrit-

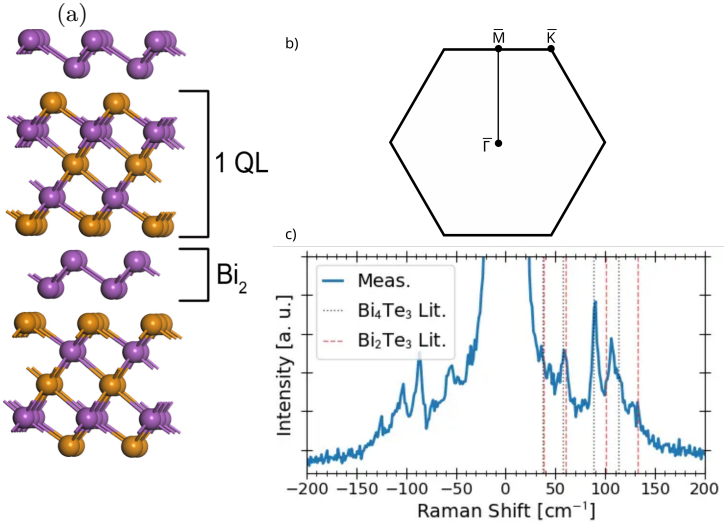

Figure 5.1: a) Stacking of layers in the Bi–Te binary systems, highlighting the quintuple (QL) and bi-layers (BL), taken from [108]. b) Sketch of the two dimensional surface Brillouin zone with high symmetry points. c) Low wavenumber Raman spectrum ($\lambda = 633\,\mathrm{nm}$) of Bi_4Te_3, with black and red lines indicating peak positions from literature [108].

ten as $(Bi_2)_3(Bi_2Te_3)_3$ with a c-axis lattice constant $c_{\mathrm{hex}} = 41.98\,\text{Å}$ in

the stacking direction. The different phases of the binary system possess different electronic properties and can be separately synthesized by careful control over the Bi and Te flux during growth via molecular beam epitaxy (MBE).
The individual layers exhibit a hexagonal lattice with lattice constant $a_{\mathrm{hex}} = 4.45\,\text{Å}$. As a consequence, the surface Brillouin zone is of hexagonal shape as well, with high symmetry points $\bar{\Gamma}$, $\bar{K}$ and $\bar{M}$, as shown in Fig. 5.1 b).
20 nm thin films were obtained from a collaborator (A. Jalil, FZJ) and were capped in UHV with a 2 nm amorphous selenium film prior to exposure (and shipping) to air. The substrate for growth is a $1 \times 1\,\mathrm{cm}^2$ doped Si(111) wafer, whose hexagonal surface provides a suitable growth site. The doping is critical for electronic measurements for any film deposited on the silicon as charge accumulation would occur otherwise. The correct Bi_4Te_3 phase of the synthesized sample along with the corresponding lattice constants were proven by means of X-ray diffraction, performed by the collaborator.
The obtained samples were prepared in UHV by repeated cycles of Ar^+ sputtering and annealing to temperatures of 600 K. This procedure is necessary for removal of the Se capping layer and to remove a few topmost layers, that could have been subject to contamination with Se. To prove intactness of the sample after annealing to high temperatures, low wavenumber Raman spectroscopy was carried out in ambient conditions, as shown in Fig. 5.1 c). The spectrum shows three distinct peaks at $60\,\mathrm{cm}^{-1}$, $89\,\mathrm{cm}^{-1}$ and $105\,\mathrm{cm}^{-1}$. The middle, $89\,\mathrm{cm}^{-1}$ peak, is a fingerprint of Bi_4Te_3 and not known in other Bi–Te phases. The right, $105\,\mathrm{cm}^{-1}$ peak can not be assigned unambiguously but the absence of

a peak at 131 cm^{-1} highlights the absence of the Bi_2Te_3 phase in the sample. The Raman spectroscopy measurements therefore underline the stability of the Bi_4Te_3 phase at elevated temperatures.
In UHV, the cleanliness and crystallinity of the sample surface is determined through LEED measurements, as shown in Fig. 5.2. All spots are

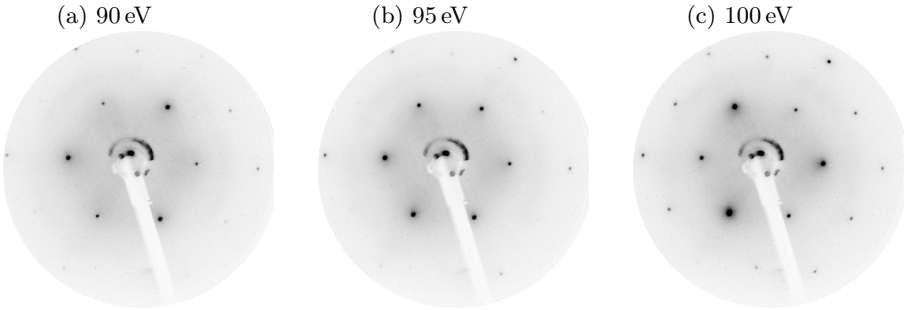

Figure 5.2: LEED pattern of pristine Bi_4Te_3 after sputtering and annealing at a) 90 eV b) 95 eV and c) 100 eV.

sharp and clearly visible with no signs of rotational disorder, therefore proving high crystallinity and the surface being free from the amorphous Se capping layer. The LEED pattern show the hexagonal surface structure of the topological insulator. This pattern is a direct representation of the surface Brillouin zone, as shown in Fig. 5.1 c). Knowledge over the orientation of the sample is critical for alignment of the ARPES setup in order to measure the band structure along the high symmetry directions of the crystal. While tuning the incident electron beam energy during LEED acquisition, the relative intensities of the first order hexagonal spots change. At 90 eV, three spots are clearly more intense than the remaining three counterparts, whereas at 100 eV the intensi-

ties appear reversed. At 95 eV all six spots appear at nearly the same intensity. This behaviour is due to the trigonal symmetry and layered structure of the sample.

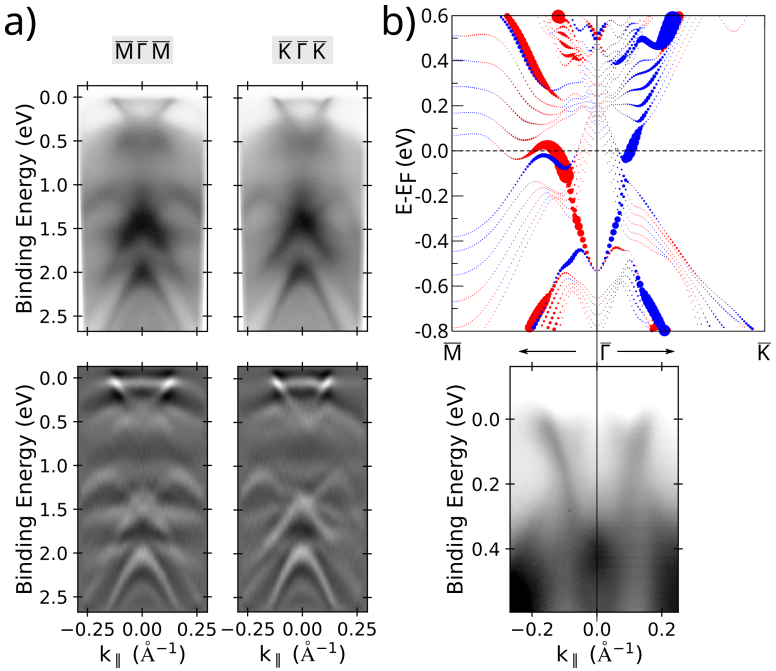

Figure 5.3: ARPES measurements of Bi_4Te_3 at 21 eV. a) Overview scans along high symmetry directions showing the raw data (upper) and second derivative (lower). b) DFT calculations for QL terminated Bi_4Te_3 close to the Fermi level along high symmetry directions (upper). Thickness of the points is proportional to the surface character, color indicates spin polarization. Experimental results close to the Fermi level with matching high symmetry directions (lower).

The electronic properties of Bi_4Te_3 were investigated using angle-resolved photoemission spectroscopy (ARPES). The measurements were performed in-house, making use of a He gas discharge lamp, which provides an 21.2 eV excitation source. The sample temperature was kept at 130 K throughout all measurements, which is the minimum achievable temperature of the setup. With knowledge of the sample orientation, scans along the $\bar{M}\bar{\Gamma}\bar{M}$ and $\bar{K}\bar{\Gamma}\bar{K}$ directions were taken, as shown in Fig. 5.3 a). The upper panel shows the raw data whereas the lower panel shows the second derivative. At high binding energies, multiple bulk bands are clearly visible with well defined dispersion along the high symmetry directions. Fig. 5.3 b) (upper) shows a DFT band structure calculation of the bands near the Fermi level. The size of the individual points corresponds to the surface state character of the bands i.e. large points originate from the surface, small points from the bulk. The color of the points indicate spin polarization. A "V-shaped" surface state with a minimum at $E - E_F = -0.5$ eV is clearly visible along with surrounding bulk bands, one of which has the shape of a "reversed V" that intersects the Fermi level. These bands match the measured ones in the lower panel. Here, the surface state is very intense and its dispersion towards the $\bar{M}$ and $\bar{K}$ point differ slightly, matching the DFT calculations. It is intersected by the weaker bulk bands whose maximum lies above the Fermi level. Shifts of the maxima/minima of both states with respect to this pristine sample can be used to judge potential doping of the TI. The surface state character of the "V-shaped" band was confirmed using synchrotron radiation.

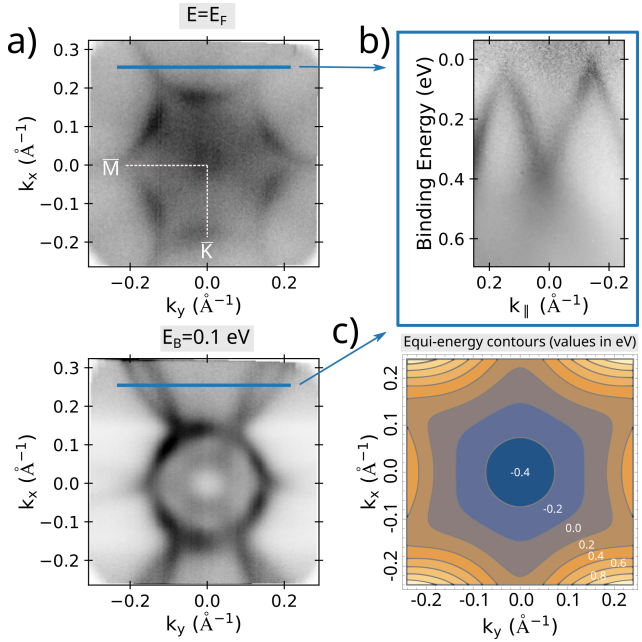

Figure 5.4: Fermi surface maps of Bi_4Te_3 at 21 eV. a) Equi-energy cuts at $E_B = E_F$ (upper) and $E_B = 0.1$ eV (lower). b) Slice along the blue line indicated in a). c) Tight-binding calculation showing hexagonal warping of the equi-energy contours at different energies.

The electronic structure of the pristine Bi_4Te_3 was further investigated by means of Fermi surface mapping, as shown in Fig. 5.4 a). The upper panel shows an equi-energy cut at $E = E_F$. In the very center, a small circular of the bulk band is visible. At higher k values, the Fermi surface of the surface state is visible as a hexagon with lines tracing outwards. It has to be pointed out, that this hexagon is rotated by 30° with respect to the surface Brillouin zone, so the hexagon cor-

ner of the Fermi surface corresponds to the $\bar{M}$ point of the Brillouin zone. Whereas the band structure of an ideal metal forms a cone with a matching, circular Fermi surface, the deviation from this circular shape into a hexagonal one is called hexagonal warping. Hexagonal warping is a feature of topological states and has been observed in the related Bi_2Te_3 phase[109], whereas trigonal warping is known at the K points of graphene.[110] The hexagonal symmetry of the warping results in increased nesting of the Fermi surface, which can potentially have an effect on optical and other electronic properties, as it is, for instance, the case in charge density waves in VSe_2. [83, 111]
The bands stretching out from the hexagon corners ($\bar{M}$ directions) represent nodal lines.[112, 113] These are flat lines along the Fermi surface at which conduction and valence bands touch and disperse between the individual Brillouin zones and are linked to the existence of Dirac cone like features in the band structure.
Fig. 5.4 b) shows a slice through two nodal lines, as indicated in a). The slice shows the existence of Dirac cones, whose maxima are located at the Fermi level. These cones perturb along the path of the nodal lines and connect the nearest Brillouin zones. The band contributions arise partially from both surface and bulk states and can potentially possess interesting carrier properties, as is the case in graphene. The lower panel in Fig. 5.4 a) shows an equi-energy cut at $E_B = 0.1\,\mathrm{eV}$. Here, the nodal lines open up into so called flower-petal states. This is directly tied of the existence of the Dirac cones. The bulk band contribution becomes clear, as the innermost circular state branches out into the flower petals.
Finally, 5.4 c) shows tight-binding calculations of equi-energy contours

of the hexagonal warping of the band structure. The tight-binding Hamiltonian was constructed following reports of the hexagonal warping in Bi_2Te_3.[109] The cone of the topological insulator evolves into a stretched hexagon for values close to and above the Fermi level, which is consistent with the experimental findings.

5.3 Rb_3C_{60} on Bi_4Te_3

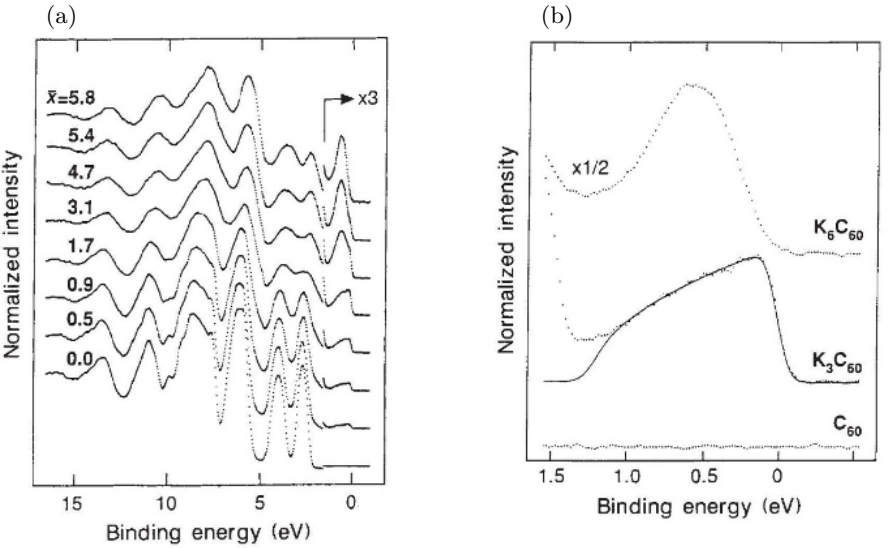

Figure 5.5: Photoemission spectra of K_xC_{60} by Chen *et al.* [114] a) UPS scans of K_xC_{60} as a function of alkali metal dopant x. b) Magnification of the C_{60}, K_3C_{60} and K_6C_{60} close to the Fermi level.

Rb_xC_{60} and K_xC_{60} is stable in different phases with respect to the amount of incorporated alkali metal, where early reports[114] found

that the $x = 3, 6$ phases are the most stable at room temperature. Chen *et al.* studied photoemission of the potassium phases by deposition of a C_{60} film on a metallic substrate with following potassium evaporation and annealing to elevated temperatures of 100 °C. The photoemission spectra in Fig. 5.5 a) show UPS scans of K_xC_{60} as a function of potassium $x = 0 \ldots 6$. From $x = 0$ to $x = 3$ there is a gradual increase of intensity close to the Fermi level, which is governed by the metallic character of K_3C_{60}. For higher concentrations, there is a shift of intensity from the Fermi level towards higher binding energies, which arises from the existence of the insulating K_6C_{60} phase (compare Fig. 5.5). In tandem with XPS, they were able to confirm that all photoemission spectra with a concentration between the stable phases are solely made up of the two separate phases, K_3C_{60} and K_6C_{60}. They proved, that no other phases can be present at room temperature.

In order to obtain well defined, superconducting films of pure K_3C_{60} and Rb_3C_{60} the control over the concentration of alkali metal in the sample is crucial. In the case of synthesis of pristine K_3C_{60}, early works relied on the gradual doping approach as used by Chen *et al.* in which the alkali metal is deposited over a certain time and annealed right after. Obtaining a pristine K_3C_{60} film using this method is not ideal, since under- or overdoping can happen easily. In recent years, a novel approach was developed for synthesis of K_3C_{60} on metal substrates that makes use of the higher thermal of K_3C_{60} over K_6C_{60}. Here, potassium is evaporated for 20-60 s onto a thin film of C_{60}. Due to the small diameter of potassium, it can diffuse into the organic layer within minutes at room temperature and slowly advances towards the $x = 3$ phase. After each deposition step, photoemission spectra are taken which show

a gradual increase of intensity close to the Fermi level. The entire process has to be performed in a short amount of time (~ 2 hours) because of the high reactivity of the alkali metal overlayer. When no further change in the photoemission spectrum is noticeable, i.e. the film is fully doped into the K_6C_{60} phase, the sample is annealed at high temperatures of 240-260 °C. This temperature however is very close to that of desorption of the entire molecular film but is able to leverage the higher thermal stability of the K_3C_{60} phase in comparison to the insulating K_6C_{60} phase. With this novel method, pure K_3C_{60} thin films can more readily be synthesized on metallic substrates.

By switching from the potassium to the rubidium based fullerene, the onset of transition from the metallic to the superconducting state is shifted towards higher temperatures, which is what makes Rb_3C_{60} favourable. However, the synthesis method described above seems to fail in that case. This can be explained by the increased diameter of rubidium versus potassium. The larger size results in much longer diffusion times at room temperature, that takes above synthesis method from 2 hours to >10 hours until full doping is achieved. During this time, the reactive Rb overlayer can degrade and form other species, which hinder the formation of a pristine Rb_3C_{60} phase. Due to this challenge in preparation, angle resolved photoemission spectra of pure Rb_3C_{60} thin films have not been reported yet.

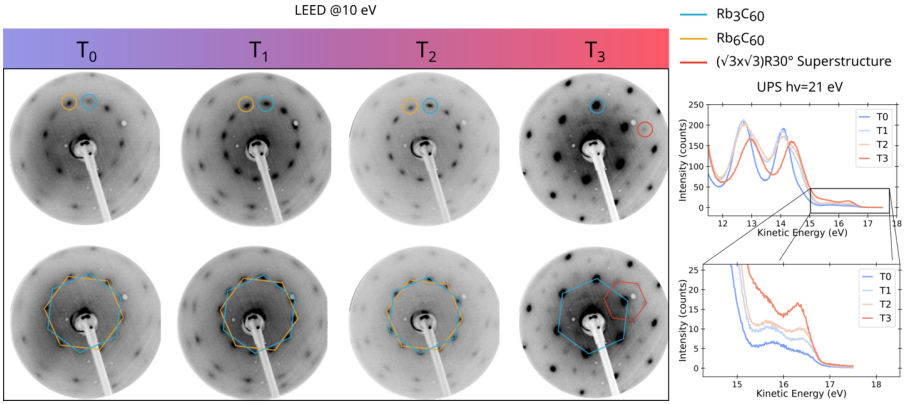

Figure 5.6: LEED pattern at 10 eV (left) for different annealing temperatures and matching UPS spectra (right).

In this work, a novel approach for thin film synthesis of Rb_3C_{60} was developed that builds upon the current findings in literature but additionally leverages the abilities of LEED to optimize the process. A thin film of C_{60} was evaporated onto a clean Bi_4Te_3 substrate, resulting in a well defined structure as discussed in detail in Section 4.2. Afterwards, a thick film of rubidium was evaporated onto the sample over a course of 15-20 min. The sample was then step-wise annealed to elevated temperatures. For each step, LEED and UPS spectra were taken, as shown in Fig. 5.6. The sample was allowed to cool down before the measurements. Starting with a low annealing temperature T_0 the LEED pattern shows circular pattern, which is made up of two hexagonal pattern that are rotated by 30° with respect to each other. In UPS, two peaks close to the Fermi level are visible, of which the left corresponds to the insulating Rb_6C_{60} phase and the right to the metallic Rb_3C_{60} phase. The insulating peak is more intense, which is directly correlated with the existence

of a higher fraction of Rb_6C_{60} in the sample. This is also observable in LEED, where the intensity of the corresponding spots (orange) is higher than the ones originating from the Rb_3C_{60} phase (blue). Increasing the temperature over T_1 to T_2 shows the increase of metallic fraction in the sample. The intensity of the LEED spots becomes equal for T_1 and then flips for T_2. The same behaviour is seen in UPS, where the relative intensities of the two metallic peak starts to increase. At the optimal temperature T_3, a major change is observable. The LEED pattern now consists of a single hexagon that corresponds to the metallic Rb_3C_{60} phase. The much increased intensity of the spots (increased brightness) is a consequence to the metallic nature of the sample. In UPS, the metallic phase in much enhanced whereas the insulating phase can not be detected any more. The remaining intensity at the position of the former Rb_6C_{60} phase originates from the underlying Bi_4Te_3, which can be seen in ARPES. This proves that this optimized procedure is capable of consistent production of Rb_3C_{60} thin films by careful control over the annealing temperature in tandem with LEED. Furthermore, this is the first report of the growth of a fullerene based metal/superconductor on a topological insulator to the knowledge of the author.

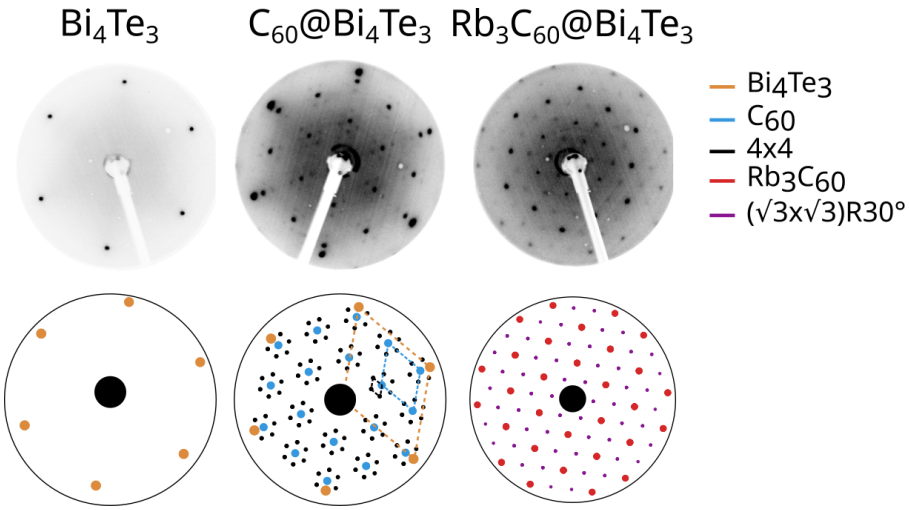

Figure 5.7: LEED images taken at 21 eV and sketches of the pattern of Bi_4Te_3 (left) C_{60}@Bi_4Te_3 (middle) and Rb_3C_{60}@Bi_4Te_3 (right).

In addition, another hexagonal pattern is visible in the LEED image at T_3, highlighted in red. This pattern has the form of a $(\sqrt{3}\times\sqrt{3})R30°$ superstructure. Its unique structure is not present in the case of pure C_{60} on the topological insulator, as shown in Fig. 5.7. This kind of superstructure can form due to electronic correlations and can potentially form charge density waves or related electronic effects. A similar structure has been shown in a recent work on K_3C_{60}@Gr@SiC by Ren *et al.*[115] Their STM measurements showed that the superstructure is insulating and vanished when increasing the layer count above the monolayer limit.

The electronic properties of the Rb_3C_{60} thin film on Bi_4Te_3 in this work were briefly studied by ARPES, as shown in Fig. 5.8 a). Close to the Γ

point, the Fermi surface of Bi_4Te_3 with hexagonal warping and nodal lines are visible. At $k \approx 0.3\,\text{Å}^{-1}$, a new, circular Fermi surface is visible, which corresponds to the metallic Rb_3C_{60}. Irregularities in measured intensities of the circular pattern are due to experimental issues of the photoelectron detector screen. The circular shape is expected for an ideal metal and was reported in literature by [116] for the case of a K_3C_{60} thin film on Au(111) single crystal. Interestingly, the observed band of the Rb_3C_{60} in this work intersects the nodal lines of the topological insulator. These are the points where Dirac cone like features exist so that potential electronic interaction between the fullerene and the TI are possible at these points. Due to low statistics of the ARPES measurements, no further information can be extracted but these measurements show the first report of the electronic structure of Rb_3C_{60} on a topological insulator to the knowledge of the author.

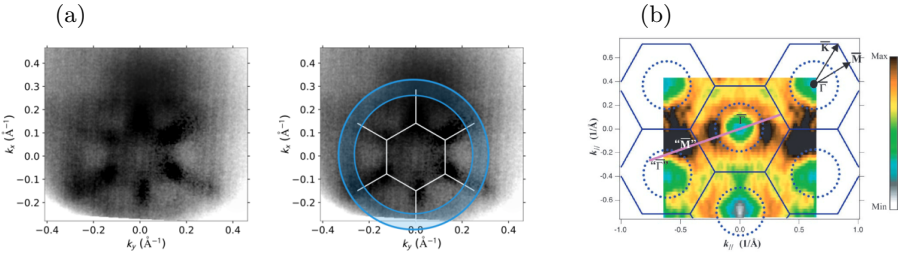

Figure 5.8: Fermi surface map of a) Rb_3C_{60}@Bi_4Te_3 around the Γ point at room temperature (left) with a sketch of the bands (right) and b) K_3C_{60}@Au(111), taken from [116].

Chapter 6
Discussion

This chapter discusses the results shown in the manuscript sections in further detail. The main points of the thesis are put into context with related, published work.

6.1 Graphene Nanoribbon Junctions

The fabrication of nanoscale heterostructures has been a major field of interest in recent years. These structures are aleady used in the form of GaAs/$Al_xGa_{1-x}As$ vertical heterostructures for fabrication of laser diodes, solar cells and photodetectors. [117, 118] Here, the combination of the two closely related structures with different bandgaps allows for the creation of high performance p–n junctions. Other work has focused on creating stacked van der Waals heterostructures by exfoliation of monolayers or MBE growth.[119] These methods methods offer a way for precise control over the stacking order and alignment of the structure (exfoliation) or fabrication of large area samples (MBE). This allows for the investigation of the interface properties through means of optical, electronic and magnetic measurements. The number of stacking layers however is limited due to the complexity of the methods and can not provide access to a large number of heterojunctions.
Graphene nanoribbon heterostructures are inherently different from the inorganic semiconductor and van der Waals heterostructures in that the bottom–up approach allows for formation of one–dimensional, lateral interfaces with atomic precision.[17] As shown in parts of this thesis, the bottom–up approach allows for the precise control over the bandgap

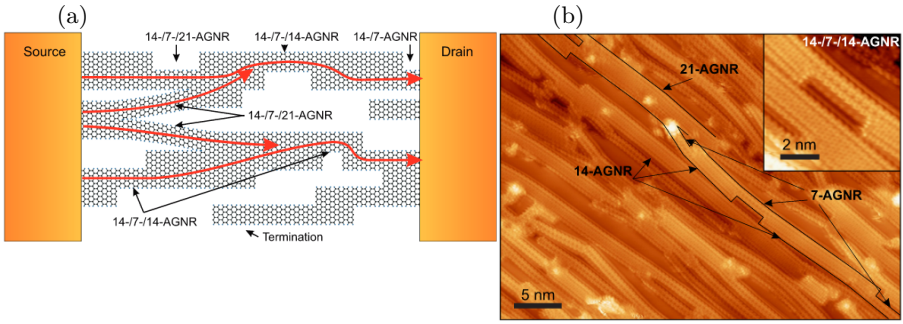

Figure 6.1: Device containing 7-/14-/21-AGNR heterojunctions. a) Sketch of the device showing graphene nanoribbons of multiple widths with possible junctions between AGNRs of different width. Red arrows trace the path of electrons travelling through the GNRs from source to drain. b) STM image of the GNR heterojunctions with black outline tracing a possible conduction path. Inset shows a close-up measurement of a typical 14-/7-/14-AGNR junction. Reprinted with permission from ref. [17] © 2021 ACS.

and electronic properties through the careful design of selected precursor. The chosen GNRs can be incorporated into devices and show excellent performance e.g. in the case of photodetection over conventional, graphene based detectors.[18]

In recent work by Senkovskiy *et al.* [17] a device containing heterojunctions between 7-AGNRs and 14-AGNRs was designed and its electronic transport properties investigated. They prove that the constructed device acts as a tunneling field effect transistor (TFET). These novel transistors could act as highly energy-efficient devices in the future and might furthermore be useful in applications such as chemical sensing.[120–122]

Fig. 6.1 a) shows a sketch of the device, in which source and drain are connected through graphene nanoribbons of different widths. The device contains multiple, aligned paths of GNRs which connect source and drain electrodes. These paths consist of junctions between GNRs of different width, which are multiples of 7 (14, 21 etc.). Here, the 7-AGNRs form semiconducting barriers due to their band gap wheres 14- and 21-AGNRs are quasi metallic and therefore form the conductive path.

The validity of this model is confirmed through STM measurements as shown in Fig. 6.1 b). These measurements show multiple GNR paths that consists of the 14-/7-/14-AGNR and similar junctions described above. STM shows the very well defined width of the GNRs, which can only be obtained through the bottom–up synthesis method.

The GNRs in their work were synthesized through the conventional bottom–up method on a stepped Au(788) bulk crystal, whose stepped terraces define the alignment of the ribbons. Through careful control over the heating times and temperatures, the ratio between 7-AGNRs and 14-AGNRs (and higher ones) can be regulated. Optimization and repeatability in different setups of this process however is very time consuming, as slight changes or misbehaviour in temperature control affect the final ratio of the ribbons. Additionally, this process does not allow for control over the lateral position of the junctions on the crystal surface.

This is where the photothermal bottom–up process, which was developed in this work, could further optimize the growth of GNR based TFETs. By depositing the molecular precursor on a thin gold substrate, it is feasible to ”draw” an entire circuit of graphene nanoribbons

directly on the surface of the GNR using thermal heating of a laser. The the ratio between semiconducting 7-AGNRs and quasi-metallic 14-AGNRs could then be controlled very precisely through heating time of a local spot and directly be investigated through means of Raman spectroscopy. Of course, the method used in this thesis is limited in terms of lateral size control through the laser spot size and thus does not allow for heating individual segments of single GNRs.
Recent developments in tip enhanced Raman spectroscopy (TERS) [123] however made it possible to perform Raman spectroscopy in the nm range. Here, a metallic tip, which is commonly used in STMs, focuses and amplifies the electromagnetic field underneath the tip. This allows for more precise lateral control of the measured Raman signal and could be used in combination with highly focused X-rays to apply heat to a sample in a very small area and measure its Raman response.

6.2 Self-assembly of organic structures on topological insulators

The interaction of topological insulators with other classes of materials such as semi- or superconductors is of great interest for the creation of next generation devices. Construction of an interface between TI and organic molecules opens up a vast playground for both theoretical and experimental scientists due to the large number of possible functionalizations of organic molecules. However, access to well defined, ordered organic layers on inorganic topological insulators is challenging due to the need for fine balance over substrate-molecule and molecule-molecule interaction.

Recent work by Bathon *et al.* [96] focused on the the self-assembly of molecular networks on the surface of the topological insulator Bi_2Te_3. Here, phthalocyanine (Pc) based molecules that each incorporate a specific transition metal were studied for the cases of Mn, Co and Cu. These planar molecules proved to be ideal systems for the construction of well oriented interfaces due to their two dimensional nature. Through STM measurements, they showed that some species were able to create very well ordered, long range structures when deposited on the TI, but others did not. They found, that the interaction of the Mn-Pc with the underlying substrate is strong and overcomes the molecule-molecule interactions, therefore leading to the formation of distorted layers. For Co-Pc and Cu-Pc they showed significantly less interaction with the substrate and therefore much better creation of a well ordered structure on the TI surface. While they relied on the interaction of the metallic center of the metal-organic structure to couple with the TI, our work avoids

this metallic component by use of pristine C_{60}. As discussed, we find that the low substrate-molecule interaction but rather strong molecule-molecule interaction allows for the construction of a well ordered, long range structure. In our case, we were even able to show a long range superstructure by low energy electron diffraction over a sample size of $1 \times 1\,\mathrm{cm}^2$. Through their STM work, they were able to point out the importance of the $d_z{}^2$ orbital for bonding with the surface, which is given by the implementation of the transition metal. The C_{60} molecule in our work does not inherit these orbitals but is still able to form well defined structures, which can open up the field of ordered organic structures of purely *sp*-hybridized molecules on topological insulators.

Other work by Jakobs *et al.* [124] focused on the control over the electronic band structure of the topological insulator Bi_2Se_3 through adsorption of the hydrogenated phthalocyanine H_2Pc and sulfurized H_2Pc^S in addition to C_{60}. Through density functional theory calculations they found that these three molecules represent bonding through strong chemisorption (H_2Pc^S), weak chemisorption (H_2Pc) and physisorption (C_{60}). The influence of these three bonding states on perturbation of the underlying TI was then studied using angle resolved photoemission spectroscopy. By clever use of a laser as an excitation source, they were able to probe the interface even in the presence of multiple layers of organic material. Lab based, laser photoemission spectroscopy (LPS) replaced the conventional helium discharge lamp, which yields an excitation energy of $h\nu = 21\,\mathrm{eV}$, with a high energy laser of $h\nu = 5.9\,\mathrm{eV}$, in their case. The resulting photoelectrons posses a larger mean free path and can therefore probe deeper into the interface/bulk. It comes with the drawback of very limited angular probing

range (small k space), which however is not an issue when studying the band dispersion close to the Γ point only, which is the case in their work. Using this setup, they were able to show that the chemisorbed species significantly interfere with the electronic band structure of the TI, while C_{60} leaves the structure unaltered. This is in very good agreement with our work and highlights the C_{60} molecule as an efficient way for protection of the topological surface states. While their work does not focus on the structural properties, we can advance on this by proving the intactness of the TI surface over a long range and in the presence of the moiré superstructure. Laser based ARPES could be a useful tool for further studies of the Rb_3C_{60} based systems.

Chapter 7
Conclusion and Outlook

In this thesis, several ways towards the synthesis of highly ordered organic layers and ribbons on multiple substrates have been explored. These included the creation of a novel synthesis route for bottom–up graphene nanoribbons through photothermal heating in combination with Raman spectroscopy as well as introducing a C_{60} based organic moiré superstructure on an inorganic topological insulator. Furthermore, the possibility of growth of an alkali metal doped, fullerene based organic superconductor on an inorganic topological insulator was studied.

All experiments were performed in ultra-high vacuum (UHV) conditions to provide optimal cleanliness and the critical stability against oxidation of all systems. Use of a specially designed UHV Raman system [125] allowed for the collection of spectra using very high laser powers, which made the realization of the novel growth method possible. The setup was further optimized for the investigation of the growth mechanism of GRNs. Where conventional bottom–up fabrication makes use of bulk gold crystals as the catalytic substrate for the Ullmann-type reaction towards GNRs, 100 nm thin crystalline films of Au/MICA were used in this scope. Using these thin films makes it possible to introduce a significant amount of heat into a single spot on the sample, since the heat cannot be dissipated easily. The spot size is defined by the laser beam, which is coupled into the UHV setup and is $\sim 15\,\mu m^2$ big. The temperature rise on the sample can be easily controlled by tuning the power of the laser and the ability to immediately turn the heating

ON/OFF made studying the reaction kinetics of GNRs possible. The real temperature on the sample can be measured with high accuracy using the ratio between Stokes- and Anti-Stokes peaks in Raman scattering. Existence of pure or even fused ribbons was proven using Raman spectroscopy at low laser power, so that it would not advance the reaction and allow the investigation of a single, stable state only. With this novel approach, the growth kinetics of 7-AGNRs, 13-AGNRs and Chevron ribbons as well as the fusion of 7-AGNRs to 14-AGNRs were studied. We examined the ability of the precursor molecules to move on the surface in combination with steric hindrance for initial formation of oligomers as a crucial step of the GNR growth. This knowledge could be critical for growth of new GNRs structures based on different precursors in the future. Furthermore, the easy tunability of the laser power in combination with a small probing spot size allows for the measurement of basically infinite points on a single substrate. This can be a major point in saving time for optimization of growth of new GNRs, where the conventional bottom–up approach on the bulk crystals can only produce a single sample at a given time, which is far less efficient than the photothermal approach.

An in-house ARPES setup (which was set up by the author in the proceedings of this thesis) was used for investigation of the self-assembly of C_{60} molecules on the surface of the topological insulator (TI) Bi_4Te_3. The TI samples were obtained from collaborators at the Forschungszentrum Jülich and their surface structure as well as their electronic properties studied using ARPES. These measurements revealed a clear surface state that is hexagonally warped and connects to the neighboring Brillouin zones through nodal lines at the Fermi level. These nodal lines

possess both surface and bulk character and the nodal lines open up into so-called flower petal states below the Fermi level. Slices through an ARPES map then revealed the existence of Dirac cone like features at the points of the nodal lines and flower petal states. This concise investigation of the topological insulator provided the basis for as a well defined surface for the growth of ordered, fullerene based structures.
One of these structures is a highly ordered C_{60} monolayer on top of the topological insulator that was prepared in UHV conditions. Through optimization of the growth procedure, a hexagonal C_{60} film was formed that perfectly aligned along the hexagonal surface of the underlying Bi_4Te_3, which was studied in depth using LEED. From these investigations we not only found the excellent directional alignment between the two structures but also a long range order in the form of a (4×4) on (9×9) superstructure. This pattern was identified through the existence of a moiré pattern in the LEED images, something that has not been shown yet in literature in the case of an organic molecule–inorganic topological insulator interface to the best of the authors knowledge. In literature, these moiré type superstructures were found to influence the electronic structure of other materials, as is best known in the case of superconductivity of magic angle bilayer graphene.[126, 127] Therefore the electronic properties of the newly formed moiré interface on Bi_4Te_3 were investigated through angle resolved photoemission spectroscopy. The band structure of the topological insulator showed no modulation through the overlayer in both bulk and surface state bands. This was found through high resolution scans at high symmetry points in combination with long range scans along the high symmetry directions of the Brillouin zone. These findings are in agreement with C_{60} films on

the related Bi_2Se_3 topological insulator, which did not show a moiré pattern however.

With the aid of density functional theory, the formation and properties of the interface were further investigated. Here we found that the interaction in the van der Waals film is stronger than that of the C_{60} molecule with the substrate, which is mostly physisorbed. The substrate–molecule interface calculations further showed, that binding of the C_{60} is preferred at Te sites, where each tellurium atom is pushed into the surface through the interaction of an adsorbed C_{60} molecule. This effect is enhanced by up to 50% in the (4×4) superstructure with respect to a single C_{60}. The fact that this distortion of the TI lattice is not followed by changes in the electronic structure is explained by the strong bismuth character of the bands measured near the Fermi level.

We further reason the softness of the surface to be one of the driving forces for the formation of a well defined organic film on the inorganic substrate. The balance between the interactions in the film and to the substrate is the reason for a slight strain in the C_{60} structure with respect to the bulk lattice, which results in the formation of the aforementioned superstructure. The fact, that the layer grows well and does not alter the electronic properties of the underlying TI mark this interface as an ideal protection of the topological insulator against further perturbation. On the other hand, the C_{60} molecules' properties could be tweaked through functionalization with heteroatoms or larger molecules to access a way to grow another highly ordered layer on top of this structure.

The interface of Bi_4Te_3 was also studied in the form of another fullerene based system, namely the alkali metal doped Rb_3C_{60}. Since Rb_3C_{60} is

metallic at room temperature and superconducting at a relatively high temperature of $T_c = 28\,\mathrm{K}$, this interface is highly interesting as the realization of an organic superconductor on an inorganic topological insulator. The growth of a pristine Rb_3C_{60} is non-trivial, since slight variations in the ratio between alkali metal and C_{60} result in the formation of overdoped Rb_6C_{60} and underdoped pristine C_{60} parts, both of which are insulating. The presence of these insulating domains hinders the formation of a well defined, long range superconductor. Therefore, much work was put into designing a method to efficiently control the growth of pristine Rb_3C_{60} on the surface of Bi_4Te_3 in this thesis. This method was developed with the aid of low energy electron diffraction in combination with photoemission spectroscopy (UPS). Where LEED found the existence of two different phases during the growth process, we were able to assign these phases to the metallic and insulating states using UPS. This allowed us to finally grow a very well ordered thin film of Rb_3C_{60} on the TI. The LEED images also show a $(\sqrt{3} \times \sqrt{3})$R30° superstructure. A recent report [115] found a similar superstructure through STM measurements in monolayers of K_3C_{60} only, which then vanished for the multilayer systems and was shown to be of insulating nature. STM measurements of monolayer Rb_3C_{60} did not feature this superstructure.[82]

The electronic properties of this new interface were briefly studied through mapping of the electronic band structure. Here we were still able to observe the characteristic, hexagonally warped Fermi surface of the underlying topological insulator in combination with a circular Fermi surface of the Rb_3C_{60}. Since there are no reports of the measurement of the two dimensional Fermi surface of Rb_3C_{60} available in litera-

ture, the measurements were compared to the closely related K_3C_{60} on a metallic substrate. Our data show a similar, general structure but at the moment are not of high enough quality to draw further conclusions. It is however interesting, that the bands of the Rb_3C_{60} intersect the Dirac-cone like features of the underlying topological insulator, which can be a point of interest for both theoretical and experimental physicists.

Chapter 8
Scientific contributions

8.1 List of Publications

- **Yannic Falke**, Niels Ehlen, Gianni Marini, Alex Grüneis *et al.* "Charge density wave enhanced coupling to zone center optical phonons in VSe_2" *Physical Review B* (2021) DOI: `https://doi.org/10.1103/PhysRevB.104.235137`.

- **Yannic Falke**, Boris Senkovskiy, Niels Ehlen, Alex Grüneis *et al.* "Photothermal Bottom-up Graphene Nanoribbon Growth Kinetics" *Nanoletters*, 20, 7, 4761-4767 (2020). DOI: `https://doi.org/10.1021/acs.nanolett.0c00317`.

- **Yannic Falke**, Niels Ehlen, Timo Knispel, Alex Grüneis *et al.* "Band structure control in Fe doped MoS_2" *in preparation.*

- **Yannic Falke**, Nicolae Atodiresei, Oliver Gallego, Alex Grüneis *et al.* "Realization of an Organic Superconductor – Topological Insulator Interface" *in preparation.*

- Dirk Honecker, Philipp Bender, **Yannic Falke**, Dominique Dresen, Sabrina Disch *et al.* "Controlling the Rotation Modes of Hematite Nanospindles by Dynamic Magnetic Fields" *submitted to Small (Wiley).*

- Tobias Hartl, Daniel Hermann, Moritz Will, **Yannic Falke**, Alex Grüneis, Pantelias Bampoulis "Silicon Cluster Arrays on the Monolayer of Hexagonal Boron Nitride on Ir(111)" *The Journal of Phys-*

ical Chemistry C (2022) DOI https://doi.org/10.1021/acs.jpcc.2c00694.

- Boris Senkovskiy, Alexey Nenashev, Seyed Alavi, **Yannic Falke**, Alex Grüneis *et al.* "Tunneling current modulation in atomically precise graphene nanoribbon heterojunctions" *Nature communications* 12, 2542 (2021). DOI: https://doi.org/10.1038/s41467-021-22774-0.

- Martin Hell, Niels Ehlen, Giovanni Marini, **Yannic Falke**, Alex Grüneis *et al.* "Massive and massless charge carriers in an epitaxially strained alkali metal quantum well on graphene" *Nature communications* 11, 1340 (2020). DOI: https://doi.org/10.1038/s41467-020-15130-1.

- Niels Ehlen, Martin Hell, Giovanni Marini, Eddwi Hesky Hasdeo, Riichiro Saito, **Yannic Falke**, Alex Grüneis *et al.* "Origin of the Flat Band in Heavily Cs-Doped Graphene" *ACS Nano* 14, 1, 1055-1069 (2020). DOI: https://doi.org/10.1021/acsnano.9b08622.

- Dominika Zakutna, **Yannic Falke**, Dominique Dresen, Sabrina Disch *et al.* "Morphological and crystallographic orientation of hematite spindles in an applied magnetic field" *Nanoscale* 11, 7149-7156 (2019). DOI: https://doi.org/10.1039/C8NR09583C.

- Martin G. Hell, **Yannic Falke**, Andrea Bliesener, Niels Ehlen, Alex Grüneis *et al.* "Combined Ultra High Vacuum Raman and Electronic Transport Characterization of Large-Area Graphene on

SiO_2" *physica status solidi b* (2018) DOI `https://doi.org/10.1002/pssb.201800456`.

8.2 Conferences

- MB Scientific AB workshop 2022, Uppsala, Sweden, 2022, **invited talk** on "Common use cases of angle resolved photoemission spectroscopy".

- Past and Future of Russian-German Uses of Synchrotron Radiation and Free Electron Lasers: International White Night Conference 2022, Saint-Petersburg, Russia, 2022, **invited talk** on "Band structure engineering in a molybdenum disulphide monolayer by iron doping", *Cancelled due to Russian-Ukrainian conflict.*

- Graphene Conference, Grenoble, France, 2021, **oral contribution** on "Photothermal Bottom-up Graphene Nanoribbon Growth Kinetics".

- CRC1238 Retreat, Bad Honnef, Germany, 2021, **invited talk** on "Electronic properties of Topological Insulator - Organic Superconductor interfaces".

- EWEG, St. Moritz, Switzerland, 2020, **oral contribution** on "Photothermal Bottom-up Graphene Nanoribbon Growth Kinetics", *Cancelled due to Covid-19 restrictions.*

- Inside Raman Meeting (Renishaw), Pliezhausen, Germany, 2019, **invited talk** on "Raman studies of Graphene Nanoribbons in UHV".

- E-MRS2019, Nice, France, 2019, **poster contribution** on "Raman studies of Graphene Nanoribbons in UHV".

Bibliography

(1) Pfeiffer, L.; West, K. W.; Stormer, H. L.; Baldwin, K. W. *Appl. Phys. Lett.* **1989**, *55*, 1888–1890, DOI: 10.1063/1.102162.

(2) Moore, G. E. et al. In *Electron devices meeting*, 1975; Vol. 21, pp 11–13.

(3) Introducing M1 Pro and M1 Max: the most powerful chips Apple has ever built, [Online; accessed 3. May 2022], 2022.

(4) Company, T. S. M. *Taiwan Semiconductor Manufactoring Company* **2021**.

(5) E. Katz, H. *J. Mater. Chem.* **1997**, *7*, 369–376, DOI: 10.1039/A605274F.

(6) Sun, Y.; Liu, Y.; Zhu, D. *J. Mater. Chem.* **2005**, *15*, 53–65, DOI: 10.1039/B411245H.

(7) Horowitz, G.; Fichou, D.; Peng, X.; Xu, Z.; Garnier, F. *Solid State Commun.* **1989**, *72*, 381–384, DOI: 10.1016/0038-1098(89)90121-X.

(8) Garnier, F. *Pure Appl. Chem.* **1996**, *68*, 1455–1462, DOI: 10.1351/pac199668071455.

(9) Sundar, V. C.; Zaumseil, J.; Podzorov, V.; Menard, E.; Willett, R. L.; Someya, T.; Gershenson, M. E.; Rogers, J. A. *Science* **2004**, *303*, 1644–1646, DOI: 10.1126/science.1094196.

(10) Dimitrakopoulos, C. D.; Malenfant, P. R. L. *Adv. Mater.* **2002**, *14*, 99–117, DOI: 10.1002/1521-4095(20020116)14:2<99::AID-ADMA99>3.0.CO;2-9.

(11) Kelley, T. W.; Muyres, D. V.; Baude, P. F.; Smith, T. P.; Jones, T. D. *MRS Online Proceedings Library (OPL)* **2003**, *771*, DOI: 10.1557/PROC-771-L6.5.

(12) Kagan, C.; Andry, P., *Thin-Film Transistors*, 2003.

(13) Reese, C.; Roberts, M.; Ling, M.-m.; Bao, Z. *Mater. Today* **2004**, *7*, 20–27, DOI: 10.1016/S1369-7021(04)00398-0.

(14) Kline, R. J.; McGehee, M. D.; Kadnikova, E. N.; Liu, J.; Fréchet, J. M. J. *Adv. Mater.* **2003**, *15*, 1519–1522, DOI: 10.1002/adma.200305275.

(15) Xu, W.; Lee, T.-W. *Mater. Horiz.* **2016**, *3*, 186–207, DOI: 10.1039/C5MH00288E.

(16) Tour, J. M. *Chem. Mater.* **2014**, *26*, 163–171, DOI: 10.1021/cm402179h.

(17) Senkovskiy, B. V. et al. *Nat. Commun.* **2021**, *12*, 1–11, DOI: 10.1038/s41467-021-22774-0.

(18) Alavi, S. K.; Senkovskiy, B. V.; Hertel, D.; Haberer, D.; Ando, Y.; Meerholz, K.; Fischer, F. R.; Grüneis, A.; Lindfors, K. *ACS Appl. Nano Mater.* **2020**, *3*, 8343–8351, DOI: 10.1021/acsanm.0c01549.

(19) Chen, Z.; Narita, A.; Müllen, K. *Adv. Mater.* **2020**, *32*, 2001893, DOI: 10.1002/adma.202001893.

(20) Cai, J.; Ruffieux, P.; Jaafar, R.; Bieri, M.; Braun, T.; Blankenburg, S.; Muoth, M.; Seitsonen, A. P.; Saleh, M.; Feng, X.; Müllen, K.; Fasel, R. *Nature* **2010**, *466*, 470–473, DOI: 10.1038/nature09211.

(21) Jona, F.; Strozier Jr., J. A.; Yang, W. S. *Rep. Prog. Phys.* **1982**, *45*, 527–585, DOI: 10.1088/0034-4885/45/5/002.

(22) Ponor and Contributors to Wikimedia projects Low-energy electron diffraction - Wikipedia, [Online; accessed 18. May 2022], 2021.

(23) Glasser, O., *Wilhelm Conrad Röntgen and the early history of the Roentgen rays*; 1; Norman Publishing: 1993.

(24) Sharma, R.; Bisen, D. P.; Shukla, U.; Sharma, B. *Recent Research in Science and Technology* **2012**, *4*, 77–79.

(25) Hammond, C. In *The Basics of Crystallography and Diffraction*; Oxford University Press: Oxford, England, UK, DOI: 10.1093/acprof:oso/9780198738671.001.0001.

(26) Van Hove, M. A.; Tong, S. Y., *Surface crystallography by LEED: theory, computation and structural results*; Springer Science & Business Media: 2012; Vol. 2.

(27) Van Hove, M. A.; Moritz, W.; Over, H.; Rous, P. J.; Wander, A.; Barbieri, A.; Materer, N.; Starke, U.; Somorjai, G. A. *Surf. Sci. Rep.* **1993**, *19*, 191–229, DOI: 10.1016/0167-5729(93)90011-D.

(28) Shin, H.-C.; Ahn, S. J.; Kim, H. W.; Moon, Y.; Rai, K. B.; Woo, S. H.; Ahn, J. R. *Appl. Phys. Lett.* **2016**, *109*, 081603, DOI: 10.1063/1.4961633.

(29) Pan, Y.; Zhang, L.; Huang, L.; Li, L.; Meng, L.; Gao, M.; Huan, Q.; Lin, X.; Wang, Y.; Du, S.; Freund, H.-J.; Gao, H.-J. *Small* **2014**, *10*, 2215–2225, DOI: 10.1002/smll.201303698.

(30) N'Diaye, A. T.; Coraux, J.; Plasa, T. N.; Busse, C.; Michely, T. *New J. Phys.* **2008**, *10*, 043033, DOI: 10.1088/1367-2630/10/4/043033.

(31) Hertz, H. *Ann. Phys.* **1887**, *267*, 983–1000, DOI: 10.1002/andp.18872670827.

(32) The Nobel Prize in Physics 1921, [Online; accessed 3. May 2022], 2022.

(33) Damascelli, A.; Hussain, Z.; Shen, Z.-X. *Rev. Mod. Phys.* **2003**, *75*, 473–541, DOI: 10.1103/RevModPhys.75.473.

(34) Seah, M. P. *Surf. Interface Anal.* **2012**, *44*, 497–503, DOI: 10.1002/sia.4816.

(35) Miller, T.; McMahon, W. E.; Chiang, T.-C. *Phys. Rev. Lett.* **1996**, *77*, 1167–1170, DOI: 10.1103/PhysRevLett.77.1167.

(36) Adams, F. C. In *Encyclopedia of Analytical Science (Third Edition)*; Academic Press: Cambridge, MA, USA, 2019, pp 391–403, DOI: 10.1016/B978-0-12-409547-2.14263-5.

(37) Ishikawa, T.; Tamasaku, K.; Yabashi, M. *Nucl. Instrum. Methods Phys. Res., Sect. A* **2005**, *547*, 42–49, DOI: 10.1016/j.nima.2005.05.010.

(38) HIS Mono - VUV Monochromator - FOCUS GmbH, [Online; accessed 4. May 2022], 2022.

(39) Ponor Setup of an ARPES experiment, [Online; accessed 3. May 2022], 2020.

(40) The Nobel Prize in Physics 1930, [Online; accessed 4. May 2022], 2022.

(41) Dresselhaus, M.; Dresselhaus, G.; Cronin, S.; Filho, A. G. S., *Solid State Properties*; Springer: Berlin, Germany.

(42) Atkins, P. W.; de Paula, J.; J., K. J., *Physikalische Chemie*, 6th ed.; Wiley-VCH.

(43) Cardona, M., *Light Scattering in Solids 1*; Springer: Berlin, Germany, 1975.

(44) Ferrari, A. C.; Basko, D. M. *Nat. Nanotechnol.* **2013**, *8*, 235–246, DOI: 10.1038/nnano.2013.46.

(45) Childres, I.; Jauregui, L.; Park, W.; Caoa, H.; Chena, Y. *New Developments in Photon and Materials Research* **2013**, 403–418.

(46) Ferrari, A. C.; Meyer, J. C.; Scardaci, V.; Casiraghi, C.; Lazzeri, M.; Mauri, F.; Piscanec, S.; Jiang, D.; Novoselov, K. S.; Roth, S.; Geim, A. K. *Phys. Rev. Lett.* **2006**, *97*, 187401, DOI: 10.1103/PhysRevLett.97.187401.

(47) Basko, D. M.; Piscanec, S.; Ferrari, A. C. *Phys. Rev. B* **2009**, *80*, 165413, DOI: 10.1103/PhysRevB.80.165413.

(48) Ferrari, A. C.; Robertson, J. *Phys. Rev. B* **2001**, *64*, 075414, DOI: 10.1103/PhysRevB.64.075414.

(49) Kürti, J.; Zólyomi, V.; Grüneis, A.; Kuzmany, H. *Phys. Rev. B* **2002**, *65*, 165433, DOI: 10.1103/PhysRevB.65.165433.

(50) Tuschel, D. *Spectroscopy* **2018**, *33*, 12–19.

(51) Novoselov, K. S.; Geim, A. K.; Morozov, S. V.; Jiang, D.; Zhang, Y.; Dubonos, S. V.; Grigorieva, I. V.; Firsov, A. A. *Science* **2004**, *306*, 666–669, DOI: 10.1126/science.1102896.

(52) Dresselhaus, M. S.; Dresselhaus, G.; Eklund, P. C.; Rao, A. M. In *The Physics of Fullerene-Based and Fullerene-Related Materials*; Springer: Dordrecht, The Netherlands, 2000, pp 331–379, DOI: 10.1007/978-94-011-4038-6_9.

(53) Ruffieux, P.; Wang, S.; Yang, B.; Sánchez-Sánchez, C.; Liu, J.; Dienel, T.; Talirz, L.; Shinde, P.; Pignedoli, C. A.; Passerone, D.; Dumslaff, T.; Feng, X.; Müllen, K.; Fasel, R. *Nature* **2016**, *531*, 489–492, DOI: 10.1038/nature17151.

(54) Kane, C. L.; Mele, E. J. *Phys. Rev. Lett.* **2005**, *95*, 146802, DOI: 10.1103/PhysRevLett.95.146802.

(55) Backes, C.; Abdelkader, A. M.; Alonso, C.; Andrieux-Ledier, A.; Arenal, R.; Azpeitia, J.; Balakrishnan, N.; Banszerus, L.; Barjon, J.; Bartali, R.; Bellani, S.; Berger, C.; Berger, R.; Ortega; Garcia-Hernandez, M. *2D Mater.* **2020**, *7*, 022001, DOI: 10.1088/2053-1583/ab1e0a.

(56) Kosynkin, D. V.; Higginbotham, A. L.; Sinitskii, A.; Lomeda, J. R.; Dimiev, A.; Price, B. K.; Tour, J. M. *Nature* **2009**, *458*, 872–876, DOI: 10.1038/nature07872.

(57) Sprinkle, M.; Ruan, M.; Hu, Y.; Hankinson, J.; Rubio-Roy, M.; Zhang, B.; Wu, X.; Berger, C.; de Heer, W. A. *Nat. Nanotechnol.* **2010**, *5*, 727–731, DOI: 10.1038/nnano.2010.192.

(58) Chen, Z. et al. *J. Am. Chem. Soc.* **2016**, *138*, 15488–15496, DOI: 10.1021/jacs.6b10374.

(59) Corso, M.; Carbonell-Sanromà, E.; de Oteyza, D. G. In *On-Surface Synthesis II*; Springer: Cham, Switzerland, 2018, pp 113–152, DOI: 10.1007/978-3-319-75810-7_6.

(60) Dong, L.; Liu, P. N.; Lin, N. *Acc. Chem. Res.* **2015**, *48*, 2765–2774, DOI: 10.1021/acs.accounts.5b00160.

(61) 10,10′-dibromo-9,9′-bianthracene | 121848-75-7, [Online; accessed 9. May 2022], 2022.

(62) Kroto, H. W.; Heath, J. R.; O'Brien, S. C.; Curl, R. F.; Smalley, R. E. *Nature* **1985**, *318*, 162–163, DOI: 10.1038/318162a0.

(63) Komatsu, K.; Murata, M.; Murata, Y. *Science* **2005**, *307*, 238–240, DOI: 10.1126/science.1106185.

(64) Shahamirian, M.; Azami, S. M. *Phys. Lett. A* **2019**, *383*, 126004, DOI: 10.1016/j.physleta.2019.126004.

(65) Chistyakov, V. A.; Smirnova, Y. O.; Prazdnova, E. V.; Soldatov, A. V. *Biomed Res. Int.* **2013**, *2013*, DOI: 10.1155/2013/821498.

(66) Gharbi, N.; Pressac, M.; Hadchouel, M.; Szwarc, H.; Wilson, S. R.; Moussa, F. *Nano Lett.* **2005**, *5*, 2578–2585, DOI: 10.1021/nl051866b.

(67) Ubasart, E.; Borodin, O.; Fuertes-Espinosa, C.; Xu, Y.; Garcia-Simón, C.; Gómez, L.; Juanhuix, J.; Gándara, F.; Imaz, I.; Maspoch, D.; von Delius, M.; Ribas, X. *Nat. Chem.* **2021**, *13*, 420–427, DOI: 10.1038/s41557-021-00658-6.

(68) Yan, W.; Seifermann, S. M.; Pierrat, P.; Bräse, S. *Org. Biomol. Chem.* **2014**, *13*, 25–54, DOI: 10.1039/C4OB01663G.

(69) Lof, R. W.; van Veenendaal, M. A.; Koopmans, B.; Jonkman, H. T.; Sawatzky, G. A. *Phys. Rev. Lett.* **1992**, *68*, 3924–3927, DOI: 10.1103/PhysRevLett.68.3924.

(70) Illescas, B. M.; Martin, N. *C. R. Chim.* **2006**, *9*, 1038–1050, DOI: 10.1016/j.crci.2005.11.016.

(71) Kumar, A.; Podhorodecki, A.; Misiewicz, J.; Avasthi, D. K.; Pivin, J. C. *J. Appl. Phys.* **2009**, *105*, 024314, DOI: 10.1063/1.3074104.

(72) Krätschmer, W. In *Electronic Properties of High-T Superconductors*; Springer: Berlin, Germany, 1993, pp 459–465, DOI: 10.1007/978-3-642-84865-0_80.

(73) Li, G.; Zhou, H. T.; Pan, L. D.; Zhang, Y.; Mao, J. H.; Zou, Q.; Guo, H. M.; Wang, Y. L.; Du, S. X.; Gao, H.-J. *Appl. Phys. Lett.* **2012**, *100*, 013304, DOI: 10.1063/1.3673830.

(74) Reddy, C. D.; Gen Yu, Z.; Zhang, Y.-W. *Sci. Rep.* **2015**, *5*, 1–7, DOI: 10.1038/srep12221.

(75) Schull, G.; Berndt, R. *Phys. Rev. Lett.* **2007**, *99*, 226105, DOI: 10.1103/PhysRevLett.99.226105.

(76) Shang, Y.; Wang, Z.; Yang, D.; Wang, Y.; Ma, C.; Tao, M.; Sun, K.; Yang, J.; Wang, J. *Nanomaterials* **2020**, *10*, 1305, DOI: 10.3390/nano10071305.

(77) Guo, H.; Martinez-Galera, A. J.; Gomez-Rodriguez, J. M. *Nanotechnology* **2020**, *32*, 025711, DOI: 10.1088/1361-6528/abbbb2.

(78) Ramirez, A. P. *Phys. C* **2015**, *514*, 166–172, DOI: 10.1016/j.physc.2015.02.014.

(79) Ganin, A. Y.; Takabayashi, Y.; Khimyak, Y. Z.; Margadonna, S.; Tamai, A.; Rosseinsky, M. J.; Prassides, K. *Nat. Mater.* **2008**, *7*, 367–371, DOI: 10.1038/nmat2179.

(80) Potočnik, A.; Krajnc, A.; Jeglič, P.; Takabayashi, Y.; Ganin, A. Y.; Prassides, K.; Rosseinsky, M. J.; Arčon, D. *Sci. Rep.* **2014**, *4*, 1–5, DOI: 10.1038/srep04265.

(81) Rogge, S.; Durkut, M.; Klapwijk, T. M. *Phys. Rev. B* **2003**, *67*, 033410, DOI: 10.1103/PhysRevB.67.033410.

(82) Wang, S.-Z.; Ren, M.-Q.; Han, S.; Cheng, F.-J.; Ma, X.-C.; Xue, Q.-K.; Song, C.-L. *Commun. Phys.* **2021**, *4*, 1–8, DOI: 10.1038/s42005-021-00619-y.

(83) Falke, Y.; Ehlen, N.; Marini, G.; Fedorov, A. V.; Voroshnin, V. Y.; Senkovskiy, B. V.; Nikonov, K.; Hoesch, M.; Kim, T. K.; Petaccia, L.; Di Santo, G.; Szkopek, T.; Profeta, G.; Grüneis, A. *Phys. Rev. B* **2021**, *104*, 235137, DOI: 10.1103/PhysRevB.104.235137.

(84) Li, Y.; Lou, N.; Gan, L. *Org. Lett.* **2015**, *17*, 524–527, DOI: 10.1021/ol503536z.

(85) Carrillo-Bohórquez, O.; Valdés, Á.; Prosmiti, R. *J. Chem. Theory Comput.* **2021**, *17*, 5839–5848, DOI: 10.1021/acs.jctc.1c00662.

(86) Whitener, K. E.; Frunzi, M.; Iwamatsu, S.-i.; Murata, S.; Cross, R. J.; Saunders, M. *J. Am. Chem. Soc.* **2008**, *130*, 13996–13999, DOI: 10.1021/ja805579m.

(87) Gruznev, D. V.; Matetskiy, A. V.; Bondarenko, L. V.; Utas, O. A.; Zotov, A. V.; Saranin, A. A.; Chou, J. P.; Wei, C. M.; Lai, M. Y.; Wang, Y. L. *Nat. Commun.* **2013**, *4*, 1–7, DOI: 10.1038/ncomms2706.

(88) Muntwiler, M.; Auwärter, W.; Seitsonen, A. P.; Osterwalder, J.; Greber, T. *Phys. Rev. B* **2005**, *71*, 121402, DOI: 10.1103/PhysRevB.71.121402.

(89) Barth, J. V. *Annu. Rev. Phys. Chem.* **2007**, *58*, 375–407, DOI: 10.1146/annurev.physchem.56.092503.141259.

(90) Wang, Y.-R.; Tao, M.-L.; Chao-Ke, M.; Wang, Z.-L.; Yang, D.-X.; Shi, M.-X.; Sun, K.; Yang, J.-Y.; Wang, J.-Z. *RSC Adv.* **2021**, *11*, 14148–14153, DOI: 10.1039/D1RA00900A.

(91) Sadowski, J. T.; Bakhtizin, R. Z.; Oreshkin, A. I.; Nishihara, T.; Al-Mahboob, A.; Fujikawa, Y.; Nakajima, K.; Sakurai, T. *Surf. Sci.* **2007**, *601*, L136–L139, DOI: 10.1016/j.susc.2007.10.005.

(92) Mihalyuk, A. N.; Utas, T. V.; Eremeev, S. V.; Hsing, C. R.; Wei, C. M.; Zotov, A. V.; Saranin, A. A. *J. Chem. Phys.* **2021**, *154*, 104703, DOI: 10.1063/5.0040483.

(93) Li, H. I.; Franke, K. J.; Pascual, J. I.; Bruch, L. W.; Diehl, R. D. *Phys. Rev. B* **2009**, *80*, 085415, DOI: 10.1103/PhysRevB.80.085415.

(94) Latzke, D. W.; Ojeda-Aristizabal, C.; Griffin, S. M.; Denlinger, J. D.; Neaton, J. B.; Zettl, A.; Lanzara, A. *Phys. Rev. B* **2019**, *99*, 045425, DOI: 10.1103/PhysRevB.99.045425.

(95) Sessi, P.; Bathon, T.; Kokh, K. A.; Tereshchenko, O. E.; Bode, M. *Nano Lett.* **2014**, *14*, 5092–5096, DOI: 10.1021/nl5017893.

(96) Bathon, T.; Sessi, P.; Kokh, K. A.; Tereshchenko, O. E.; Bode, M. *Nano Lett.* **2015**, *15*, 2442–2447, DOI: 10.1021/nl5048434.

(97) Yang, H.-H.; Chu, Y.-H.; Lu, C.-I.; Butler, C. J.; Sankar, R.; Chou, F.-C.; Lin, M.-T. *Nano Lett.* **2015**, *15*, 6896–6900, DOI: 10.1021/acs.nanolett.5b02811.

(98) Yamana, K.; Kihara, K.; Matsumoto, T. *Acta Crystallogr. B* **1979**, *35*, 147–149, DOI: 10.1107/S0567740879002788.

(99) Chagas, T.; Ribeiro, G. A. S.; Gonçalves, P. H. R.; Calil, L.; Silva, W. S.; Malachias, Â.; Mazzoni, M. S. C.; Magalhães-Paniago, R. *Electron. Struct.* **2020**, *2*, 015002, DOI: 10.1088/2516-1075/ab7398.

(100) Chagas, T.; Ashour, O. A.; Ribeiro, G. A. S.; Silva, W. S.; Li, Z.; Louie, S. G.; Magalhães-Paniago, R.; Petroff, Y. *Phys. Rev. B* **2022**, *105*, L081409, DOI: 10.1103/PhysRevB.105.L081409.

(101) Nabok, D.; Tas, M.; Kusaka, S.; Durgun, E.; Friedrich, C.; Bihlmayer, G.; Blügel, S.; Hirahara, T.; Aguilera, I. *Phys. Rev. Mater.* **2022**, *6*, 034204, DOI: 10.1103/PhysRevMaterials.6.034204.

(102) Stanescu, T. D.; Sau, J. D.; Lutchyn, R. M.; Sarma, S. D. *arXiv* **2010**, DOI: 10.1103/PhysRevB.81.241310.

(103) Hsieh, D.; Qian, D.; Wray, L.; Xia, Y.; Hor, Y. S.; Cava, R. J.; Hasan, M. Z. *Nature* **2008**, *452*, 970–974, DOI: 10.1038/nature06843.

(104) Roushan, P.; Seo, J.; Parker, C. V.; Hor, Y. S.; Hsieh, D.; Qian, D.; Richardella, A.; Hasan, M. Z.; Cava, R. J.; Yazdani, A. *Nature* **2009**, *460*, 1106–1109, DOI: 10.1038/nature08308.

(105) Zhang, T.; Cheng, P.; Chen, X.; Jia, J.-F.; Ma, X.; He, K.; Wang, L.; Zhang, H.; Dai, X.; Fang, Z.; Xie, X.; Xue, Q.-K. *Phys. Rev. Lett.* **2009**, *103*, 266803, DOI: 10.1103/PhysRevLett.103.266803.

(106) Hsieh, D.; Xia, Y.; Wray, L.; Qian, D.; Pal, A.; Dil, J. H.; Osterwalder, J.; Meier, F.; Bihlmayer, G.; Kane, C. L.; Hor, Y. S.; Cava, R. J.; Hasan, M. Z. *Science* **2009**, *323*, 919–922, DOI: 10.1126/science.1167733.

(107) Fu, L.; Kane, C. L. *Phys. Rev. Lett.* **2008**, *100*, 096407, DOI: 10.1103/PhysRevLett.100.096407.

(108) Xu, H.; Song, Y.; Pan, W.; Chen, Q.; Wu, X.; Lu, P.; Gong, Q.; Wang, S. *AIP Adv.* **2015**, *5*, 087103, DOI: 10.1063/1.4928217.

(109) Fu, L. *Phys. Rev. Lett.* **2009**, *103*, 266801, DOI: 10.1103/PhysRevLett.103.266801.

(110) Azizi, J.; Phirouznia, A.; Hasanirokh, K. *Physica E* **2015**, *68*, 28–32, DOI: 10.1016/j.physe.2014.12.010.

(111) Wang, Z.; Yin, Q.; Yan, S.; Wu, L.; Wu, X.; Li, M.; Song, W.; Liu, Q.; Ma, H.; Ji, W.; Lei, H.; Wang, S. *Phys. Rev. B* **2021**, *104*, 155134, DOI: 10.1103/PhysRevB.104.155134.

(112) Fu, B.-B. et al. *Sci. Adv.* **2019**, *5*, eaau6459, DOI: 10.1126/sciadv.aau6459.

(113) Cheng, Z.; Zhang, Z.; Sun, H.; Li, S.; Yuan, H.; Wang, Z.; Cao, Y.; Shao, Z.; Bian, Q.; Zhang, X.; Li, F.; Feng, J.; Ding, S.; Mao, Z.; Pan, M. *APL Mater.* **2019**, *7*, 051105, DOI: 10.1063/1.5084090.

(114) Chen, C. T.; Tjeng, L. H.; Rudolf, P.; Meigs, G.; Rowe, J. E.; Chen, J.; McCauley, J. P.; Smith, A. B.; McGhie, A. R.; Romanow, W. J.; Plummer, E. W. *Nature* **1991**, *352*, 603–605, DOI: 10.1038/352603a0.

(115) Ren, M.-Q.; Han, S.; Wang, S.-Z.; Fan, J.-Q.; Song, C.-L.; Ma, X.-C.; Xue, Q.-K. *Phys. Rev. Lett.* **2020**, *124*, 187001, DOI: 10.1103/PhysRevLett.124.187001.

(116) Brouet, V.; Yang, W. L.; Zhou, X. J.; Hussain, Z.; Shen, Z. X. *J. Phys. Chem. Solids* **2006**, *67*, 218–222, DOI: 10.1016/j.jpcs.2005.10.170.

(117) Alferov, Z. I. *Rev. Mod. Phys.* **2001**, *73*, 767–782, DOI: 10.1103/RevModPhys.73.767.

(118) Dai, X.; Zhang, S.; Wang, Z.; Adamo, G.; Liu, H.; Huang, Y.; Couteau, C.; Soci, C. *Nano Lett.* **2014**, *14*, 2688–2693, DOI: 10.1021/nl5006004.

(119) Geim, A. K.; Grigorieva, I. V. *Nature* **2013**, *499*, 419–425, DOI: 10.1038/nature12385.

(120) Vadlamani, S. K.; Agarwal, S.; Limmer, D. T.; Louie, S. G.; Fischer, F. R.; Yablonovitch, E. *Proc. IEEE* **2019**, *108*, 1235–1244, DOI: 10.1109/JPROC.2019.2904011.

(121) Ionescu, A. M.; Riel, H. *Nature* **2011**, *479*, 329–337, DOI: 10.1038/nature10679.

(122) Zhang, Q.; Fang, T.; Xing, H.; Seabaugh, A.; Jena, D. *IEEE Electron Device Lett.* **2008**, *29*, 1344–1346, DOI: 10.1109/LED.2008.2005650.

(123) Richard-Lacroix, M.; Zhang, Y.; Dong, Z.; Deckert, V. *Chem. Soc. Rev.* **2017**, *46*, 3922–3944, DOI: 10.1039/C7CS00203C.

(124) Jakobs, S. et al. *Nano Lett.* **2015**, *15*, 6022–6029, DOI: 10.1021/acs.nanolett.5b02213.

(125) Grüneis, A.; Senkovskiy, B. V.; Fedorov, A. V.; Hell, M.; Michel, S. In *Encyclopedia of Interfacial Chemistry*; Elsevier: Walthm, MA, USA, 2018, pp 367–374, DOI: 10.1016/B978-0-12-409547-2.14168-X.

(126) Li, G.; Luican, A.; Lopes dos Santos, J. M. B.; Castro Neto, A. H.; Reina, A.; Kong, J.; Andrei, E. Y. *Nat. Phys.* **2010**, *6*, 109–113, DOI: 10.1038/nphys1463.

(127) Dean, C. R.; Wang, L.; Maher, P.; Forsythe, C.; Ghahari, F.; Gao, Y.; Katoch, J.; Ishigami, M.; Moon, P.; Koshino, M.; Taniguchi, T.; Watanabe, K.; Shepard, K. L.; Hone, J.; Kim, P. *Nature* **2013**, *497*, 598–602, DOI: 10.1038/nature12186.

(128) Van Rossum, G.; Drake, F. L., *Python 3 Reference Manual*; CreateSpace: Scotts Valley, CA, 2009.

(129) WaveMetrics IGOR Pro, 2016.

(130) Hunter, J. D. *Computing in Science & Engineering* **2007**, *9*, 90–95, DOI: 10.1109/MCSE.2007.55.

(131) Inkscape Project Inkscape, version 0.92.5, 2020.

Appendix

Acknowledgements

I would like to thank Prof. Alexander Grüneis for supervising my PhD thesis in the recent years and the ability explore the interesting field of experimental physics. Our direct and open communication was extremely helpful and proved to be quite efficient. I would further like to thank Prof. Klas Lindfors for taking the role of my second supervisor and his very constructive feedback. His calm and on-point mentality made our few discussions very pleasant. I also thank Prof. Mathias Wickleder and Dr. Dirk Hertel very much for taking the role of the committee chair and notes taker respectively.
Words can not describe how much I value the support of my girlfriend Friederike and the joy she brings to my life. Thank you for being there for me when I needed you and despite me not being home a lot.
I owe a lot to my family for always supporting me and understanding that studying natural sciences can be somewhat stressful at times. I always feel at home with you and enjoy our limited time thoroughly.
Of course I could not have succeeded with this thesis without the great support of my colleagues. I especially want to thank Niels Ehlen, Martin Hell, Boris Senkovskiy, Alexander Chernov, Alessandro D'Elia, Max Buchta and Oliver Gallego with whom I enjoyed working and "processing just having worked" a lot. Our scientific and non-scientific discussions always made for good times. I further thank all the other people that were part of our workgroup for great collaborations.
The SFB has to receive further thanks for the fruitful discussions, where I would like to especially point out those with Robin Bernhardt, Andrea

Bliesener and Raphael German.
All the people that aided me on beamtimes have my deepest regards and I want to thank them for their great and thorough support. This includes, but is not limited to, Luca Petaccia, Giovanni Di Santo and José Avila.
Of course I also like to thank all the countless collaborators of my published and ongoing work. Discussions with you were always great and lead to many scientific results.
Working and going on beamtimes with Prof. Thomas Michely and his group were always pleasant and helped me gain a different point of view on many related topics. Here I would really like to thank the postdocs Jeison Fischer and Wouter Jolie for always being in a good mood when I came with lots of questions as well the PhD students in the group for taking their time and sharing thoughts.
All the people in the chemistry department with whom I am still in close contact have to receive many thanks for providing a lot of variety on topics of scientific and non-scientific discussion. It was great to talk about the love-hatred relationship with chemistry that we all so deeply share.
Of course I have to thank all of my friends and previous colleagues who left chemistry already. Working with you was great and enjoying life with you still is always great. I really value it a lot that we are still in good contact or have even become good friends. All of you have really pushed me to continuing and finishing my PhD work.
Finally, I immensely thank all of my friends not related to science with whom I can always enjoy good times and take the very much needed brakes from thinking about work.

List of Figures

Data Availability

All collected data are backed up on redundant RAID1 drives on the work-group internal PC and can be made available upon reasonable request. The data is additionally backed up on the back-up server "TSM" of the University of Cologne. The exact samples that were used during data acquisition are mainly stable in UHV only and can therefore not be supplied. Procedures on their synthesis are found in the respective sections.

Used Tools

Data analysis was performed through python3[128] and Igor Pro 6.0[129]. Python scripts are backed up and can be accessed as described in Section 8.2. Individual figures were produced using pythons matplotlib library[130] and Igor Pro 6.0 and combinations were constructed using Inkscape[131]. This thesis was written using LaTeX.

Declaration of Authorship

(Gemäß der Promotionsordnung vom 12. März 2020)
Hiermit versichere ich an Eides statt, dass ich die vorliegende Dissertation selbstständig und ohne die Benutzung anderer als der angegebenen Hilfsmittel und Literatur angefertigt habe. Alle Stellen, die wörtlich oder sinngemäß aus veröffentlichten und nicht veröffentlichten Werken dem Wortlaut oder dem Sinn nach entnommen wurden, sind als solche kenntlich gemacht. Ich versichere an Eides statt, dass diese Dissertation noch keiner anderen Fakultät oder Universität zur Prüfung vorgelegen hat; dass sie - abgesehen von unten angegebenen Teilpublikationen und eingebundenen Artikeln und Manuskripten - noch nicht veröffentlicht worden ist sowie, dass ich eine Veröffentlichung der Dissertation vor Abschluss der Promotion nicht ohne Genehmigung des Promotionsausschusses vornehmen werde. Die Bestimmungen dieser Ordnung sind mir bekannt. Darüber hinaus erkläre ich hiermit, dass ich die Ordnung zur Sicherung guter wissenschaftlicher Praxis und zum Umgang mit wissenschaftlichem Fehlverhalten der Universität zu Köln gelesen und sie bei der Durchführung der Dissertation zugrundeliegenden Arbeiten und der schriftlich verfassten Dissertation beachtet habe und verpflichte mich hiermit, die dort genannten Vorgaben bei allen wissenschaftlichen Tätigkeiten zu beachten und umzusetzen. Ich versichere, dass die eingereichte elektronische Fassung der eingereichten Druckfassung vollständig entspricht.

Teilpublikationen

- **Yannic Falke**, Boris Senkovskiy, Niels Ehlen, Alex Grüneis *et al.* "Photothermal Bottom-up Graphene Nanoribbon Growth Kinetics" *Nanoletters*, 20, 7, 4761-4767 (2020). Reprinted with permission © 2021 ACS.
  DOI: `https://doi.org/10.1021/acs.nanolett.0c00317`.

Yannic Frank Falke 05.06.2022